Sardar, Sabah (2024) *Cellular phenotype characterisation in different variants of visceral myopathy.* PhD thesis.

https://theses.gla.ac.uk/84706/

Cellular Phenotype Characterisation in Different Variants of Visceral Myopathy

Sabah Sardar
BSc (Hons), MRes

Submitted in fulfilment of the requirements for the
Degree of Doctor of Philosophy

School of Engineering
College of Science and Engineering
University of Glasgow
July 2024

Abstract

Visceral myopathy is a rare and severe gastrointestinal motility disorder, affecting 1 in 100,000 individuals globally. It is a genetically heterogeneous disease where the genetics behind the disorder are not fully understood. Visceral myopathy results in a pseudo-obstruction in the intestine without the presence of a mechanical obstruction. This has been attributed to an impairment in the contractile phenotype of smooth muscle cells. Several genes, and variants within those genes, have been associated with visceral myopathy, all of which cause similar symptoms to develop in individuals with the disease. Currently, variants in the enteric smooth muscle actin gamma 2 (*ACTG2*) gene have been identified as causing approximately 40-50% of cases. However, the rarity of visceral myopathy coupled with misdiagnosis or late diagnosis, has resulted in limited advances in available treatment options.

Whilst the disease impacts on a mechanical phenotype, its mechanobiology has not been fully investigated yet. Therefore, studying the disorder from a mechanobiological and biochemical perspective is beneficial for gaining insights into the disease pathology in order to aid in developing therapies and improving disease diagnosis. With this in mind, patient dermal fibroblasts were used as a model for investigating the morpho-mechanical and biochemical characteristics of visceral myopathy cells. The variants investigated were *ACTG2* variants R257C and R38H, as well as novel *PIEZO1* biallelic mutations affecting S1814F and P2230L. Initially, Yes-associated protein (YAP) translocation and traction forces exerted by cells were analysed. This was followed by the study of cell morphology, the mechanical clutch model, and migration. The metabolic profiles were then assessed and comparisons were drawn between visceral myopathy caused by *ACTG2* and *PIEZO1* mutations. *PIEZO1* associated VSCM was found to differ completely from *ACTG2*-VSCM, at a morpho-mechanical and metabolomic level.

Furthermore, in this work, YAP nuclear localisation, traction forces, and cell migration were identified as potential disease markers which can be exploited for the development of diagnostic and drug screening assays. However, it was traction forces which emerged as the most promising label-free physical biomarker for visceral myopathy. Particularly, when traction forces are measured using the micropillar array platform as it provides a robust method which has the potential

to be used for therapeutic purposes.

Declaration

University of Glasgow
College of Science and Engineering

Statement of Originality to Accompany Thesis Submission

Name: Sabah Sardar

Registration Number:

I certify that the thesis presented here for examination for PhD degree of the University of Glasgow is solely my own work other than where I have clearly indicated that it is the work of others (in which case the extent of any work carried out jointly by me and any other person is clearly identified in it) and that the thesis has not been edited by a third party beyond what is permitted by the University's PGR Code of Practice.

The copyright of this thesis rests with the author. No quotation from it is permitted without full acknowledgement.

I declare that the thesis does not include work forming part of a thesis presented successfully for another degree [unless explicitly identified and as noted below].

I declare that this thesis has been produced in accordance with the University of Glasgow's Code of Good Practice in Research.

I acknowledge that if any issues are raised regarding good research practice based on review of the thesis, the examination may be postponed pending the outcome of any investigation of the issues.

Signature:

Acknowledgements

I would like to thank my supervisors, Professor Massimo Vassalli, Professor Matthew Dalby, and Professor Manuel Salmeron-Sanchez, for their constant support and guidance over the years. I am especially grateful to Massimo for the continuous encouragement, discussions, and opportunities he has provided me during this PhD.

Additionally, I would also like to thank Matthew for providing me with the opportunity to undertake this PhD as part of the lifETIME centre for doctoral training (CDT). It has been a great experience from which I have learned valuable skills and met some wonderful people.

I am also grateful to Dr Monica Tsimbouri for the knowledge and support she has provided me over the years. I could not have done this without her and will forever be grateful for the invaluable advice she has provided me throughout my PhD.

I am thankful to Dr Federica Viti and Dr Isabella Ceccherini, who have taught me everything I know about visceral myopathy. Thank you for the zoom call meetings during lockdown, your constant feedback, and the overall patience and kindness you have shown me over these four years.

I would also like to thank the Alessandra Bono Foundation in Italy, the Baldussi-Contessa Family and the IRCCS Giannina Gaslini Children's Hospital (Genoa, Italy) for the financial support and knowledge exchange during my PhD. Additionally, I am extremely grateful to Professor Elena Bonora and the Sant'Orsola - Malpighi Polyclinic for providing me with samples of the *PIEZO1* mutations causing visceral myopathy. It was truly a great opportunity.

I am also thankful to Professor Gadegaard's group at University of Glasgow and Professor Tomaso Zambelli at ETH Zurich for welcoming me into their labs and teaching me so much.

To all the members of the Centre for the Cellular Microenvironment (CeMi), I feel especially lucky to have undertaken my PhD in such a friendly and welcoming lab. I could not have asked for a better group of people to work with. I am especially grateful to Justine, Rui Ling, and Rosalia for their friendship. Also, a special thanks to Dr Rosalia Cuahtecontzi Delint and Dr Jack Brennan for taking the time to provide me with constant thesis feedback during what seemed like a never ending write-up period.

I would also like to thank my mum and dad for their unconditional love, faith, and for always empowering my curiosity. To my siblings - Sehar, Zeeshan, and Zaman - for always being a constant source of strength and laughter.

Last, but not least, I thank my husband, Zyshan for his unwavering love and support. You were the one who encouraged me to begin this journey, and you have been my greatest source of support ever since. Thank you for constantly motivating me to persevere.

Abbreviations & Acronyms

2D *2 Dimensional*

3D *3 Dimensional*

ACTG2 *Smooth Muscle Actin Gamma 2*

AFM *Atomic Force Microscopy*

ARG, R *Arginine*

BSA *Bovine Serum Albumin*

Ca 2+ *Calcium*

CGN *CpG dinucleotide-rich codons*

CIPO *Chronic Intestinal Pseudo-obstructions*

DMEM *Dulbecco's Modified Eagle Medium*

DPBS *Dulbecco's Phosphate Buffer Soloution*

EGFR *Epidermal Growth Factor Receptor*

ECM *Extracellular Matrix*

ENS *Enteric Nervous System*

F-actin *Filamentous Actin*

FLNA *Filamin A*

FBS *Foetal Bovine Serum*

FFL *Force From Lipids*

FFF *Force From Filaments*

GI *Gastrointestinal Tract*
GelMa *Gelatin Methacryloyl*
G-actin *Globular Actin*

HSCR *Hirschsprung's Disease*
HDF *Human Dermal Fibroblast*
HIMSC *Human Intestinal Smooth Muscle Cells*
hNSPC *Human Neural Stem/Progenitor Cells*
HPA *Human Protein Atlas*
hTERT *Human Telomerase Reverse Transcriptase*

IPA *Ingenuity Pathway Analysis*

LMOD1 *Leiomodin 1*
LIG3 *Ligase III*
LAP *Lithium phenyl-2,4,6-trimethylbenzoylphosphinate*

MMIHS *Megacystis Microcolon Intestinal hypoperistalsis syndrome*
MYH11 *Myosin Heavy Chain 11*
MYLK *Myosin Light Chain Kinase*
MYL9 *Myosin Light Chain 9*

NAD+ *Nicotinamide Adenine Dinucleotide*

PCA *Principle Component Analysis*
PDMS *Polydimethylsiloxane*
PIPO *Paediatric Intestinal Pseudo-obstructions*

qPCR *Quantitative Polymerase Chain Reaction*

RT	*Room Temperature*
RPMI	*Roswell Park Memorial Institute 1640 Medium*
SRF	Serum Response Factor
VSCM	*Visceral Myopathy*
Wnt	*Wingless-related integration site*
YAP	*Yes-Associated Protein*

List of Figures

List of Tables

List of Equations

Thesis Outline

Chapter 1 presents the current understanding of visceral myopathy and introduces the aims and objectives of the thesis.

Chapter 2 describes the thesis design including the cell lines used, as well as outlining the general materials and methods utilised to carry out the work presented in this thesis.

Chapter 3 describes visceral myopathy in the context of intestinal force and mechanotransduction. It explores the use of YAP and traction forces exerted by cells as disease biomarkers for drug screening or diagnostic assays. The work in this chapter is centred around *ACTG2* associated visceral myopathy, healthy controls, and controls based on non-*ACTG2* CIPO disorders (*LIG3*-chronic intestinal pseudo-obstruction and Hirschsprung's disease). The traction forces work was carried out in collaboration with Professor Nikolaj Gadegaard's group at the University of Glasgow.

Chapter 4 explores cell morphology, actin cytoskeleton dynamics, molecular clutch engagement, and cell migration in *ACTG2* associated visceral myopathy, healthy controls, and controls based on other non-*ACTG2* CIPO disorders (*LIG3*-chronic intestinal pseudo-obstruction and Hirschsprung's disease). Moreover, this chapter explores the use of migration as a biomarker for diagnostic and therapeutic purposes.

Chapter 5 describes the mechanosensitive ion channel, Piezo1 and concentrates on the novel *PIEZO1* mutations causative of visceral myopathy, identified in Sant'Orsola-Malpighi Polyclinic, Bologna, Italy. It reports on the morpho-mechanical and metabolic profile of *PIEZO1* associated visceral myopathy, as well as comparing differences between *PIEZO1*-VSCM, healthy control cells, and visceral myopathy caused by *ACTG2*.

Chapter 6 summarises and contextualises the main findings of this thesis. Furthermore, it outlines the limitations and highlights future work which could follow on from this thesis.

Contents

1 | Introduction

This thesis aims to provide as complete as possible picture of the myopathic intestinal pseudo-obstruction, known as visceral myopathy (VSCM). VSCM is a rare and severe motility disorder of the gastrointestinal tract which affects 1 in 100000 individuals [1]. Overall, the disease lacks fast and certain diagnosis, whilst no pharmacological therapy exists.

The introduction to the thesis will serve as an overview to the nomenclature issue and the unmet medical needs of the pathology, which mainly regards its diagnosis and therapy. There will be an extensive focus on the genetic basis of the disease, the current knowledge at biophysical and biomolecular levels, and the existing models for studying this pathology. The overall scope is to orchestrate available knowledge on VSCM to provide a comprehensive and harmonised picture of the disease before embarking on the study of VSCM from a mechanobiology point. The primary aim of the thesis is to support further investigations, which are crucial to advance in the solution of the main VSCM-related challenges of diagnosis and therapy.

1.1 A nomenclature muddle

Motility disorders of the gastrointestinal tract leading to intestinal pseudo- obstruction vary in their severity and frequency. Rare gastrointestinal dysmotility disorders presenting similar, severe consequences include chronic intestinal pseudo-obstructions (CIPO; ORPHA:2978), paediatric intestinal pseudo- obstructions (PIPO), visceral myopathy (VSCM; OMIM #155310) and megacystis microcolon intestinal hypoperistalsis syndrome (MMIHS; OMIM #249210) [1–3]. The nomenclature surrounding these disorders is not clearly defined. The above terms are used to describe different diseases, as reported in the OMIM and Orphanet databases, but, due to partial overlap among symptoms, on occasion multiple terms have been used to describe the same disorder. This results in a layer of complexity, additional to the rareness and severity of these pathologies. This thesis will focus on VSCM, the myogenic form of CIPO. However, a brief overview on the rare disorders mentioned above - CIPO, PIPO and MMIHS - will be presented.

CIPO is one of the most commonly used terms to describe defects in peristalsis. It is caused by impairments in the propulsive activity of the gastrointestinal tract without the presence of mechanical obstructions [3,4]. CIPO can be divided into three main categories: neuropathies, mesenchymopathies and myopathies. This depends on the genes causative of the disease, in which cell types they are expressed, and the underlying pathogenetic mechanisms. Neuropathies are caused by a genetic defect in the enteric neurones innervating intestinal smooth muscle, and include, as the most recurrent, Hirschsprung's disease (HSCR); mesenchymopathies are due to defects in interstitial cells of Cajal promoting muscle contraction; while myopathies involve defects of the smooth muscle cells [5–8]. Often the term CIPO has been extended to describe VSCM and MMIHS [8,9].

PIPO is primarily a term which describes chronic intestinal pseudo-obstruction in infants. Experts, including those from the European Society for Paediatric Gastroenterology, Hepatology, and Nutrition, published a report recommending the consideration of PIPO as a separate disorder from CIPO when present in infants and children [1]. This is because intestinal obstruction is thought to present itself differently in children compared to adults [1,10–12]. Nevertheless, the term CIPO is frequently also used for early age onset.

MMIHS, also known as Berdon syndrome, is an autosomal recessive disorder which impairs the gastrointestinal motility and affects new-born children, with major prevalence in females than males [2,13]. It is caused by defects in the muscle cells. Individuals suffering from this disorder have enlarged bladders, microcolon as well as motility dysfunction of the whole intestine [2,14].

VSCM is defined as a rare intestinal motility disorder which presents impaired intestinal function and motility in the absence of mechanical obstruction. The disorder mainly occurs in infants, however, it can also affect children and adults. VSCM is often described as a myogenic form of CIPO as it is caused by defects regarding the enteric smooth muscle cells [8,15], therefore being frequently included under the CIPO family of diseases [16,17]. The main differences between VSCM and MMIHS rely on the age of onset (MMIHS can be diagnosed prenatally due to a recognisable bladder distension while VSCM can occur later) and disease severity (most MMIHS patients surviving days or months after birth) [18]. Nevertheless, sometimes, the word 'VSCM' has been used as an umbrella term to include all myogenic chronic intestinal pseudo-obstructions, such as CIPO and MMIHS, which often are described (not always obtaining consensus) as different phenotypes of VSCM [7,17].

1.2 Visceral myopathy

1.2.1 An unmet medical need

VSCM primarily affects young children but on occasion has been identified in adults. The main indicators associated with the disease are abnormal intestinal function, malnutrition, abdominal discomfort, and challenges with food intake [8, 19]. VSCM is a rare genetic disease, presenting diverse degree of severity in gastrointestinal motility disorder. The severity of VSCM can differ widely, with the extreme cases leading to intestinal failure and potentially fatal outcomes [19]. The disorder is characterised by recurring episodes which resemble mechanical obstruction without any physical obstruction. This is attributed to the compromised contractile function of the smooth muscle cells which line the walls of the gastrointestinal tract [8, 9].

The walls of the gastrointestinal tract are lined with an outer longitudinal and inner circular layer of smooth muscle cells which have a critical role in gastrointestinal motility [20, 21]. The function of these smooth muscle cells is coordinated by the enteric nervous system (ENS), which facilitates peristalsis and segmentation. Peristalsis propels intestinal contents along the intestine, while segmentation mixes these contents, enhancing the uptake of nutrient and water. Normally, these smooth muscle layers not only perform tonic contractions to maintain structural integrity under physical stress but also execute forceful contractions that drive the movement of the digestive bolus along the tract [22].

However, in the case of VSCM, this coordination is disrupted. Affected individuals exhibit impaired peristaltic and segmental motions due to degeneration and fibrosis of the smooth muscle cells. This disruption in muscle function leads to significant challenges in both the propulsion and the mixing of intestinal contents, crucial for effective digestion [19].

VSCM diagnosis is not straightforward and occurs through a combination of different clinical tests. Computed tomography scans or endoscopy are usually performed to exclude the presence of a mechanical obstruction in the gastrointestinal tract (GI) [23, 24]. Specialised tests such as manometry are used to examine intestinal motility. Moreover, biopsies can be taken to allow clinicians to look: 1. at histology, in order to verify the presence of correct muscle tissue innervation, thus excluding ENS responsibility in the lack of peristalsis (as in the case of HSCR); and 2. at histopathology, to investigate tissue and/or cellular abnormalities [24, 25]. However, a gap in knowledge of intestinal tissue and nerves conformation often prevents histopathological analysis from highlighting abnormalities between VSCM and normal intestines [26]. When clinical examination leads to hypothesise that an individual has VSCM, confirmatory genetic tests are performed, which demonstrated to be the only effective method of diagnosis, especially for highlighting the primary cause of CIPO, either neurogenic, mesenchymogenic or myogenic. Usually, these tests rely on Sanger sequencing of VSCM major candidate gene, smooth muscle actin gamma 2 (*ACTG2*) [27, 28]. When no mutations are found in this gene, gene panels or clinical or whole exome sequencing are performed, to analyse if variants are present in other genes reasonably involved in the mechanical feature of the cells. Also, in a few cases whole genome sequencing is carried out, to shed light on other possible genetic causes associated to non-coding regions or to structural variants [28–30].

Furthermore, for around 40% of patients with VSCM-like symptoms, no genetic driver has emerged so far [28, 30], thus individuals remain without a certain diagnosis. This is due to a crucial bottleneck in VSCM diagnosis which remains as a result of the partially unveiled genetic scenario underlying the pathology.

Difficulties in the VSCM treatments are even harder than those related to its diagnosis. Currently, treatment choices are extremely limited, and always involving invasive options. At present, there is no gastrointestinal motility drug to treat VSCM, and the only pharmacological options show symptomatic rather than curative effects, focusing on controlling intestinal inflammation, suppressing bacterial overgrowth, promoting gastrointestinal motility, reducing the severity of nausea, and vomiting [31]. Such drugs are often associated with unacceptable extra-intestinal side-effects, and tolerance can be impacted as the disease progresses. In order to handle acute events, surgical removal of the intestinal obstruction and intestinal resection is performed [24]. To avoid recurrent obstruction, total parenteral nutrition and catheterization are strongly suggested, thus condemning patients to a low-quality life. In the past, intestinal transplantation represented an attempt to provide an additional possibility of life for patients [32]. Nevertheless, more recently this method has been discouraged: due to the high percentage of consequent deaths, it does not represent a treatment option anymore [33]. Preliminary studies of novel treatment options such as faecal bacterial transmutation show to be a promising treatment option to alleviate symptoms and would be beneficial to explore further [26, 34].

1.2.2 The genetics of VSCM

The genetics underpinning VSCM are not fully understood. The primary genes linked with VSCM are genes for the cell contractile apparatus, thus suggesting a significant mechanical component to the disease.

Variants in the *ACTG2* gene are found in 40%-45% of patients. Furthermore, causative genetic variants identified in other genes account for about 10% of cases that exhibit similar symptoms. Yet, for more than 40% of patients, the precise genetic factors remain unknown, pointing to the possibility of other genes. The rarity of VSCM complicates early and accurate diagnosis and hinders the development of treatments. Currently, the only options are highly invasive, such as total parenteral nutrition and ostomies to facilitate gut emptying, emphasising the need for alternative therapies.

Actin Gamma 2 (*ACTG2*)

For the purposes of this thesis, appropriate variants published under myopathic CIPO, PIPO, and MMIHS will also be considered as a contributor to VSCM. Taking this into consideration, currently, publications point *ACTG2* variants as the main genetic contributor for VSCM. The *ACTG2* gene presents as the primary genetic contributor to VSCM, with evidence suggesting, 40-50% of cases are *ACTG2*-positive [27]. *ACTG2* gene is found on chromosome 2 and it consists of 9 exons. The gene codes for a 376 amino acid protein called actin gamma 2 protein which is a globular, monomeric form of actin found in enteric smooth muscle.

ACTG2 variants are mostly heterozygous, missense single nucleotide mutations that most likely alter protein function by affecting actin polymerisation and cell contractility.The exact mechanism by which *ACTG2* mutations alter protein function is not fully established. Studies have shown that actin polymerisation is affected however this will be discussed in more detail in the context of actin retrograde flow results explored in Chapter 4 [18, 35]. Additionally, VSCM has resulted in diminished cell contractility which is discussed in more detail in Chapter 3. Figure 1.1a shows the location of VSCM causing variants on the *ACTG2* gene and Table 1.1 provides greater detail on the known variants.

Familial mutations which have an autosomal inheritance pattern result in late onset VSCM, whereas, heterozygous de novo mutations have been reported to cause congenital VSCM [1, 15, 28, 36, 37]. Arginine (Arg, R) residues are primarily affected in the majority of heterozygous mutations linked to *ACTG2* associated VSCM, with changes to Arg residues accounting for 79% of *ACTG2* positive cases 1.1b. Disease severity is associated with the specific arginine residue affected [27, 36]. Furthermore, these mutations frequently occur at CpG dinucleotides, predominantly a result of the conversion of methylated cytosine (5mC) to thymine [15, 27]. This is often seen because of the arginine codon bias that tends to favour these mutable CpG dinucleotide-rich codons (CGN) across genes [15, 38].

Mutations in R178 are associated with the most extreme from of VSCM due to the critical role of R178 in inter-domain contacts. Moreover, the most frequently occurring mutation which causes VSCM are in the residue R257 and these also bring about a severe form of the disorder [15,27]. Batzir *et al.,* reported a spectrum of phenotypic disease severity for *ACTG2* Arg mutations, with R178 being the most severe, then R257, and milder forms of the disease observed in individuals with mutations in R40 and R38 [27]. Additionally, severe cases of VSCM have been reported with mutations in R63, R40, R211, T149, and E196 [27,37]. Specifically, the T149R substitution highlights that both the substitution and addition of Arg residues can profoundly impact ACTG2 function. Conversely, variants H41Q and L143F are linked to milder symptoms [37].

Recent studies have highlighted that individuals with VSCM caused by autosomal recessive *ACTG2* variants are more severe than their heterozygous counterparts [39, 40]. This disparity in disease severity is consistent across all reported homozygous *ACTG2* variants associated with causing VSCM. These homozygous recessive variants are: V10M, R168*, R211*, R336W, and an exon 6 - intron 6 spanning deletion. Variants V10M, R168*, R211*, and R336W appear in both monoallelic and biallelic forms, but only the biallelic form is pathogenic. Whilst the monoallelic forms are associated with mild gastrointestinal symptoms, primarily chronic constipation [37, 39–41].

Moreover, the effects of heterozygous deletions remain unclear, whilst, homozygous exon deletions have been found to cause severe forms of VSCM. For example, a heterozygous deletion of the non-coding exon 1 was not identified as non-pathogenic. In contrast, a severe case of VSCM, caused by a homozygous deletion spanning the boundary of exon 6 and intron 6 (c.589_613+163del188), was identified to cause VSCM [39, 40]. Additionally, there have been no reported cases of VSCM caused by compound heterozygous mutations.

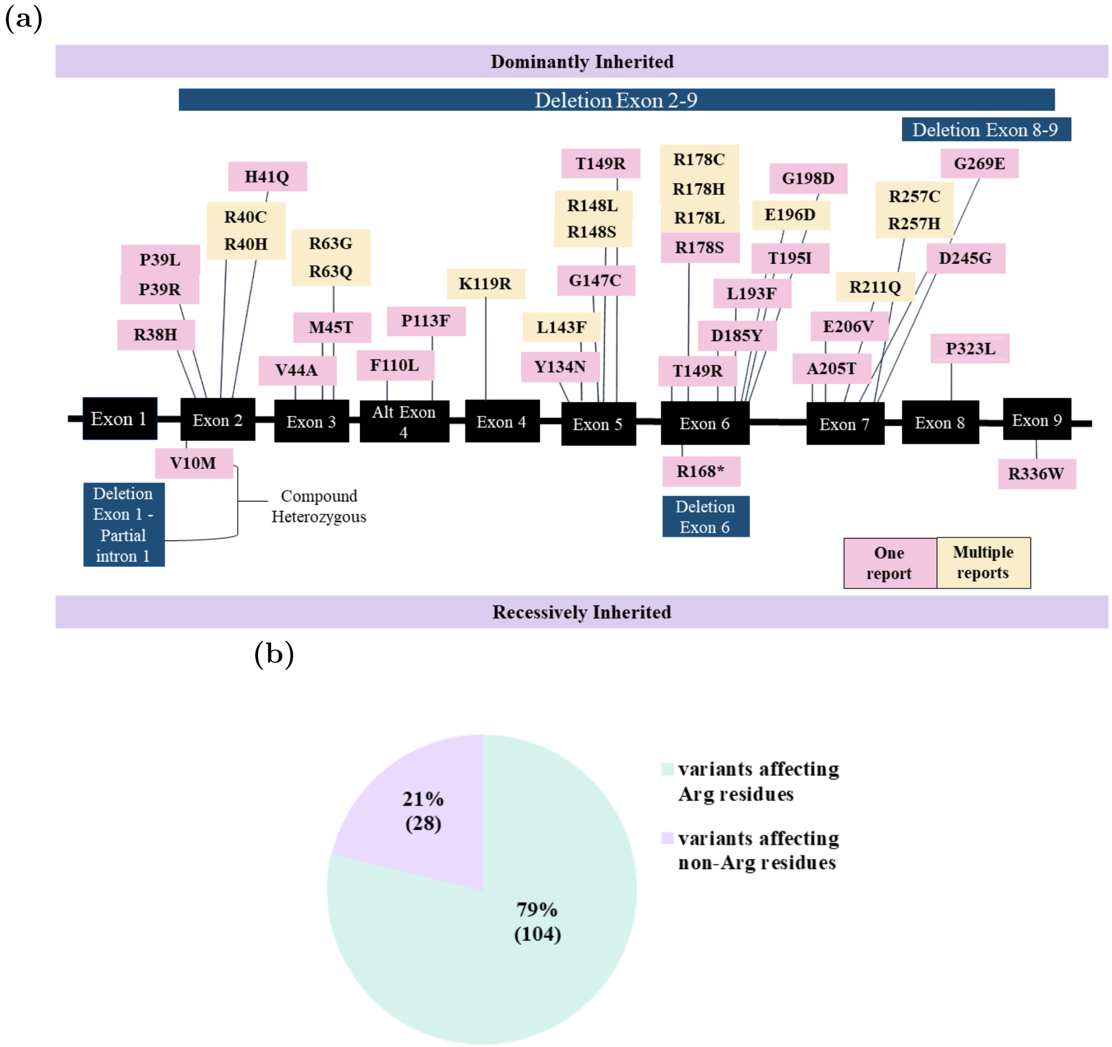

Figure 1.1: Illustrative summary of VSCM caused by variants affecting *ACTG2* gene. (a) Schematic of *ACTG2* gene showing exons with location of reported variants. Exons are outlined in black. Variants that are reported once shown in pink, variants reported multiple times in yellow, and deletions in blue. Dominantly inherited mutations are illustrated on top of exons and recessively inherited mutations are listed underneath exons. (b) Variants impacting argenine residues.

Nucleotide	**Variant**	**Alleles**	**Inheritance**	**Mutation**	**Condition**	**Publications**
c.113G>A	R38H	Heterozygous	AD	Missense	CIPO	[36]
c.116C>T	P39L	Heterozygous	AD	Missense	VSCM	[27]
c.116C>G	P39R	Heterozygous	AD	Missense	CIPO	[42]
c.118C>T	R40C	Heterozygous	AD	Missense	VSCM	[15, 18, 27, 43]
c.119G>A	R40H	Heterozygous	AD	Missense	VSCM/ CIPO/PIPO	[15, 27, 28, 37, 43]
c.123C>A	H41Q	Heterozygous	AD	Missense	VSCM/ PIPO	[37]
c.131T>C	V44A	-	-	-	MMIHS	[27]
c.134T>C	M45T	Heterozygous	De novo	Missense	VSCM	[15, 27]
c.187C>G	R63G	Heterozygous	AD	Missense	VSCM	[15, 27, 28]
c.188G>A	R63Q	Heterozygous	AD	Missense	VSCM/PIPO	[18, 27, 44]
c.330C>A	F110L	Heterozygous	AD	Alternative Exon 4	VSCM	[15]
c.337C>T	P113S	Heterozygous	De novo	Missense	PIPO	[45]
c.463A>G	K119R	-	De novo	-	VSCM/ ADL	[46]
c.412T>A	Y134N	Heterozygous	De novo	Missense	MMIHS	[15, 27]

Continued on next page

Table 1.1 – continued from previous page

Nucleotide	Variant	Alleles	Inheritance	Mutation	Condition	Publications
c.427C>T	L143F	Heterozygous	-	Missense	PIPO	[27, 37]
c.439G>T	G147C	Heterozygous	AD	Missense	VSCM	[47]
c.443G>T	R148L	Heterozygous	AD	Missense	VSCM	[43, 45]
c.446C > G	T149R	Heterozygous	De novo	Missense	PIPO	[37, 48]
c.532C>T	R178C	Heterozygous	AD	Missense	VSCM/ MMIHS	[15, 36, 49, 50]
c.533G>A	R178H	Heterozygous	AD	Missense	VSCM/ MMIHS	[27, 44, 49, 51]
c.533G>T	R178L	Heterozygous	AD	Missense	VSCM/ MMIHS	[15, 49, 50]
c.532C>A	R178S	Heterozygous	De novo	Missense	MMIHS	[52]
c.553G>T	D185Y	Heterozygous	De novo	Missense	PIPO	[45]
c.577A>T	L193F	Heterozygous	De novo	Missense	CIPO	[44]
c.584C>T	T195I	Heterozygous	-	Missense	CIPO	[17]
c.588G>C	E196D	Heterozygous	De novo	Missense	PIPO	[37, 45, 53]
c.593G>A	G198D	Heterozygous	De novo	Missense	VSCM	[15]
c.613G>A	A205T	-	AD	Missense	VSCM	[54]
c.617A>T	E206V	Heterozygous	AD	Missense	CIPO	[55]
-	R211Q	-	AD	Missense	VSCM	[27, 55]

Continued on next page

Table 1.1 – continued from previous page

Nucleotide	Variant	Alleles	Inheritance	Mutation	Condition	Publications
c.734A>G	D245G	Heterozygous	De novo	Missense	PIPO	[45]
c.769C>T	R257C	Heterozygous	AD	Missense	VSCM/MMIHS	[15, 27, 36, 37, 43–45]
c.770G>A	R257H	Heterozygous	AD	Missense	VSCM/MMIHS	[17, 36, 45]
c.806_807 del	G269E	Heterozygous	-	Deletion	VSCM	[56]
c.968C>T	P323L	Heterozygous	AD	Missense	CIPO	[55]
c.28G>A	V10M	Heterozygous	-	Missense	PIPO	[40]
exon 8-9 del	-	Heterozygous	-	Deletion	CIPO	[42]
c.589_613, 163del18	-	Homozygous	AR	Deletion	-	[39]
6.8 kb del at 2p13.1	-	Homozygous	AR	Deletion	PIPO/MMIHS	[40]
-	R168*	Homozygous	AR	Missense	-	[41]
c.1006C>T	T336W	Homozygous	AR	Missense	VSCM	[37]
Truncating	R211*	Homozygous	AR	Missense	VSCM	[36]

Table 1.1: *ACTG2* variants in VSCM. Information on *ACTG2* associated variants of VSCM. CIPO = chronic intestinal pseudo-obstruction; VSCM = visceral myopathy; PIPO = paediatric intestinal pseudo-obstruction; MMIHS = megacystis microcolon intestinal hypoperistalsis syndrome; AD = autosomal dominant; AR = autosomal recessive; del = deletion.

ACTG2 protein and related cell phenotype

A key characteristic of smooth muscle cells is their slow involuntary contractions and relaxations. This is due to the cells contractile apparatus and cytoskeleton [57]. To generate force and contract, smooth muscle cells contain actin-myosin filaments, obliquely arranged: filamentous actin (F-actin), which is generated by polymerisation of globular actin (G-actin) monomers, is anchored by dense bodies and connected to the extracellular matrix; the myosin contribution is provided by myosin heavy chains. During force production, the F-actin network is regulated by proteins that nucleate, elongate, cleave, branch, and bundle filaments into stress fibres [58, 59].

ACTG2 is the primary actin isoform in smooth muscle cells of the urinary and intestinal tracts [18]. It appears important especially in dynamic submembranous actin network that links extracellular matrix to cytoskeleton and polymerises in response to a contractile stimuli [58, 60]. The actin cytoskeleton has many roles within eukaryotic cells. It is involved in muscle contraction, regulating cell shape, cell motility, and numerous essential cellular processes such as organelle transport [58,61]. *ACTG2* plays a key role in the contractile apparatus of the enteric smooth muscles, which enables expelling urine from the bladder and moving food through the intestines as part of the digestive process [48]. In particular, it has been shown that ACTG2 presence is necessary for the controlled dilatation of various muscular structures [57].

ACTG2 associated VSCM pathogenic mechanism is still unknown, although a series of mechanisms have been hypothesised, including alterations in actin filament polymerisation, stability, regulation of filament dynamics via actin regulatory proteins, and altered interactions of the filaments with myosin or a decreased ability to withstand the force applied to the actin filaments during myosin mediated contraction [62].

Changes of residues in ACTG2 seem to reflect into enteric smooth muscle cells morpho-mechanical dysfunctions, thus being potentially able to lead to the signs and symptoms of VSCM condition. In order to study the effects of *ACTG2* mutations on the protein structure, in-silico models of the protein were developed, to help in disease stratification and in pathogenesis mechanism identification [18, 49, 56, 59].

These in-silico models helped to prove the severity of different forms of VSCM. Based on the root-mean square displacement factor, Halim *et al.,* found that ACTG2 structures presenting R178C and R40C mutations resulted respectively the most and the least deviated structures compared to wild-type ACTG2, leading to hypothesise associated severe and mild symptoms, respectively [18]. These findings were confirmed by Batzir *et al.,* who proposed the following path of decreasing severity: p.R178>p.R257>p.R40. R257C mutation was investigated through molecular modelling by Hashmi and colleagues, who assessed that effects of the mutation on ACTG2 secondary structure could be not dramatic [27, 59]. Nevertheless, they noticed that the normal F-actin molecule had a steric clash between R257 and F223, which is not present in the mutated ACTG2 f-actin, with potential implications for filaments structure, that was confirmed by fluorescence microscopy. Klar *et al.,* studied the crystal structure of ACTG2 carrying G269E mutation to predict the pathophysiological significance of the variant at a protein level [56]. Their results showed that distances between the 269 residue and residues in its close proximity of the adjacent actin monomers vary when the uncharged glycine is replaced by the larger and polar glutamic acid, suggesting a possible effect on the actin polymer and a perturbation of filaments polymerisation and/or stability, although not confirmed. Recently, relying on ACTG2 molecular modelling, Matera and colleagues proposed additional interesting insights on disease stratification. They highlighted that the break of hydrogen bond and salt bridge between R257 and E196, typical of R257C and E196D mutations, give heavy molecular consequences that can reflect in some of the most severe disease phenotypes [37].

Being directly related to ACTG2 structure, actin polymerisation and cytoskeleton organisation in presence of *ACTG2* mutations result to be the most investigated aspects to shed light on VSCM pathogenic mechanism. Polymerisation of the actin cytoskeleton plays a central role in the development of tension and the spreading of forces from the cytoskeleton to the extracellular matrix and the surrounding cells, and therefore it is observed as potentially involved in the pathogenic mechanism. Relying on in-silico structural analysis, Thorson *et al.,* sustained that the R178L and R178C mutations would likely impair polymerisation of ACTG2 into thin filaments, and found that these ACTG2 mutants showed a diffuse localisation and a poor association with actin filaments [49]. Similar findings were obtained through fluorescence on cell culture and co-sedimentation approaches, showing that, while wild-type ACTG2 could incorporate into the actin filaments, no co-localisation was observed for *ACTG2* in presence of R178C, R178L, R178H, R40C, R63Q, R148S mutations, and that this could reflect in impaired actin polymerisation and in changes in the overall actin organisation [18]. Analogous conclusions on R148S mutation were obtained by Lehtonen and colleagues who, relying on fluorescence staining of fixed cells, found that mutated ACTG2 exhibited predominantly diffuse localisation and weak association with the actin-based structures (such as contractile stress fibres) [8]. Moreover, an abnormal myosin II incorporation resulted into these structures of localisation. Working on smooth muscle cells carrying R257C ACTG2 mutation, and fluorescently labelling ACTG2 and f-actin, Hashmi and colleagues did not highlight any profound disruption of overall organisation of the actin cytoskeleton networks in mutant cells compared to the wild-type [59]. On the other hand, they found differences in filament structure: ACTG2 carrying R257C mutation was incorporated into fewer, shorter, thinner, and less branched f-actin bundles compared with the wild-type protein. Using transmission electron microscopy on a biopsy from a patient carrying G147C mutation in *ACTG2*, Collins *et al.,* found disorganised aggregates of 9nm to 11nm actin filaments in smooth muscle cells [47]. Overall, results on effects of *ACTG2* mutations on actin polymerisation do not provide a clear consensus: this could suggest that different variants lead to diverse levels of impairments on actin bundles and related disease symptoms, or partially diverse results could be due to the exploitation of different experimental models, such as different cell lines. The actin polymerisation effects are still unclear, thus contribute to confusion on the mechanisms underlying the lack of smooth muscle contraction experienced in presence of VSCM.

Nevertheless, the issue at a cytoskeletal level was also proved through experiments on cell morphology by Hashmi *et al.,*. Differences were identified between wild type and R257C mutant cells: the latter appeared 20% less circular in shape and had 11% wider diameter [59].

The reduced cell contractility, typical of VSCM, has led to the investigation of mechanical properties at a cellular level. This requires further work, especially due to the findings of impairments in actin polymerisation and abnormal actin bundle formation, which impact on the cytoskeleton and cell mechanical characteristics. Thus, providing the physical basis of the reduced contractility of enteric smooth muscles in VSCM patients.

Collagen gel contraction assays were used to determine if mutant cells present different contraction ability compared to wild-type. Such tests showed statistically significant impairments in presence of R178H, R178C, R178L and R148S mutations, while this mechanical feature does not seem compromised when cells are affected by R40C, R63Q and R257C [8,18,49,59]. Further functional examination of wild-type and R257C-mutated ACTG2 human intestinal smooth muscle cells showed that also other aspects of the cell mechanical environment are affected by this mutation presence. Cells migrated 11% faster and spread over a 21% greater area compared to wild-type cells [59]. Findings on decreased cell contractility coupled to improved cell migration in presence of R257C variant can be explained considering that the two mechanical phenomena rely on different smooth muscle cells components.

Collectively these findings suggest that mutations involved in the most severe forms of VSCM impact ACTG2 structure, with potential effects of f-actin filaments and with almost certain impairment of morpho-mechanical cell features. The dominant negative nature of the disease suggests that sequestration occurs of actin regulatory proteins by the dysfunctional actin monomers, preventing their participation in normal actin filament regulation [62]. ACTG2 is thought to be involved in regulating mechanical features of smooth muscle cells such as cell migration, cell spreading, cell contraction and resistance to passive stretch [59]. Although not totally clear yet, the idea that *ACTG2* mutations characterising VSCM could impact on cell mechanical function is promising, and that such affected cell phenotype could be responsible of the mechanical disabilities in the visceral organs exhibited by VSCM affected patients.

Additional genes linked to VSCM

Genes aside form *ACTG2*, appear to contribute to VSCM cases. This is evident as around 40% of cases do not have a genetic cause linked to them [63]. For the majority of these cases the genetics behind the disorder are unclear. However, for 10% of VSCM cases, the following cell contractile apparatus genes have been identified; myosin light chain 9 (*MYL9*), myosin light chain kinase (*MYLK*), myosin heavy chain 11 (*MYH11*), and Filamin A (*FLNA*), and Leiomodin 1 (*LMOD1*) [30, 48, 50, 51, 63–68]. Smooth muscle myosin proteins are coded by *MYLK*, *MYL9*, and *MYH11*. These gene, either directly (*MYL9 and MYLK*), or indirectly (*MYH11*), facilitate muscle contractions [48, 63, 67, 68]. Moreover, *LMOD1* is involved in the nucleation of actin filaments and *FLNA* promotes actin binding [69, 70].

1.2.3 Animal models

VSCM-like symptoms have been induced in Serum response factor (SRF) knockout mice, myocardin knockout mice and Kindlin-2 knockout mice [71–73]. These models have been characterised. However to date, no mice models have been utilised to investigate VSCM [63].

In order to achieve a thorough understanding of the mechanisms underlying VSCM, and to test the effectiveness of potential therapeutic molecules, models mimicking the pathology are needed, coupled to functional tests able to verify the experimental hypothesis. In particular, Rubenstein and Mayer suggested that models expressing a single actin type would be extremely beneficial, to study the effect of the mutation in an undiluted context [62]. In this sense, they highlighted budding yeast as a potentially successful model, for similarity among its single actin and the mammalian smooth muscle actins (about 87% identical), and because yeast shares many actin-binding proteins with mammalian cells. Yeast could represent an *ACTG2* high-performance purification system with properties of the mutant actin, alone and in conjunction with different regulatory proteins. This can be assessed *in vitro*, and successively verified *in vivo*, to move further to higher cell types such as mammalian cells [62]. Nevertheless, at the time of this thesis, no yeast model exists for VSCM.

1.2.4 Neurogastrointestinal disorders

As previously mentioned, the CIPO family includes neuropathies such as ligase III (LIG3) associated CIPO and Hirschsprung's disease (HSCR) [74, 75]. Patients with these disorders exhibit similar intestinal symptoms to VSCM but have also exhibited neurological symptoms, such as epilepsy, migraines, and leukoencephalopathy [74, 76, 77].

The *LIG3* gene codes for a DNA ligase which is involved in the maintenance and replication of mitochondrial DNA through interactions with mitochondrial polymerase and replisome factors [74, 78–80]. Mutations in *LIG3* lead to mitochondrial dysfunction and impact the metabolic profile of cells [74]. Moreover, HSCR is defined by the lack of enteric ganglion cells along the specific regions of the intestines (myenteric and submucosal plexuses of the distal intestine) [75]. Currently, the 'Rearranged-during transfection' (*RET*) gene has been identified as the primary genetic cause of the disease. Additionally, *EDNRB*, *EDN3*, and *SOX10* genes have also been linked to causing HSCR [81]. However, as in VSCM, the genetics behind HSCR are poorly understood.

In this thesis, *LIG3*-CIPO and HSCR were used as controls against VSCM. This is due to individuals with these neurogastrointestinal disorders presenting with similar intestinal symptoms but differing in the genetics.

1.3 Aims and objectives

The primary aim of this project was to gain a deeper understanding of VSCM pathogenesis by investigating the mechanical and molecular basis of the disorder. This was carried out through exploration of how physical forces and changes in the mechanical properties of cells contribute to the physiology and development of VSCM. Firstly, the mechanical phenotype of *ACTG2* associated VSCM was investigated to identify physical biomarkers which can be further exploited for diagnostic assays and therapeutic purposes. Furthermore, *PIEZO1* associated VSCM was studied to evaluate whether VSCM caused by *PIEZO1* mutations is similar, at a molecular and biophysical level, to VSCM caused by *ACTG2* variants.

This thesis assessed YAP nuclear localisation in VSCM in comparison with healthy controls to determine whether the loss of contractility in the intestine impacts YAP localisation. This is followed by the exploration of force based assays to identify one that is able to exploit the use of forces as a biomarker for VSCM. Furthermore, the assessment of migration as a physical biomarker for VSCM is studied which includes an investigation into the morpho-mechanical features as well as the molecular clutch dynamics of VSCM associated cells. Moreover, the differences between VSCM caused by novel *PIEZO1* mutations and that by *ACTG2* variants are investigated. The morpho-mechanical features of *PIEZO1*-VSCM cells will be analysed and a comparison carried out against healthy control cells as well as *ACTG2*-VSCM cells. This is followed by the exploration of the metabolomic profile of VSCM caused by *PIEZO1* mutations and by *ACTG2* variants to assess changes in metabolites and biochemical pathways in VSCM.

2 | Materials & Methods

2.1 Thesis design

To carry out the work in this project, several variants associated with VSCM were studied, including *ACTG2* variants and two biallelic causative variants of *PIEZO1*. Table 2.1 provides an overview of the control and mutant cells studied in this thesis. Two *ACTG2* variants were investigated, R257C and R38H, from which one sample was from an individual with VSCM caused by R38H and two samples were from two individuals with VSCM caused by R257C. The R257C variant results in a severe form of VSCM, whereas individuals with R38H variant have a mild form of the disease. In this thesis, all three *ACTG2*-VSCM cell lines will be analysed collectively, as well as separately, depending on disease severity. Additionally, biallelic variants, S1814F (c.5441C>T) and P2230L (c.6689C>T), in *PIEZO1* were identified in two siblings who had healthy parents, in Sant'Orsola - Malpighi Polyclinic, Bologna Italy. The variants were heterozygous missense variants and resulted in symptoms similar to individuals with VSCM caused by *ACTG2* variants. However, it should be noted that only one sample was available for study.

Moreover, four samples from patients with no gastrointestinal disorder or no known health conditions were used as controls to compare against the VSCM samples. Furthermore, additional controls were set up to determine whether VSCM could be distinguished from other gastrointestinal disorders which are not myogenic in nature such as HSCR and *LIG3* associated CIPO. There were two samples for the HSCR control group and one for *LIG3*-CIPO controls.

Furthermore, during the optimisation stage of the collagen and GelMa contractility assays (Chapter 3, section 3.3.4 and section 3.3.6), work was carried out on the commercially available dermal fibroblasts; human telomerase reverse transcriptase (hTERT) cell line. This was due to the large number of cells that were needed for the optimisation of the protocol. It would not have been feasible to use primary HDFs for this purpose, thus, the immortalised cell line was utilised.

For the purposes of this thesis, all work (bar collagen contraction optimisation) was carried out on primary human dermal fibroblast cells (HDF) from individuals with VSCM. The HDF cells were chosen as a model for VSCM due to previous work that was undertaken, in collaboration with Viti and colleagues, as a precursor to this project, which showed that the enteric *ACTG2* gene was expressed in dermal fibroblasts as well as demonstrating that the disease phenotype could be monitored in HDFs [82]. Although, it would be beneficial to use intestinal cells as the model to study VSCM, the procedure to obtain such cells is invasive and can result in complications to individuals with VSCM, thus was avoided.

Table 2.1: List of cells

ID	Phenotype	Culture media	Hospital	Notes
C1	Control	DMEM	Sant'Orsola-Malpighi	No known health condition
C2	Control	RPMI	Giannina Gaslini Institute	No GI health condition
C3	Control	RPMI	Giannina Gaslini Institute	No GI health condition
C4	Control	RPMI	Giannina Gaslini Institute	No GI health condition
S1	Severe VSCM	RPMI	Giannina Gaslini Institute	R257C *ACTG2* mutation
S2	Severe VSCM	RPMI	Giannina Gaslini Institute	R257C *ACTG2* mutation
M1	Mild VSCM	RPMI	Giannina Gaslini Institute	R38H *ACTG2* mutation
P1	VSCM	DMEM	Sant'Orsola-Malpighi	S1814F & P2230L *PIEZO1* mutations
LC	LIG3-CIPO	RMPI	Giannina Gaslini Institute	*LIG3* mutation
H1	HSCR	RPMI	Giannina Gaslini Institute	No *RET* mutation
H2	HSCR	RPMI	Giannina Gaslini Institute	R275W *RET* mutation
hTERT BJ-5ta	Immortalised	DMEM	-	From AATC height

2.2 Materials

The materials used for the work carried out in this thesis are listed in the tables below.

Table 2.2: List of cell culture reagents

Reagent	Product	Provider	Notes
Roswell Park Memorial Institute 1640 Medium	21875034	ThermoFisher (Gibco)	RPMI
Dulbecco's modified Eagle's medium	41966029	ThermoFisher (Gibco)	DMEM
Penicillin/Streptomycin	15140122	ThermoFisher (Gibco)	P/S
Foetal Bovine Serum	F9665	Sigma-Aldrich	FBS
L-Glutamine	G7513	Sigma-Aldrich	-
Non-essential amino acids	11140-035	ThermoFisher	
Fungizone	15290-026	ThermoFisher (Gibco)	-
Trypsin-Neutralizer Solution	R-002-100	ThermoFisher (Gibco)	Diluted in HEPES 1:40
HEPES	C-40000	Promo Cell	-
Trypan Blue	T8154	Sigma-Aldrich	-

Table 2.3: List of antibodies and other reagents used for staining cells

Reagent	Product	Provider	Notes
Phalloidin	A12379	ThermoFisher	Dilution 1:250
Mouse-anti-Vinculin (monoclonal)	V9131-100ul	Sigma-Aldrich	Dilution 1:400
Mouse-anti-YAP (monoclonal) (H-9)	SC-271134	Santa Cruz Biotechnology	Dilution 1:100
Rabbit-anti-mouse-Cy3 (Polyclonal)	315-165-003	Jackson ImmunoResearch	Dilution 1:200
SPY555-FastAct	SC205	Spiro Chrome	Dilution 1:1000
Bovine Serum Albumin	A7979	Sigma-Aldrich	BSA
Triton-X100	T8787	Sigma-Aldrich	-
Tween 20	P2287	Sigma-Aldrich	-
VectaShield with DAPI	H-1200-10	Vectorlabs	-

Table 2.4: List of reagents used in collagen hydrogels

Reagent	Product	Provider	Notes
Rat tail collagen type 1	60-30-810	First Link UK	-
10X DMEM	D2429	Sigma-Aldrich	-
0.1M NaOH	43617-1L	Sigma-Aldrich	-

Table 2.5: List of reagents used in gelatin methacryloyl (GelMA) hydrogels

Reagent	Product	Provider	Notes
Gelatin Methacryloyl (Porcine Skin)	SASKU0010	Swift Analytical	GelMA
Lithium phenyl-2,4,6-trimethylbenzoylphosphinate	900889-1G	Sigma-Aldrich	LAP

Table 2.6: List of reagents used in PDMS Micropillar arrays

Reagent	Product	Provider	Notes
Polydimethylsiloxane			PDMS
Sylgard 184	1024001	Dow Corning	-
Fibronectin	1918-FN-02M	R&D Systems	Human, from plasma

Table 2.7: List of other reagents and materials used

Reagent	Product	Provider	Notes
Anhydrous Dimethyl Sulfoxide	D/4120/PB08	Fisher Scientific	DMSO
Dulbecco's phosphate buffer solution	14040-083	ThermoFisher	DPBS
CellAdhere Type I Bovine Collagen	07001	Stem Cell Technologies	

2.3 Methods

2.3.1 Sample preparation and ethics

Skin biopsy extraction and initial cell culture was carried out in Italy, at either the biobank of the Giannina Gaslini Institute, Genova or the Sant'Orsola - Malpighi Polyclinic, Bologna. Biopsies were extracted from the the dermis and subdermis of the abdominal region of affected individuals. Pateints from which biopsies were obtained are outlined in table 2.1. All biopsies were obtained out during surgery in order to operate under general anesthesia and therefore reduce the impact of the procedure, as outlined by the ethics committee. The location of the biopsy coincided with the incision in the abdomen and consisted of the removal of 1-2 cm^2 of skin in correspondence with the surgical cut, and immediately before the definitive suture. The skin biopsies were minced and cultured as outlined below in section 2.3.2. This allowed the collection of dermal fibroblasts to set up the cell lines.

For work carried out on cell lines obtained from the the Giannina Gaslini Institute, ethical approval was granted by N. CET - Liguria: 269/2021 - DB Id: 11485. Additionally, ethical approval was granted by Sant'Orsola - Malpighi Polyclinic for work carried out on control (C1) and the *PIEZO1* mutant cell lines.

2.3.2 Cell culture

HDFs were cultured in Dulbecco's Modified Eagle Medium (DMEM) or Roswell Park Memorial Institute 1640 Medium (RPMI) media as indicated in table 2.1. Cells were expanded and experiments carried out at low passages.

hTERTs cultured in DMEM (+ 4.5 g/l D-Glucose, + L-Glutamine, + Pyruvate) were supplemented with 1% penicillin/streptomycin, 0.05% fungizone, 1 X non-essential amino acids solution, and 10% Foetal Bovine Serum (FBS).

Primary cells cultured in DMEM (+ 4.5 g/l D-Glucose, + L-Glutamine, + Pyruvate) were supplemented with 1% penicillin/streptomycin and 10% FBS. Cells cultured in Roswell Park Memorial Institute 1640 Medium (RPMI) (+ L-Glutamine) were supplemented with 1% penicillin/streptomycin and 10% FBS. All cells were kept at 37°C in a humidified incubator with 5% CO_2. Culture media was changed every 2 to 3 days. VSCM and non-*ACTG2* CIPO cell lines grew at a slower rate compared to control cells, with control cell lines having a doubling rate of approximately 2 days compared to about 5 days for VSCM cells.

For all experiments, except those assessing migration and traction forces, cells were synchronised in terms of their cell cycle and metabolic activity. This synchronisation was achieved by culturing the cells in media with 1% FBS, instead of the usual 10% FBS, for 24 hours before cell seeding.

2.3.3 Immunofluorescence

HDFs were seeded, at a concentration of 2000 cells/cm^2, onto glass coverslips coated with type 1 bovine collagen. Cells were cultured for 24 hours as outlined in section 2.3.2.

Samples then underwent fixation in 4% paraformaldehyde for 15 minutes at room temperature (RT), followed by washing with DPBS. To permit cellular permeabilisation, 0.1% Triton X-100 was used for 5 minutes. Washing steps with DPBS were performed twice, and samples were blocked with 1% Bovine Serum Albumin (BSA) for 1 hour at RT to prevent non-specific binding. The appropriate primary antibody was added and incubated overnight at 4°C. Following incubation, the samples underwent 3 washes using washing buffer (0.5% Tween 20 in DPBS), each lasting 5 minutes. Phalloidin and secondary antibodies were then incubated for 1 hour at RT. Samples were washed with washing buffer three times, each for 5 minutes. Lastly, VectaShield mounting media with DAPI was added. The antibodies used, and appropriate dilutions can be found in table 2.3.

2.3.4 Statistical analysis

Statistical analysis was performed using GraphPad Prism 8.4.2 software. Unless stated otherwise, all experiments were performed in triplicate and the number of images taken per sample have been outlined in the relevant sections.

First the Gaussian distribution of the data was tested via D'Agostino-Pearson normality test [83]. When only two groups were compared, either parametric unpaired t-test with Welch's correction (for normally distributed data) or non-parametric Mann-Whitney test (non-normally distributed data) were used [84,85].

For analysis involving three or more groups: data that was normally distributed underwent a Brown-Forsythe and Welch ANOVA test, with Dunnett T3 post hoc test for adjustment of multiple comparisons; for data that was not normally distributed, the Kruskal-Wallis test was applied, followed by Dunn's post hoc test for multiple comparison adjustments [86–89].

Significant differences between groups was denoted as follows: * for p-values $<$ 0.05, ** for p-values $<$ 0.01, *** for p-values $<$ 0.005, **** for p-values $<$ 0.001, and non-significant differences ($p > 0.05$) were labelled as (n.s).

3 | Biomarkers Associated to Mechanotransduction

3.1 Introduction

Mechanical forces are exerted during normal intestinal function. These include tensile, compressive, which are exerted during intestinal filling and emptying; and shear forces. [90]. Tensile forces occur when the intestine stretches as digestive content enters and compressive forces arise on contraction of the intestine during emptying [91]. Shear forces occur due to a number of reasons. The first being, movement of intestinal content along the digestive tract known as peristalsis [92]. Additionally, segmental and ring contractions result in shear force due to the churning of intestinal content, which generates a force parallel to the movement of the content [93]. Moreover, shear force can arise in the intestinal lining during luminal flow of chyme, which is partially digested contents in gastric fluid, through the intestine. Luminal flow derived shear stress is impacted by the viscosity and flow speed [90, 92].

Cell behaviour and function are not only impacted by biochemical cues but also by mechanical stimuli. The field of mechanobiology is the study of mechanics and biology in an attempt to understand how cells can sense, modify, and respond to the mechanical stimuli in their environment [94]. These include cues such as changes in shear stress, matrix stiffness, and pressure. Therefore, the impact of intestinal gasses and changes in the luminal cross section affect the mechanical forces experienced by cells. The cumulative effect of these forces impacts intestinal development as well as the ability to maintain organ homeostasis [90, 91]. The ability of cells to ‘sense’ their environment is known as mechanosensing. It involves the use of cellular structures, primarily, integrins, actin cytoskeleton, focal adhesions, and ion channels, to determine how any modification in the surrounding environment [95]. Following mechanosensing the mechanotransduction pathways activate, allowing the translation of the mechanical stimuli into cellular responses [96]. In the context of VSCM, mechanotransduction converts the mechanical stimulus, i.e. mechanical forces outlined above, to biochemical signals that control cell behaviour [97].

One pivotal mechanotransducer is Yes-associated protein (YAP). YAP is a transcriptional regulator that plays a critical role in sensing mechanical stimuli and mediating a biological response, by triggering the downstream hippo signalling cascade [98]. Cellular localisation of YAP can provide an indication of mechanotransduction. A greater ratio of nuclear to cytoplasmic YAP indicates that YAP has been mechanically activated due to higher levels of mechanical stimulus [99]. In this way, YAP can be used as an indicator of cellular response to mechanical forces. Moreover, VSCM is an impairment in intestinal function caused by a pseudo-obstruction in the absence of a physical obstruction [19,63]. This has been attributed to contractile dysfunctions which in turn impact mechanical forces exerted during normal intestinal function. Therefore, this chapter explores the role of mechanotransduction in VSCM.

Initially, YAP localisation was investigated to determine whether differences existed between *ACTG2* associated VSCM and controls. This was followed by the assessment of different platforms to act as an assay through which forces exerted by cells can be measured. The decision to explore a force based assay was twofold: firstly, due to findings from work carried out in collaboration with Viti *et al.,* as a precursors to this project, and secondly, to determine if differences in mechanotransduction were seen in forces exerted by cells. The work carried out in this chapter attempts to understand the role of mechanotransduction in VSCM as well as exploring the use of a mechanotransduction based biomarker for diagnostic and therapeutic purposes.

3.2 Materials and methods

Information on cell lines used and cell culture conditions can be found in Chapter 2, table 2.1 and section 2.3.2. Specifically, for the work carried out in this chapter, the following cell lines were used: control cell lines (C1-C4), *ACTG2*-VSCM cell lines (S1, S2, & M1), *LIG3*-CIPO cell line (LC), HSCR cell lines (H1 & H2), and hTERTs.

3.2.1 YAP image analysis

Immunofluorescence assays for YAP, actin and nuclei was carried out to visualise cellular YAP localisation. The materials and methods used for this work can be found in Chapter 2, section 2.3.3. Images were taken on the Zeiss confocal LSM 980 microscope using 40x oil immersion objective with 1.3 numerical aperture. Quantification of YAP localisation was carried out with ImageJ 2.9.0. The nuclei and actin cytoskeleton were thresholded and outlines used to quantify integrated density of nuclear YAP and cytoplasmic YAP. The nuclear to cytoplasmic YAP ratio was determined using the following equation:

$$YAP_{N/C} = \frac{YAP_N/Area_N}{YAP_C/Area_C} \tag{3.1}$$

where $\mathrm{YAP}_{\mathrm{N/C}}$ is the nuclear to cytoplasmic YAP ratio, $\mathrm{YAP}_{\mathrm{N}}$ is the integrated density of nuclear YAP, $\mathrm{Area}_{\mathrm{N}}$ is the area of the nucleus, $\mathrm{YAP}_{\mathrm{C}}$ is the integrated density of cytoplasmic YAP (equation 3.2), and $\mathrm{Area}_{\mathrm{C}}$ is the area of the cytoplasm (equation 3.3).

Integrated density for cytoplasmic YAP was calculated by:

$$YAP_{\mathrm{C}} = YAP_{\mathrm{Cell}} - YAP_{\mathrm{N}} \tag{3.2}$$

The cytoplasmic area was calculated by:

$$Area_{\mathrm{C}} = Area_{\mathrm{Cell}} - Area_{\mathrm{N}} \tag{3.3}$$

3.2.2 Micropillar array formation

The work on micropillar arrays was carried out in collaboration with Professor Nikolaj Gadegaard's lab in the University of Glasgow.

Micropillar fabrication

Micropillar fabrication methods were based on a published protocol by Ghassemi *et al.,* [100]. This was prepared at the James Watt Nanofabrication Centre, at the University of Glasgow, by Dr Badri Aekbote from Professor Gadegaard's group.

Furthermore, Dr Aekbote prepared polydimethylsiloxane (PDMS) micropillar arrays by mixing PDMS with its curing agent, Sylgard 184 in a 10:1 elastomer base: curing agent ratio. The mixture was degassed and spin coated onto glass slides. A silicon mould with pit structures was placed on top to be cured at 70°C for 12 hours after which the silicon was removed. The resulting PDMS micropillar array had a Young's modulus of 2MPa. The micropillars were arranged in a square lattice with a pillar centre to pillar centre gap (pitch) of 3μm. Each pillar was 2.9 - 3μm in height, 1μm in diameter and had a stiffness of k=12.07 nN/μm using the Euler–Bernoulli beam theory:

$$k = \frac{3}{64}\pi E \frac{D^4}{L^3} \tag{3.4}$$

were E is the Young's modulus, D is diameter and L is the length of the pillar.

Figure 3.1 illustrates the micropillar dimensions. Moreover, the calculated stiffness and equivalent shear modulus of the fabricated PDMS pillars gives an 11.6 kPa equivalent shear modulus [101].

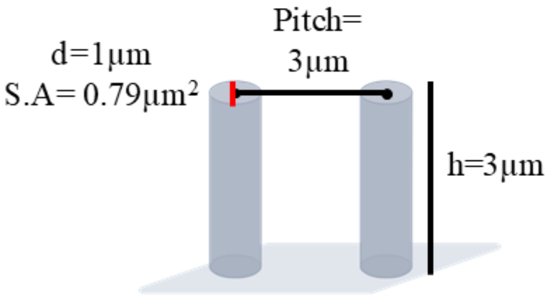

Figure 3.1: Schematic illustrating micropillar dimensions. 3μm Height (h) and 3μm pitch of micropillar are shown. 1μ diameter of pillar (d,red) and 0.79μm surface area (SA) are highlighted. Image created with BioRender.com

Cell seeding

96 well plates containing micropillar arrays were UV sterilised for 10 minutes before seeding. Micropillars were coated with 1μg/ml fibronectin for 1 hour at RT. Cells were seeded at 2000 cells/cm^2 and cultured for 24 hours as outlined in section 2.3.2.

Live imaging

Measurements were acquired using the Evos M7000 imaging system with an on-stage incubator operating at standard cell culture conditions of 37°C and 5% CO$_2$. Single cell images were taken at a rate of 1 image/minute for 20 minutes and captured using 60x air objective with 0.84 numerical aperture.

Micropillar analysis

Time-course stacks of single cells were analysed using ImageJ 2.9.0. Stacks were first aligned using the MultiStackReg plugin followed by using pillar tracker GUI plugin to measure displacement of pillars. The force exerted by single cells on the micropillars was calculated using Hooke's Law:

$$F = kx \tag{3.5}$$

where k is the spring constant (young's modulus) and x is the pillar displacement.

Cellular forces were calculated by measuring deflection of 10 pillars with a total of 21 cells analysed for each cell line.

3.2.3 3D collagen hydrogel formation

Collagen hydrogels with a final concentration of 2.05mg/ml were formed using rat tail collagen type 1, 0.1M NaOH, 10x DMEM, and FBS. The pH was adjusted to 7.2 - 7.4 using additional 0.1M NaOH. The gel solution was then used to resuspend cell pellets. Gelation occurred for 30 minutes in a 37°C humidified incubator with 5% CO_2. The final volume of collagen hydrogels was 200μl in 48 well plates. Cell culture media was added following gelation, and gels were transferred to a 37°C incubator with 5% CO_2.

3.2.4 3D GelMa hydrogel formation

GelMa hydrogels (5% w/v) encapsulated with fibroblast cells were mixed with photoinitiator lithium acylphosphinate (LAP) (0.5% w/v) and photo-polymerised using UV light at an intensity of 7 mW/cm^2 for 5 minutes. The final volume of the hydrogels was 200μl in a 48 well plate. Cell culture media was added following gelation, and hydrogels were transferred to a 37°C incubator with 5% CO_2.

3.2.5 Hydrogel imaging and analysis

Hydrogels were imaged every 24 hours for 4 days (unless otherwise stated) using the LICOR Odyssey Sa Infrared Imaging System. Hydrogel area was measured using ImageJ 2.9.0. The percentage hydrogel area reduction was calculated relative to the negative control gels (gels with no cells).

3.2.6 Rheology

The mechanical properties of hydrogels were characterised using the MCR302 (Anton Paar) rheometer, 24 hours after gelation. Parallel plate geometry was used where the upper plate diameter was 8mm. Measurements were taken on 5 hydrogels per gel type. For all measurements the temperature was set to 37°C and DPBS was used to prevent evaporation.

Strain sweeps were performed to evaluate the linear viscoelastic properties of the hydrogels. Specifically, the strain was varied from 0.1 to 10 % while keeping the angular frequency constant at 10 rad/s to ensure quasi-static conditions (i.e., frequency close to zero). Because of this, the storage modulus (G') can be approximated by the shear elastic modulus (G) [102].

3.3 Results

3.3.1 YAP nuclear localisation increases in VSCM

YAP staining on HDFs seeded on collagen coated glass coverslips was studied to determine if YAP localisation and activity was affected by mechanical forces exerted by cells. Figures 3.2 showed YAP was present in the cytoplasm and nucleus in all HDF cell lines to varying degrees. This was confirmed via quantification, as outlined in Figures 3.3a and b. A significant increase in nuclear YAP localisation was observed between *ACTG2*-VSCM and healthy controls as well as with HSCR. However, no significant difference was seen between *ACTG2*-VSCM and *LIG3*-CIPO. Additionally, Figure 3.3c showed that when *ACTG2* associated VSCM was split into severe (R257C) and mild (R38H) forms, significant difference was still observed.

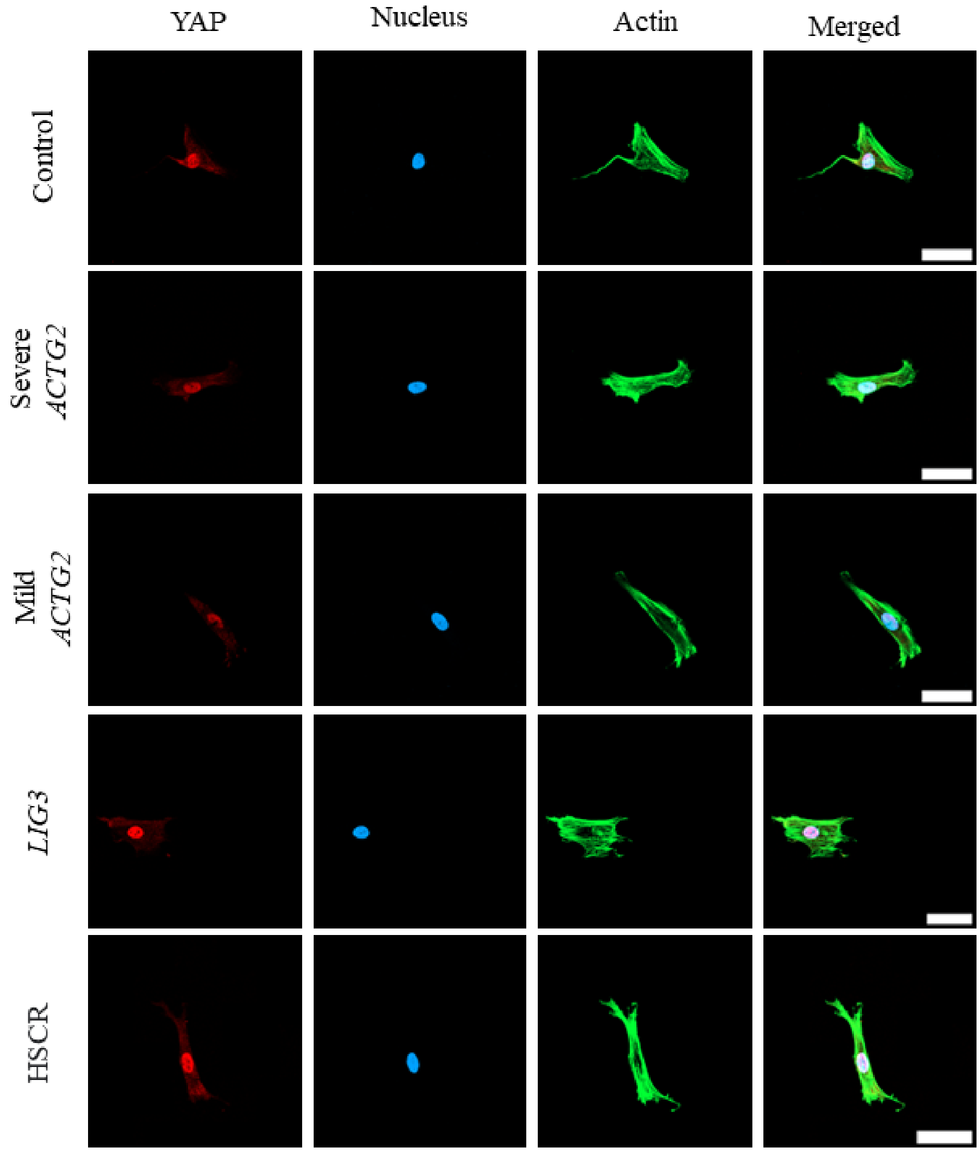

Figure 3.2: Representative single cell images of YAP localisation in HDFs seeded on collagen coated glass coverslips and imaged with Zeiss confocal LSM 980 microscope using 40x oil immersion objective. Blue shows nuclei, green actin and red YAP. Scale bar = 50μm.

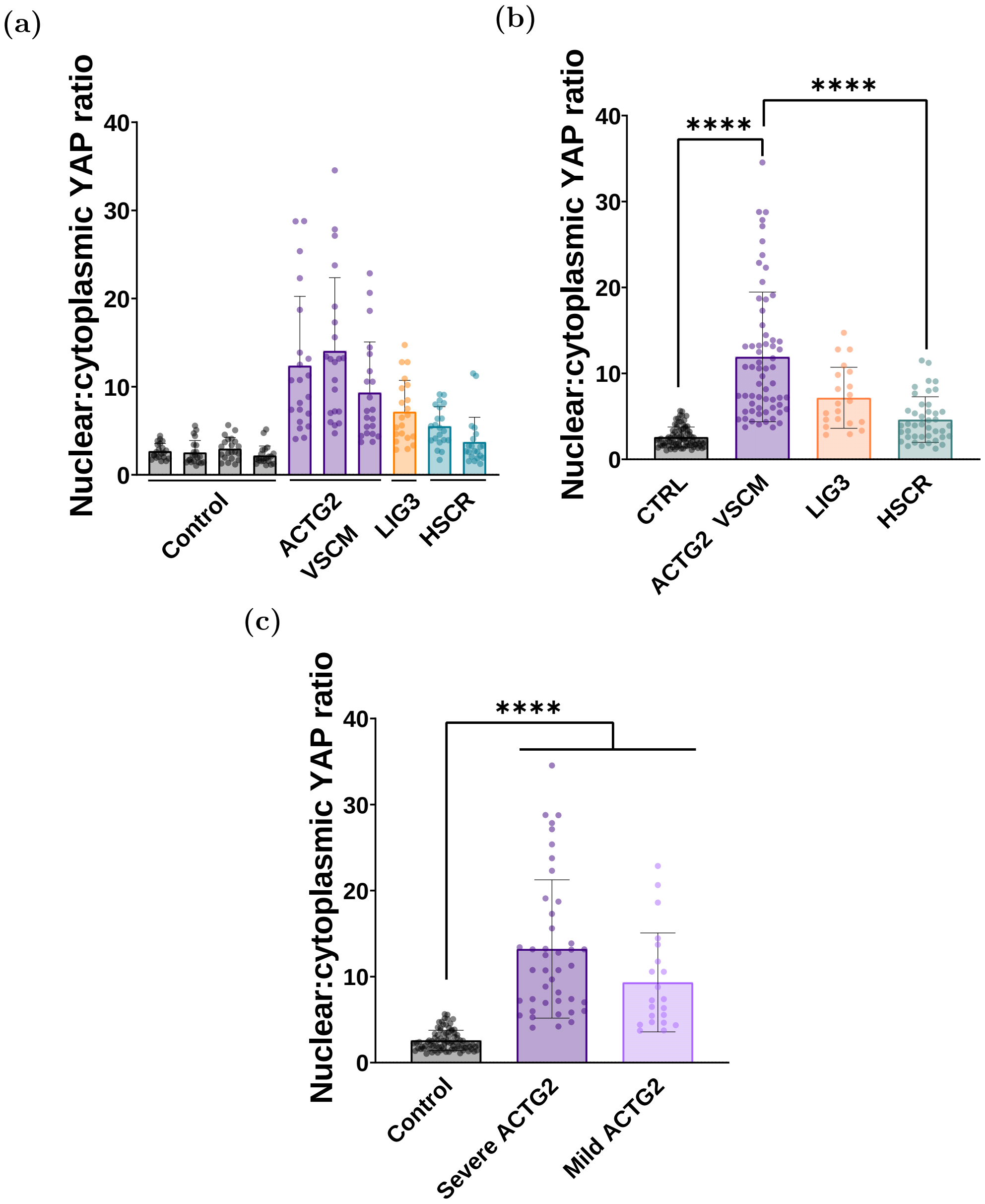

Figure 3.3: YAP localisation in HDF cells. (a) Quantification of nuclear to cytoplasmic YAP ratio in individual cell lines (*n=21 cells*) (b) Quantification of nuclear to cytoplasmic YAP ratio in control cell lines (*n=84 cells*), VSCM affected cell lines (VSCM caused by *ACTG2* variant R257C or R38H) (*n=63 cells*), *LIG3* cell line (*n=21 cells*), and HSCR cell lines (*n=42*) (c) Quantification of nuclear to cytoplasmic YAP ratio in control (*n=84 cells*), severe *ACTG2*-VSCM affected cell lines (R257C, *n-42*), and *ACTG2*-mild VSCM affected cell line (R38H, *n=21*). All graphs show mean ± SD with circles representing individual cell measurements. Statistical significance was determined using Kruskal-Wallis test with Dunn's post hoc multiple comparison test. **** P=0.0008, ****P<0.0001.*

Following on from the quantification of YAP localisation; micropillar array, collagen hydrogel contractility assay and GelMa hydrogel contractility assay were considered as platforms to observe cellular force.

3.3.2 Stiffness of materials

Initially, the stiffness of materials used in this work was characterised through bulk rheology. Five collagen and GelMa hydrogels, made on different days, were measured to determine the G'. The linear viscoelastic region was used to determine G' for collagen, as shown in Figure 3.4a, and for GelMa, shown in Figure 3.4b. From this the average stiffness of the hydrogels were determined. Figure 3.4c showed that the average stiffness of collagen hydrogels was 131Pa and GelMa hydrogels was 390Pa. Greater variation in G' between hydrogels were observed for collagen compared to GelMa based hydrogels. This was expected as the stiffness of collagen hydrogels correlates to the pH at which the gels set. Errors are likely as pH is determined by a visual colour change when adding NaOH as described in section 3.2.3.

Ideally, the PDMS pillar substrate would be characterised experimentally using atomic force microscopy (AFM) or nanoindentation. However, to date, this has not been achievable due the size of micropillars as well as the difficulty in positioning micropillar substrate on their side whilst the cantilever probes the sidewall for measurements. Therefore, the stiffness was calculated theoretically using the Euler-Bernoulli beam theory as outlined under micropillar fabrication in section 3.2.2.

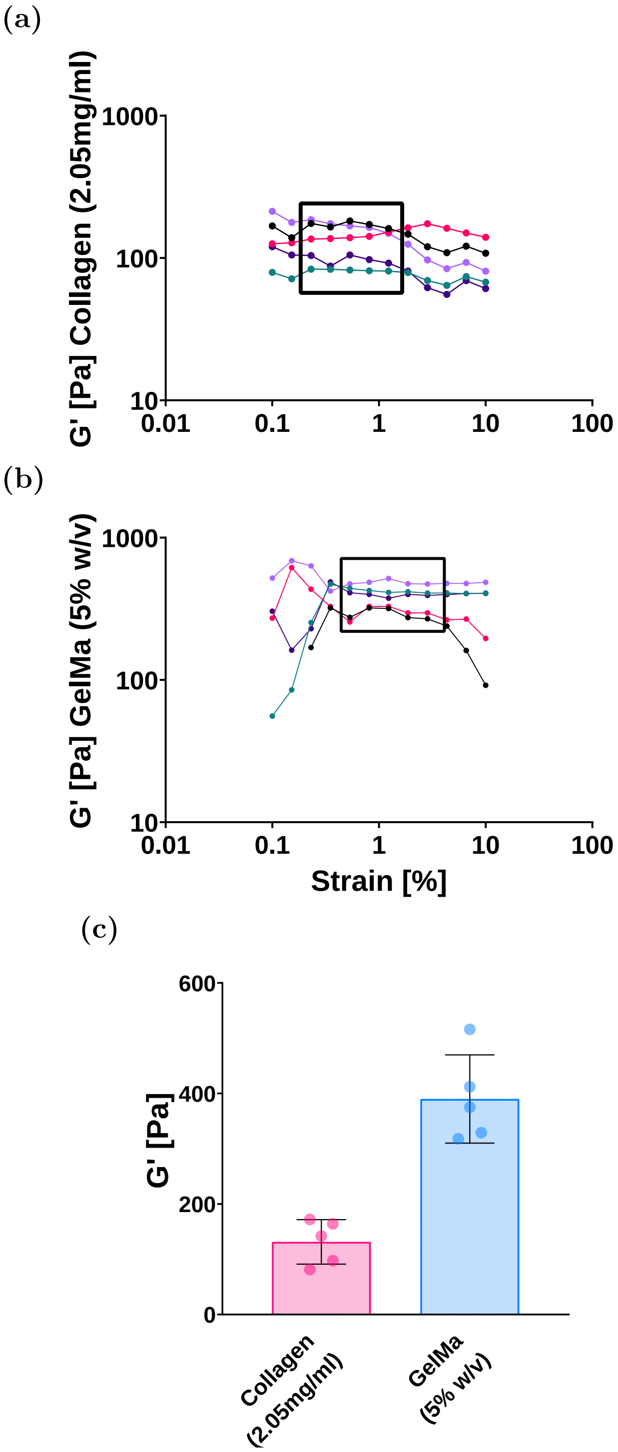

Figure 3.4: Stiffness of collagen and GelMa hydrogels obtained through bulk rheology, 24 hours after gelation. Strain sweep was performed in the linear viscoelastic region using parallel plate geometry to calculate G'. Strain sweep on (a) collagen hydrogels (2.05mg/ml) and (b) GelMa (5% w/v) hydrogels with box outlining linear viscoelastic regime. (c) Hydrogel stiffness for collagen hydrogels ($\varepsilon = 0.543\%$) and GelMa hydrogels ($\varepsilon = 1.23\%$). Graph (c) shows mean ± SD with circles representing individual hydrogel measurements $N = 5$.

3.3.3 VSCM lowers force exerted by cells on micropillar substrate

This work was undertaken in collaboration with Professor Gadegaard's group at the University of Glasgow.

Changes in mechanical forces exerted by HDF cell lines were investigated by seeding cells on top of PDMS micropillar arrays. Figure 3.5a depicts a schematic of a cell seeded ontop of the micropillar array. From Figure 3.5b and c, it was clear that the average force exerted by *ACTG2* associated VSCM was significantly lower than that exerted by healthy control cells. Furthermore, Figure 3.5c highlighted that when *ACTG2*-VSCM was divided into severe and mild forms, the reduction in force exerted by cells was still observed. Additionally, force exerted could be used to differentiate between *ACTG2*-VSCM and HSCR, as highlighted in Figure 3.5b and c. However, no significant difference was seen when *ACTG2* associated VSCM was compared against *LIG3*.

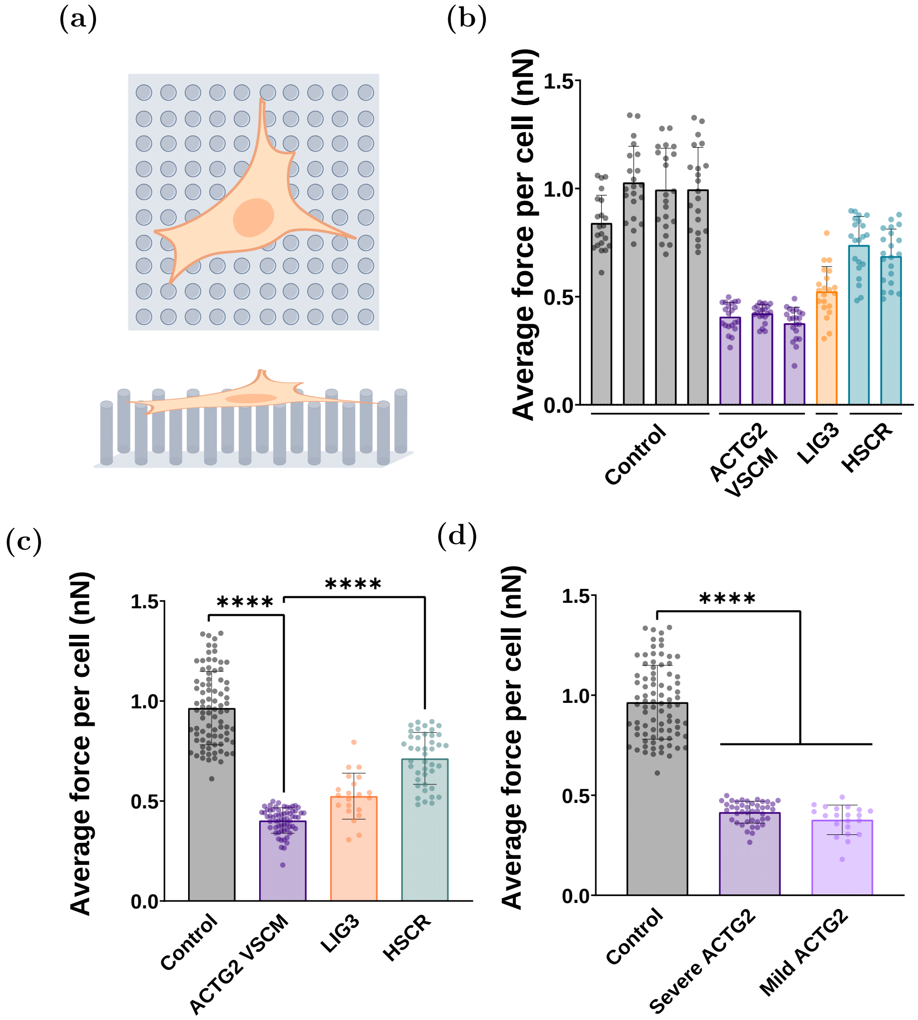

Figure 3.5: Force exerted on PDMS micropillar array. (a) Schematic of single cell on PDMS micropillar array from top and side view. Created with BioRender.com (b) Average force exerted per cell (nN) in individual cell lines (*n=21 cells*). (c) Average force exerted per cell (nN) in control cell lines (*n=84 cells*), VSCM affected cell lines (VSCM caused by *ACTG2* variant R257C or R38H) (*n=63 cells*), *LIG3* cell line (*n=21 cells*), and HSCR cell lines (*n=42*) (c) Average force exerted per cell (nN) in control (*n=84 cells*), severe *ACTG2*-VSCM affected cell lines (R257C, *n-42*), and *ACTG2*-mild VSCM affected cell line (R38H, *n=21*). All graphs show mean ± SD with circles representing individual cell measurements. Statistical significance was determined using Kruskal-Wallis test with Dunn's post hoc multiple comparison test. Statistical significance was determined using Kruskal-Wallis test with Dunn's post hoc multiple comparison test. **** P=0.0002, ****P<0.0001*

3.3.4 Establishing experimental conditions for 3D hydrogel contraction

The ability of cells to contract when encapsulated inside a 3 dimensional (3D) environment was first investigated using collagen hydrogels. The collagen gel contractility assay was an in-house developed method to distinguish between cell phenotypes. Since, the assay had not been used to study fibroblasts, cell seeding density for hydrogel contraction needed to be determined. This was done by seeding different concentrations of hTERTs (50,000 cells/ml, 100,000 cells/ml, 250,000 cells/ml, and 500,000 cells/ml) into hydrogels, and observing hydrogel contraction every 24 hours over 7 days.

Figure 3.6a showed that by day 7, technical replicates of hydrogels with 250,000 cells/ml contracted to a similar degree. This was in contrast to all other cell concentrations tested. Furthermore, Figure 3.6b illustrated that the rate of hydrogel contraction decreases over time, with contraction tapering off after day 4. Therefore, going forward hydrogel contraction assay was monitored for 4 days.

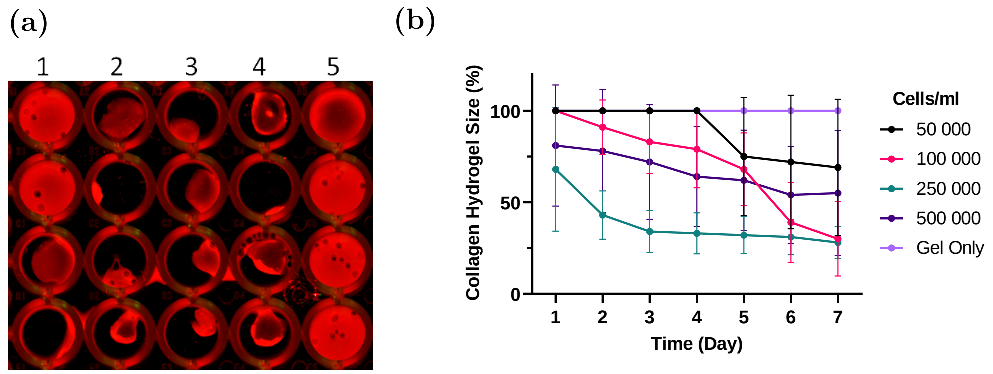

Figure 3.6: Determining cell density for dermal fibroblasts encapsulated in 3D collagen hydrogel. (a) Representative image of collagen hydrogels on day 7. *1 = 50,000 cells/ml; 2 = 100,000 cells/ml; 3 = 250,000 cells/ml; 4 = 500,000 cells/ml; 5 = hydrogel only (no cell).* (b) Change in hydrogel size over 7 days. Graph shows mean ± SD. Cell line = hTERTs, experimental $n = 1$.

3.3.5 Collagen hydrogel contraction assay

Once experimental conditions for using collagen hydrogels as a platform to test dermal fibroblasts, were established, preliminary experiments were carried out on primary HDF cells; *ACTG2*-VSCM and healthy control cells.

Overall, VSCM affected cells caused the collagen hydrogels to contract more than control cell, as illustrated in Figure 3.7 a. Figures 3.7b and c showed control and *ACTG2*-VSCM groups both reduced in size on day 1. However, from Figures

3.7b and d, it can be seen that the difference in size reduction between the two groups decreased over the 4 day period. Furthermore, overall quantification of hydrogel size, on day 4, confirmed VSCM associated gels reduced in size to 19% size compared to 29% for control gels. Although this difference was not significant, the trend of *ACTG2*-VSCM hydrogels contracting more than controls was seen in all experiments regardless of disease severity.

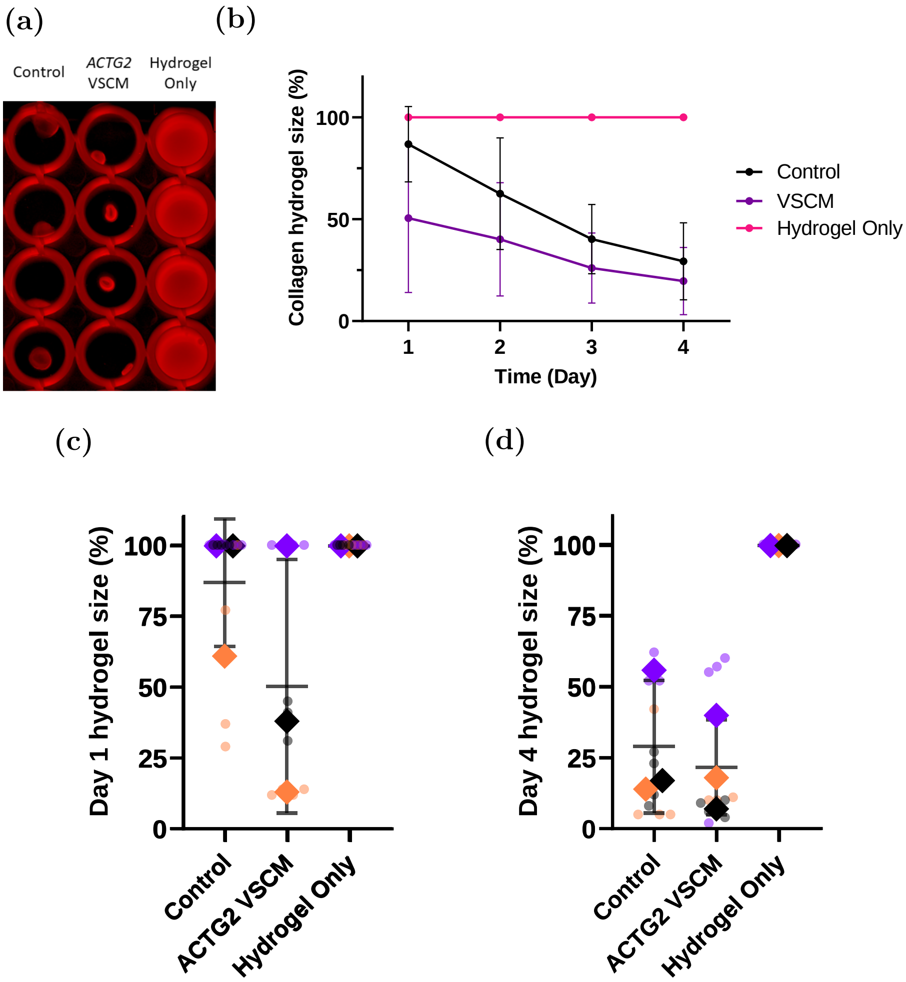

Figure 3.7: *ACTG2*-VSCM and healthy control cell lines encapsulated in 3D collagen hydrogel contraction assay. (a) Representative image of collagen hydrogels day 4. (b) Change in hydrogel size over 4 days. Graph shows mean ± SD. (c) Hydrogel size on day 1. (d) Hydrogel size on day 4. Graph (c) and (d) mean ± SD showing 3 biological replicates represented by different colours. Black and orange are severe VSCM affected cell lines and purple is mild VSCM affected cell line. Circles represent technical repeats and diamonds represent biological repeat *N = 3 biological replicate (with 4 technical repeats per replicate).*

3.3.6 GelMa based hydrogels as a platform to study cell mechanics

Following on from the preliminary findings with collagen, another material was considered for the contraction assay, with the aim of improving outcomes observed with the collagen assay. GelMa was considered as an appropriate material to study mechanical forces exerted by cells as it is a biocompatible material with tunable properties. For the work on the GelMa hydrogel contraction assay, hTERTs were again utilised.

The initial aim was to create GelMa based hydrogels which matched the stiffness of collagen hydrogels. To do this, the tunability of GelMa was exploited. 2.5% w/v GelMa hydrogels were first tested. However, the hydrogels dissolved when cell culture media was added which resulted in no data obtained. 5% w/v GelMa hydrogels were then created. These hydrogels did not dissolve in culture media but were 259Pa stiffer than the collagen hydrogels, as previously outlined in section 3.3.2, Figure 3.4. However, Figures 3.8b, c and d showed that despite the structural stability of the 5% w/v GelMa hydrogels, no cell mediated hydrogel contraction was observed over the 4 day period. This was attributed to the photocrosslinking component of GelMa which was not previously considered.

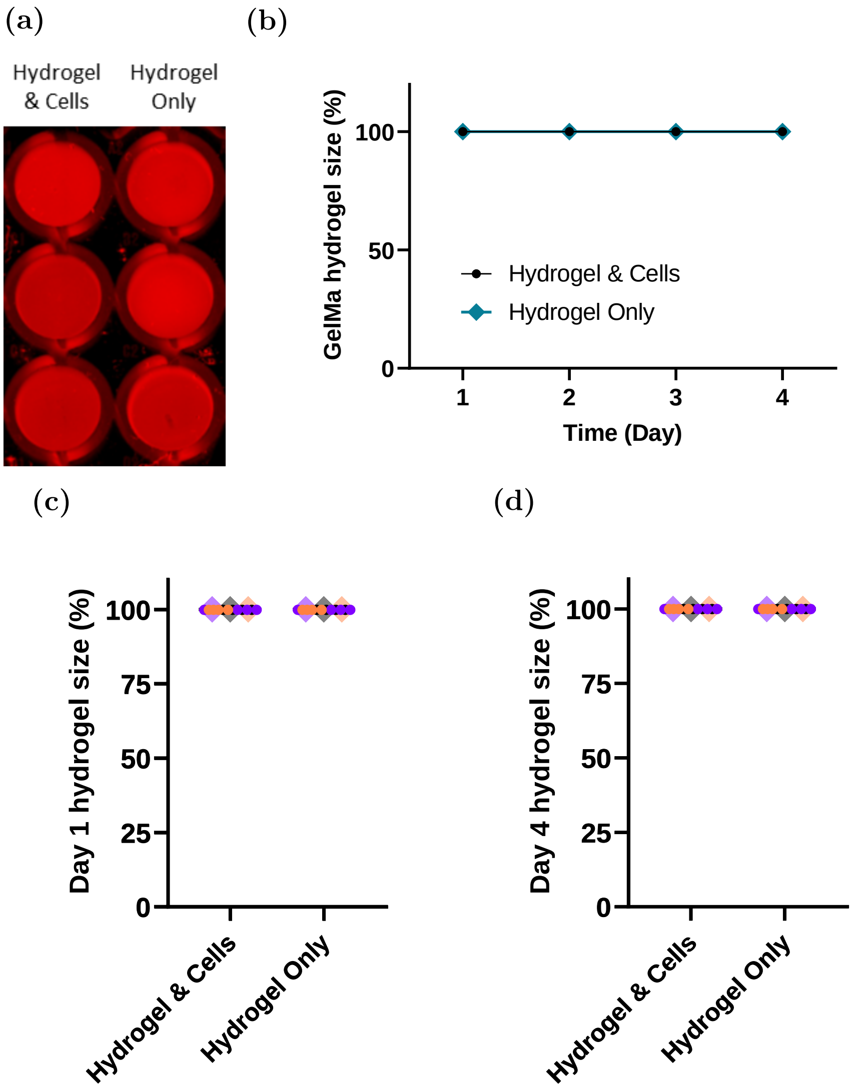

Figure 3.8: Dermal fibroblasts encapsulated in 3D GelMa hydrogel contraction assay. (a) Representative image of GelMa hydrogel day 4 (b) Change in hydrogel size over 4 days. Graph shows mean ± SD (c) Hydrogel size on day 1 (d) Hydrogel size on day 4. Graphs (c) and (d) show mean ± SD, with circles representing technical repeats and diamonds representing biological repeats *Cell line = hTERTs, n = 3 biological replicates (with 4 technical repeats per replicate)*. Cell line = hTERTs, $n = 3$.

3.4 Discussion

A healthy intestine experiences a number of mechanical forces which play an important role in its normal function [90–93]. VSCM is an intestinal disease that affects contractility and thus may have an impact on the mechanical forces exerted. Additionally, cells can detect environmental cues, such as forces, and respond by influencing mechanotransduction pathways [94]. This chapter initially investigated the impact of mechanotransduction in VSCM by analysing YAP localisation. Furthermore, cellular forces were also studied to determine whether there were differences in mechanical forces experienced by VSCM cells in comparison to control cell lines. The overall aim of this chapter was to determine if mechanotransduction associated markers could be utilised as a disease biomarker for *ACTG2*-VSCM with the longer term aim of using such a biomarker for therapeutic and diagnostic purposes.

3.4.1 YAP as a biomarker for VSCM

Initially, YAP was explored as a mechanotransducer in VSCM through YAP staining of HDF cells. Figure 3.3 showed significantly higher nuclear to cytoplasmic YAP ratio in VSCM caused by *ACTG2* mutations. This was independent of disease severity and also higher HSCR but not *LIG3*-CIPO. YAP/TAZ are key modulators of mechanotransduction [99]. Nuclear YAP localisation increases when cells experience greater mechanical forces. Using 2 dimensional (2D) substrates with different stiffness, Dupont and colleagues demonstrated that increased nuclear YAP localisation correlates with increased extra-cellular matrix stiffness [103]. Further work by the same group showed the relationship between stiffness and yap localisation exists in a 3D matrix [104]. However, work by the Chaudhuri group shows stiffness alone does not drive nuclear YAP localisation in 3D models [105]. Although working with 3D culture is closer to a biological model, there can be a number of reasons for the lack of correlation between YAP and stiffness observed by Chaudhuri's group. In a 3D culture environment, factors such as ligand density, cell spreading, and dimensionality play a role in YAP nuclear localisation [106–108]. It is also more difficult to quantify YAP in a 3D model as cells may not lie in the same plane.

Additionally, from the increased YAP nuclear localisation seen in *ACTG2*-VSCM, outlined in Figures 3.2 and 3.3, it is likely the primary HDF cell lines have been mechanically primed [109]. It has been shown that YAP/TAZ retain mechanical memory from their previous environment [110, 111].

Since opposing views on the relationship between YAP and stiffness are held in the mechanobiology field, it is best to consider the results presented in this work in relation to VSCM. Specifically, there is a strong implication that decreased intestinal contractility will impact mechanical forces acting on the intestines which in turn results in stiffening of the intestinal wall [90–93]. Thus, when taking the YAP findings presented in this work together with the current knowledge of mechanical forces acting in the intestine, it can be concluded that the relationship between YAP and stiffness for VSCM aligns with what had been established by Dupont's group. Furthermore, these results highlight the potential of using YAP as a biomarker for VSCM as significant differences are observed between *ACTG2*-VSCM and healthy controls. However, further work would need to be carried out in order to develop a YAP nuclear translocation assay which can be particularly useful for drug screening.

Furthermore, Heuckeroth's group have presented a hypothesis where they proposed YAP localisation to the nucleus occurs in VSCM cells as a result of increasing stiffness. They go on to suggest nuclear YAP localisation creates a feedback loop by binding with myocardin which in turn prevents myocardin binding with serum response factor and causes further downregulation of smooth muscle cell contractile gene expression [63]. The YAP results presented in this thesis, which illustrated higher YAP nuclear localisation in *ACTG2*-VSCM compared to healthy controls, partly supports Heuckeroth's hypothesis. Nonetheless, the work carried out in this thesis, did not delve into the role of myocardin in relation to VSCM. However, literature has shown a relationship between contractility, YAP/TAZ and myocardin [110]. In particular, Daoud and colleagues found the knockout of YAP/TAZ in mice resulted in a reduced contractile phenotype with CIPO-like symptoms of intestinal distention and fecoloma [112]. Although this study investigated the downregulation of YAP/TAZ, it highlighted the importance of YAP in intestinal pseudo-obstructions and shows further work investigating YAP will be beneficial in improving our understanding of VSCM. Overall, there is scope for future work on investigating YAP localisation in relation to VSCM as well as the potential use of YAP as a biomarker for a VSCM drug screening assay. This will be discussed in greater detail in Chapter 6.

3.4.2 Micropillar arrays as a platform for VSCM screening

Differences in the mechanical forces exerted by control and *ACTG2*-VSCM cells were measured to explore whether cellular forces could also be a label-free biomarker for VSCM. PDMS, collagen, and GelMa were utilised as platforms to study this. The choice of substrate was based on biocompatiblity, material tunability, and substrates that are widely used in the bioengineering field [113–117].

PDMS micropillar arrays were used to investigate traction forces exerted by HDF cell lines. Reduced forces were exerted by *ACTG2* associated VSCM cells compared to control groups. This was also seen in work carried out by Viti and colleagues using confocal reference free traction force microscopy [82]. The same patient cell lines used in this thesis were also utilised in Viti's work as it was carried out as a precursor to this project, and in collaboration. The traction force work by Viti was carried out independently, however, also highlighted that *ACTG2*-VSCM cells exert significantly less traction forces compared to healthy controls and HSCR cell lines. However, the technique used by Viti and colleagues, although robust was highly specialised and not easily reproducible in clinical and research settings, thus limiting its use in diagnostics and therapeutics.

Overall, PDMS micropillar arrays can be considered a good platform to study traction forces as they are highly reproducible and there is little batch to batch variation. The work carried out in this thesis was in collaboration with Professor Gadegaard's group who specialise in micropillar substrate. However, it can be difficult to manufacture the micropillar arrays in a clinical setting.

3.4.3 Hydrogel contraction assays

Hydrogel contraction assays using soft materials (collagen and GelMa) were employed to test if differences in contractility of control versus VSCM cells could be quantified using a 3D model. It was initially decided that the assay will be based on collagen, as collagen is the most widely used material to measure cell mediated effects of forces [118]. The preliminary results shown in Figure 3.7 indicated a trend where collagen based hydrogels could be used to distinguish between control and *ACTG2*-VSCM cells. Collagen hydrogel contraction assays have also been utilised by a number of groups to study cell contraction in VSCM caused by different *ACTG2* mutations. A reduction in gel contractility was reported in VSCM caused by *ACTG2* variants R148S, R178L, and R178C. No significant differences were observed in VSCM caused by variants R40C, R63Q, and R257C [8,18,49,59]. Due to the discrepancies highlighted here, further work is needed in order to quantify the effects of forces in VSCM. This can be carried out using different materials and platforms other than collagen.

Furthermore, Figure 3.5 and 3.7 showed that the collagen hydrogel contraction assay results differed from the traction force results. A decrease in traction forces were observed in *ACTG2*-VSCM cells using micropillar arrays; compared to greater contraction caused by *ACTG2*-VSCM cells encapsulated in collagen hydrogels. This difference can be due to the effects of cell-matrix interactions, where cells are able to remodel the hydrogel resulting in greater contractions [119]. Additionally, a 3D context is a closer representation of *in vivo*. However, studying traction forces on 2D substrates offers a more controlled environment with fewer variables at play. It should also be noted that the contraction assay only showed a trend and further optimisation is required, perhaps with a different material for the hydrogel.

The development of the collagen contraction assay was stopped in order to maximise the investigation of an ideal label-free biomarker. This was due to the large variation observed between hydrogels which is an inherent property of collagen. Large variation made it difficult to define clear boundaries between healthy control and *ACTG2*-VSCM cell lines. Moreover, although cells were able to contract the collagen hydrogels, the cell density required for hydrogel gel contraction was not feasible in carrying out optimisation work where large numbers of primary cells are needed but not readily available. Reducing the final volume of the hydrogel (currently 200μl) could be a solution to the cell density issue. However, contraction would become harder to quantify.

In this chapter, a GelMa based hydrogel contraction assay was also explored. Figure 3.8 showed that no hydrogel contraction was observed during the four day period. This was most likely due to the photocrosslinking component of GelMa hydrogel formation as well as greater network density that occurs with GelMa based hydrogels [120, 121]. Cell viability in the hydrogels was not investigated as further testing on GelMa would be redundant as the material could not contract, so would not be utilised for the purposes of this project.

The main conclusions from the work carried out in this chapter have been illustrated in Figure 3.9.

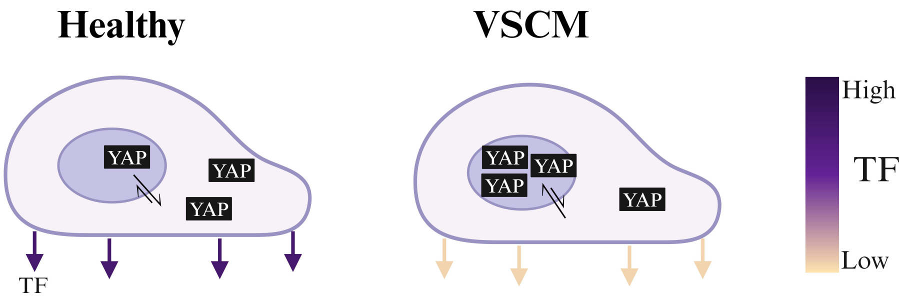

Figure 3.9: Schematic illustrating effects of mechanotransduction in *ACTG2* associated VSCM cells compared to healthy cells. Arrows show traction forces (TF) with the colour of the arrows correlating to force exerted by cells as illustrated with the TF gradient key. Yes-associated protein (YAP) is shown as black squares with double arrows indicating translocation of YAP. VSCM cells exert less force and have a higher nuclear to cytoplasmic YAP ratio compared to healthy cells. Image created with BioRender.com

3.5 Conclusion

At the time of this work, there were no established biomarkers available for VSCM. Traction forces were previously shown to be reduced in VSCM caused by *ACTG2* mutations [82]. Furthermore, it was known that mechanical forces play a key role in normal intestinal activity [90–93].

In this chapter, significant differences in YAP localisation were seen which need to be studied further in order to gain a better understanding of VSCM. This can be carried out, for example, by exploring the hippo signalling pathway, which would aid in the development a drug testing assay which would in turn increase available therapeutic options.

Further developmental work is needed to improve the hydrogel contractility assay. *ACTG2*-VSCM affected cell lines exerted less force on micropillar substrate. Thus, PDMS micropillar arrays present as a useful platform due to the reproducible of the substrate and quantifiable nature of the assay. Currently, micropillar arrays require state of the art fabrication facilities which would be difficult in a clinical and/or drug discovery setting but there is a need for the development of such an assay, for high throughput screening in a commercial setting.

Overall, there is potential for mechanotransduction to be exploited as a disease biomarker for VSCM. The field is moving towards gaining a deeper understanding of the role that cellular forces play in VSCM and in turn using this information for diagnostic and drug discovery purposes.

4 | Migration Based Biomarker

4.1 Introduction

In the previous chapter, the use of force as a label-free physical biomarker for VSCM was explored. During this work, YAP nuclear localisation was significantly increased in VSCM associated cell lines compared to control cell lines. Studies have shown that YAP is also associated with cell migration. Work carried out by Mason and colleagues on endothelial colony-forming cells found that the reduction of YAP/TAZ resulted in reduced migration [122]. The effects of YAP on migration was also seen in prostate cancer cells, where Wenzel's group found mechanical stress stimulated YAP, which in turn increased cancer cell migration [123].

Cell migration is coordinated by various intracellular mechanisms such as actin cytoskeleton dynamics, cell polarity, and adhesions between cells and the extracellular matrix (ECM) [124]. Biophysical cues from the cellular microenvironment begin a signalling cascade that first impacts the actin cytoskeleton [125]. This results in protrusions of the cell membrane which are generated by three processes. Two of these processes are dependent on active actin polymerisation which causes the formation of actin protrusions at the leading edge of the cell, known as lamellipodia and filopodia. The third process is driven by hydrostatic pressure at the actin cortex that results in spherical protrusions known as blebs [126]. After the formation of protrusions, cells can adhere to the ECM through focal adhesions and integrins. This is followed by contraction of the cytoplasm, which then results in detachment of the cell at the rear end, and the cell extending forward due to the protrusive force generated. [127].

Moreover, the filamentous actin structures continuously undergo remodelling by assembling and dissembling in a constant flow known as actin retrograde flow [128]. Actin retrograde flow occurs at the lamellipodia, moves into the cell and when coupled with myosin motors, the force generated is passed from the actin to the focal adhesions. The transmission of force from actin to focal adhesion occurs via integrins. This relationship between actin retrograde flow, force, and focal adhesions was first termed the molecular clutch model [129]. The model can be summarised in an ‘engaged’ and a ‘disengaged’ form. When the molecular clutch is engaged, actin retrograde flow is reduced as the actin cytoskeleton is bound to the ECM though integrins and integrin binding proteins, primarily talin, which in turn interacts with the focal adhesion protein vinculin to bind with the actin cytoskeleton. This results in stronger focal adhesions and greater traction force generation. During clutch disengagement, actin retrograde flow speed increases as the actin polymerisation increases, focal adhesions become less stable, and force generated is weaker [129, 130]. The molecular clutch model is illustrated in the schematic shown in Figure 4.1

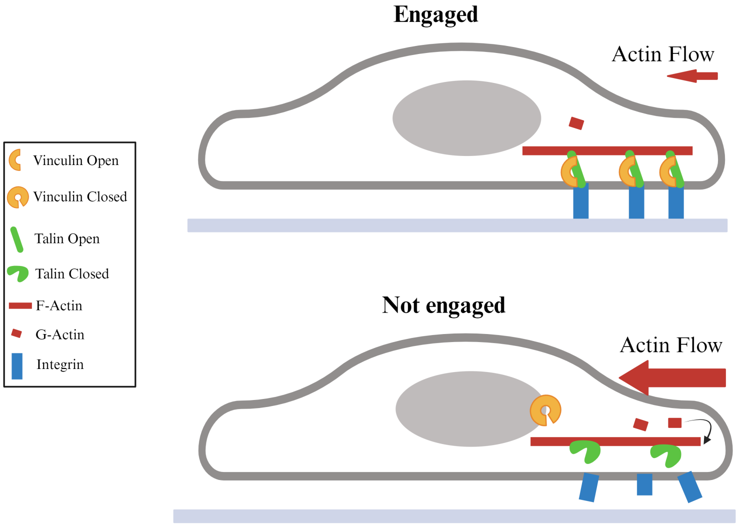

Figure 4.1: Schematic illustrating molecular clutch mechanism. Cell is shown with molecular clutch engaged and not engaged. When the molecular clutch is engaged, talin interacts with vinculin to bind with the actin cytoskeleton which in turn is bound via integrins to the extracellular matrix (ECM). When the clutch is not engaged, these interactions do not occur Image created with BioRender.com

In this chapter, single cell migration was monitored by digital holographic microscopy on HoloMonitorM4 microscope (Phase Holographic Imaging PHI AB, Sweden). Digital holographic microscopy is a label-free method of live cell tracking which is has been utilised to study cell behaviour due to the advantages over traditional cell tracking techniques [131–133]. For example, traditionally, cell tracking can be carried out by staining with dyes, but there is uncertainty surrounding the impact of these dyes on cell behaviour [134]. Furthermore, using a fluorescence microscope over a long period of time can lead to phototoxicity [135]. Thus, in order to minimise impact on cells during tracking over the 24 hour period, digital holography was used to study cell migration.

Overall, since the majority of VSCM cases occur due to mutations in *ACTG2* (an actin isoform), this chapter focuses on understanding cell morphology and mechanical clutch engagement in the context of VSCM. Differences in cell morphology, focal adhesions, and actin retrograde flow were studied. Moreover, digital holography was then employed to monitor cell migration in a label-free manner to explore the use of migration as a biomarker for VSCM that can potentially be used for diagnostic and therapeutic purposes.

4.2 Materials and methods

Information on cell lines used and cell culture conditions can be found in Chapter 2, table 2.1 and section 2.3.2. Specifically, for the work carried out in this chapter, the following cell lines were used: control cell lines (C1-C4), *ACTG2*-VSCM cell lines (S1, S2 & M1), *LIG3*-CIPO cell line (LC), and HSCR cell lines (H1 & H2).

4.2.1 Immunofluorescence imaging

Immunofluorescence was carried out to visualise nuclei, actin cytoskeleton, and focal adhesions as described in Chapter 2, section 2.3.3. Images of actin cytoskeleton, nuclei and focal adhesions were taken on the Zeiss confocal LSM 980 using 40x oil immersion objective with 1.3 numerical aperture.

4.2.2 Image analysis

For confocal imaging cells were seeded as outlined in section 2.3.3. Image analysis was carried out using CellProfiler v4.2.6.

Cell morphology

The nuclear and corresponding actin cytoskeleton images were converted to 8-bit and processed by thresholding to create masks. Figure 4.2 provides an overview of the analysis workflow in CellProfiler V4.2.6. The following measurements were carried out: cell area (μm^2), nuclear area (μm^2), cell eccentricity as calculated in equation 4.1, major axis length, minor axis length, and Haralick texture features of contrast and entropy for the actin cytoskeleton [136]. Measurements were carried out in pixels and the converted to μm.

$$Eccentricity = \frac{distance\ between\ foci\ of\ elipse}{major\ axis\ length} \tag{4.1}$$

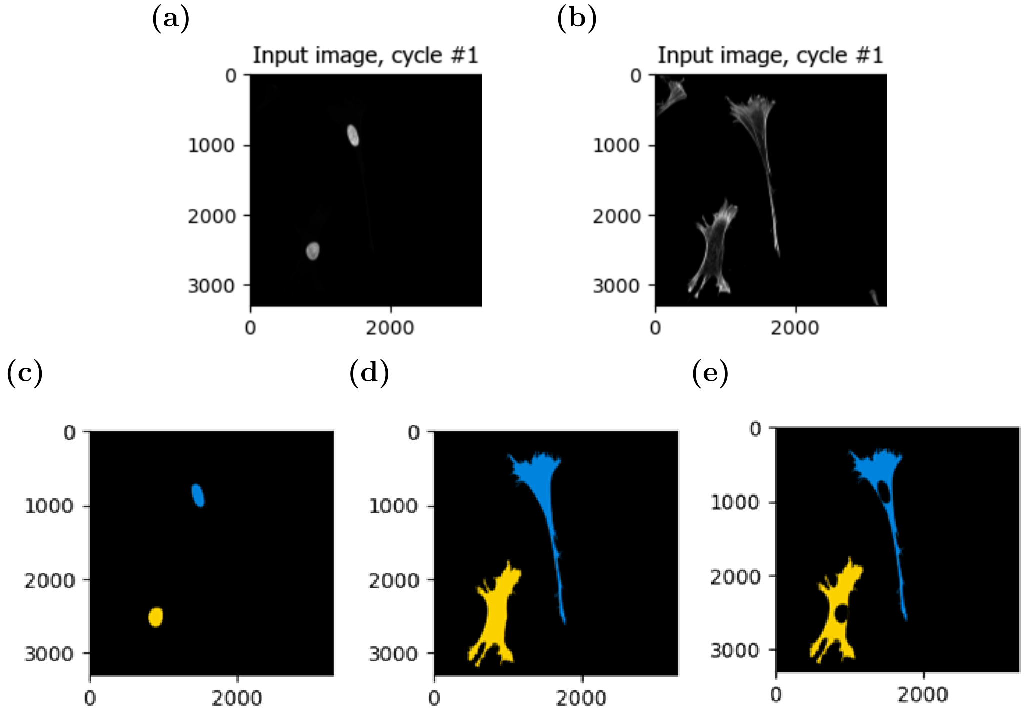

Figure 4.2: Cell morphology analysis workflow using CellProfiler V4.2.6. Cells were seeded, at a concentration of 2000 cells/cm^2, onto glass coverslips coated with type 1 bovine collagen, and cultured for 24 hours prior to fixing and staining. (a) Nuclear input image (b) Actin cytoskeleton input image (c) Nuclear identification (d) Cell identification (e) Cytoplasm identification. Scale shown in pixels.

Focal adhesions

Focal adhesion images were analysed on CellProfiler V4.2.6. Images were processed by creating a mask to outline the cell, illumination correction, and thresholding. This allowed identification of focal adhesion length and number of focal adhesions per cell.

4.2.3 Actin retrograde flow

Cell Seeding

Cells were seeded at a density of 2000 cells/cm^2 on 35 mm glass bottom petri dishes (Matteck, USA) and incubated for 24 hours at 37°C with 5% CO$_2$. SPY555-FastAct was added to samples 2 hours prior to imaging.

Live imaging

Time lapse imaging was carried out on Zeiss confocal LSM 980 microscope using 40x oil immersion objective with 1.3 numerical aperture. During imaging an incubation chamber maintained temperature at 37°C and 5% CO_2. Images were taken every 2 seconds for 4 minutes.

Image analysis

Quantification of actin retrograde flow was carried out using Image J v2.9.0 by converting image stacks to 8-bit and enhancing contrast. Actin retrograde flow was calculated at the leading edge of cells (lamellipodia) using the multi kymograph plugin to produce a kymograph of line width 1 at the selected region. The bounding rectangle was measured on the kymograph followed by division of width by height to obtain speed of actin retrograde flow in pixels/s which was then converted to nm/s. Figure 4.3 shows an example of image stacks with the corresponding kymograph.

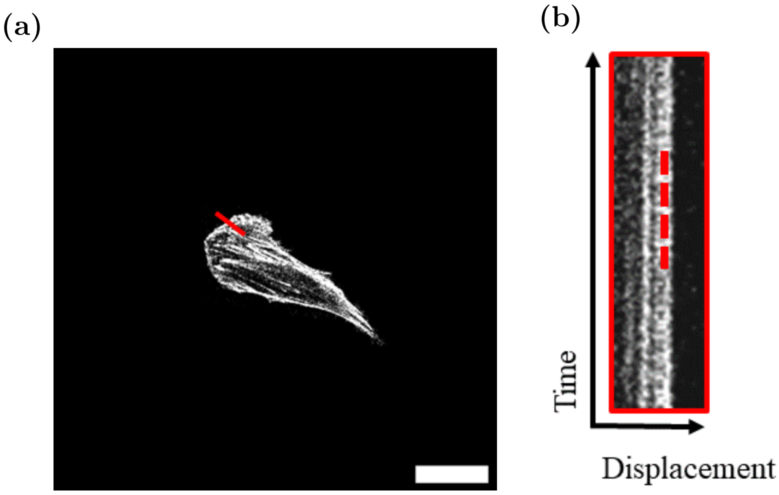

Figure 4.3: Actin retrograde flow quantification example. Cells were seeded, at a concentration of 2000 cells/cm^2, and cultured for 24 hours prior staining with SPY555-FastAct.(a) Representative image stack of example cell stained with SPY555-FastAct. Red line shows region where kymograph is calculated. Scale bar = 50μm. (b) kymograph taken from image stack shown in (a) at highlighted region. Red dashed line indicates slope where actin retrograde flow is calculated.

4.2.4 Digital holography

Digital holographic microscopy works by using a beam splitter to divide the laser beam into two; the sample is illuminated by the object beam whilst the reference beam travels to the reference mirror. An interference pattern (hologram) is created when the object and reference beams intersect, allowing a 3D reconstruction of the cell [137] [138].

Cell seeding

Cells were seeded at a density of 2000 cells/cm^2 on tissue culture treated 24 well plates and cultured for 24 hours as outlined in section 2.3.2.

Live imaging

Excess cell culture media was added to each well as imaging took place in a non-humidified incubator. HoloLids (phiab, Sweden) were UV sterilised for 30 minutes and placed on top of the well plate instead of the usual tissue culture plate lids to improve imaging quality. Measurements were taken inside a 37°C non-humidified incubator with 5% CO$_2$ using the HoloMonitor M4 live cell imaging system. Single cell images were captured every 15 minutes for 24 hours using a 20x air objective.

Image analysis

App suite cell imaging software v4.0 was used to analyse images. 3 technical repeats were carried out where 9 different areas were monitored. This resulted in analysis of more than 50 cells. The average distance travelled by cells in the selected area was calculated using the following equation:

$$d = vt \tag{4.2}$$

where d is distance, v is speed and t is time.

This was then divided by number of cells in the area to get average distance travelled per cell. The average distance travelled was plotted against time. Simple linear regression was carried out from which the gradient of the line was taken as the average speed.

4.3 Results

4.3.1 Evaluating cell shape: area, axes, and eccentricity

Cell morphology was investigated for all HDF cell lines in order to determine phenotypic variations between VSCM and control cell lines. Cells were cultured on collagen coated glass coverslips for 24 hours prior to immunostaining with phalloidin to visualise the cytoskeleton. Representative images for control, severe *ACTG2*-VSCM, mild *ACTG2*-VSCM, *LIG3*-CIPO, and HSCR cell lines are shown in Figure 4.4.

Figure 4.5 shows quantification of cell and nuclear surface area highlighting that there was no significant differences between *ACTG2*-VSCM and healthy control cells, with cell surface area average around 2400 μm^2 and nuclear area around 220 μm^2. However, as demonstrated in Figure 4.5c, *ACTG2* associated VSCM cell lines were spread over a larger area when compared with HSCR cell lines. Moreover, cell eccentricity, major axis length, and minor axis length were measured to determine if variations were present in cell shape. Figure 4.6a-f highlights that *ACTG2* associated VSCM cells had a significantly longer major axis length of 143μm compared to 104μm length for control cells. The minor axis length was similar between *ACTG2* associated VSCM, control and *LIG3*-CIPO cells but shorter for HSCR cells. From Figure 4.6g-i, it was clear that all cell lines had eccentricity values close to 1 implying cells had an elongated elliptical shape. Although, it should be noted that *ACTG2* associated VSCM cells were significantly more elongated compared to controls.

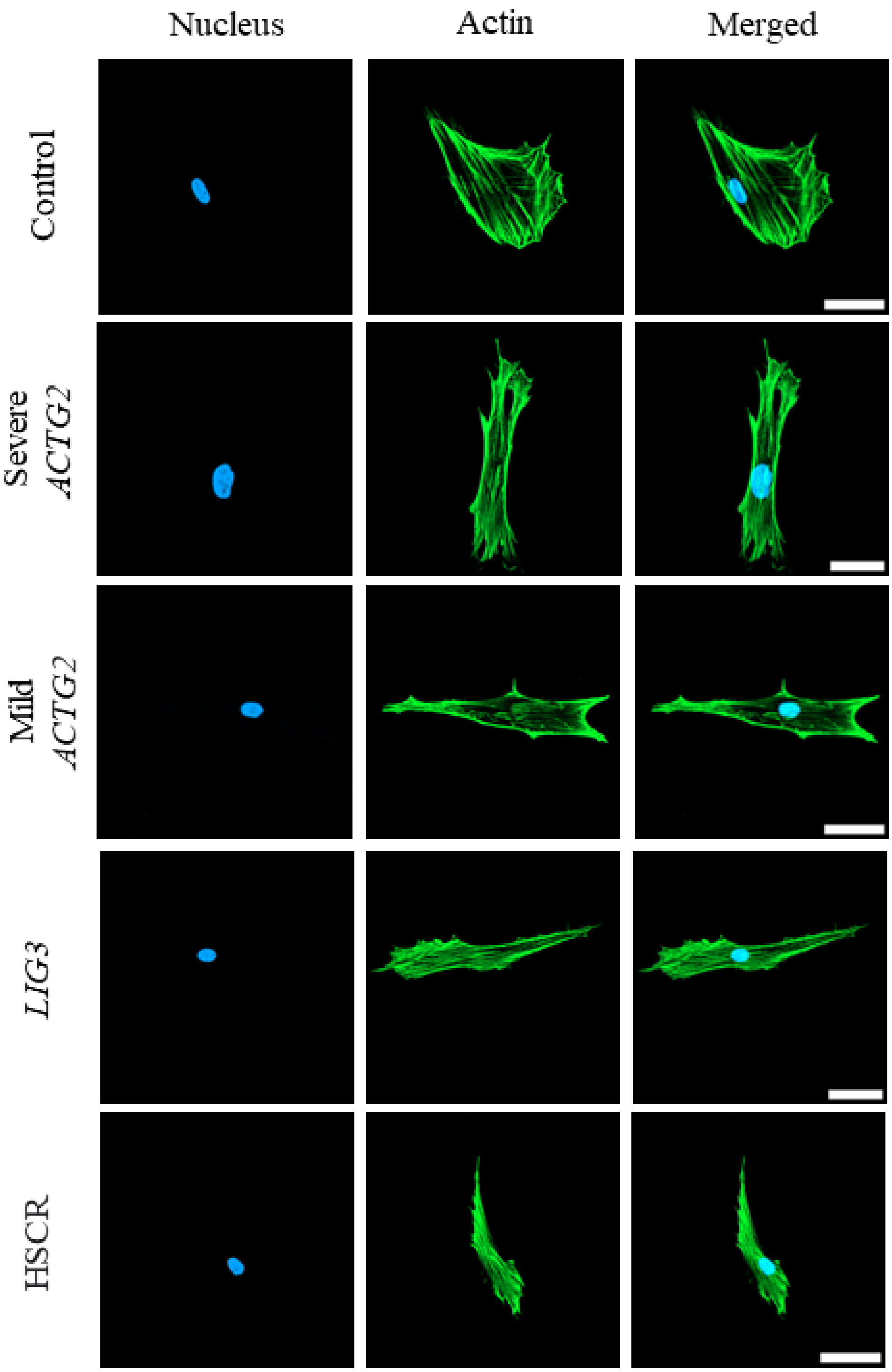

Figure 4.4: Representative images for HDF cells showing nucleus and actin cytoskeleton. Cells were seeded, at a concentration of 2000 cells/cm^2, onto glass coverslips coated with type 1 bovine collagen, and cultured for 24 hours prior to fixing and staining. Imaging was carried out on Zeiss confocal LSM 980 microscope using 40x oil immersion objective. Nucleus (stained with DAPI, blue) and actin cytoskeleton (stained with phalloidin, green). scale bar = 50μm.

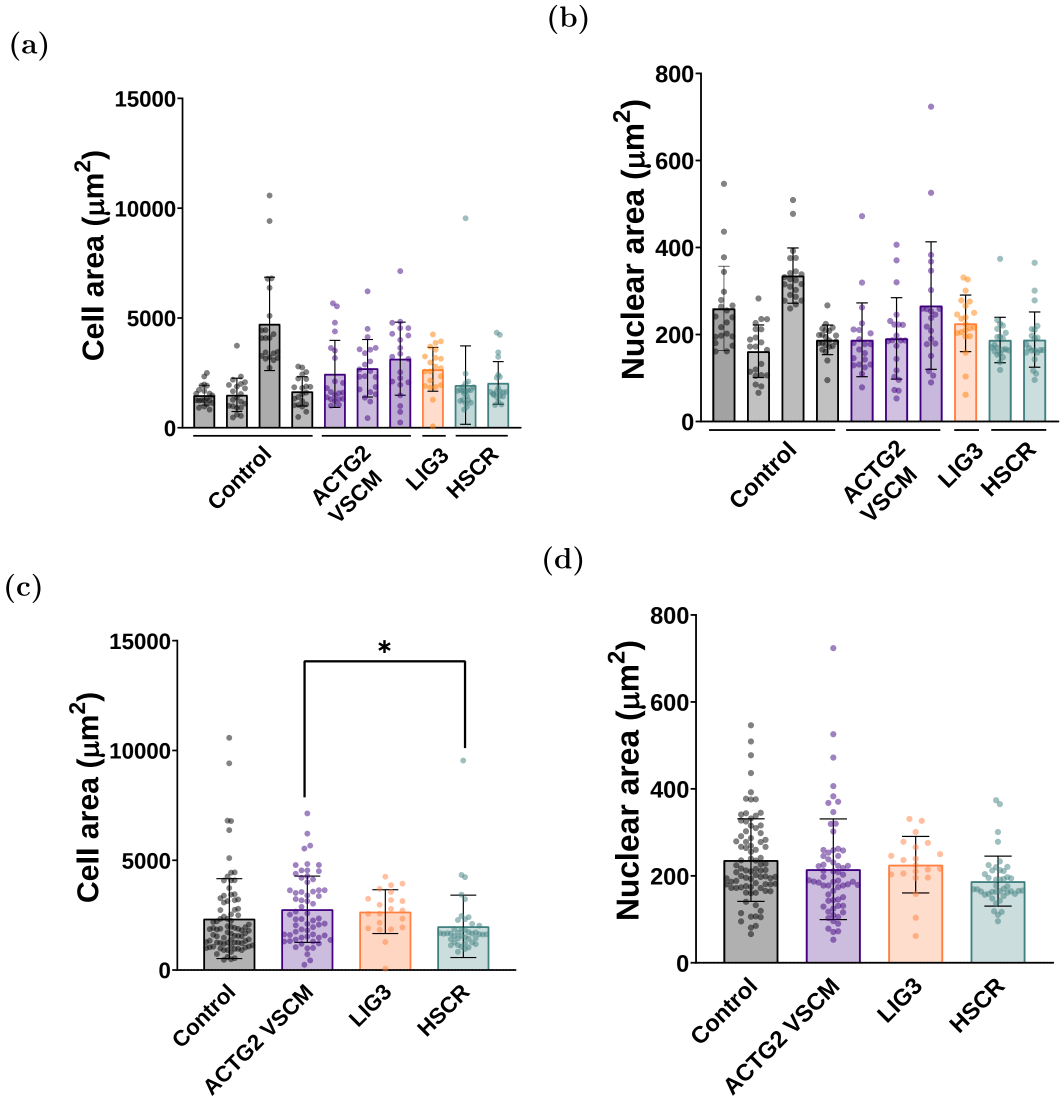

Figure 4.5: VSCM does not impact cell and nuclear area. Quantification of individual cell lines (*n=21 cells*) for (a) Average cell area (μm^2) and (b) Average nuclear area (μm^2). Quantification of control cell lines (*n=84 cells*), VSCM affected cell lines (VSCM caused by *ACTG2* variant R257C or R38H) (*n=63 cells*), *LIG3* cell line (*n=21 cells*), and HSCR cell lines (*n=42*) for (c) Average cell area (μm^2) and (d) Average nuclear area (μm^2). All graphs show mean ± SD with circles representing individual cell measurements. Statistical significance was determined using Kruskal-Wallis test with Dunn's post hoc multiple comparison test. ** P=0.0137*

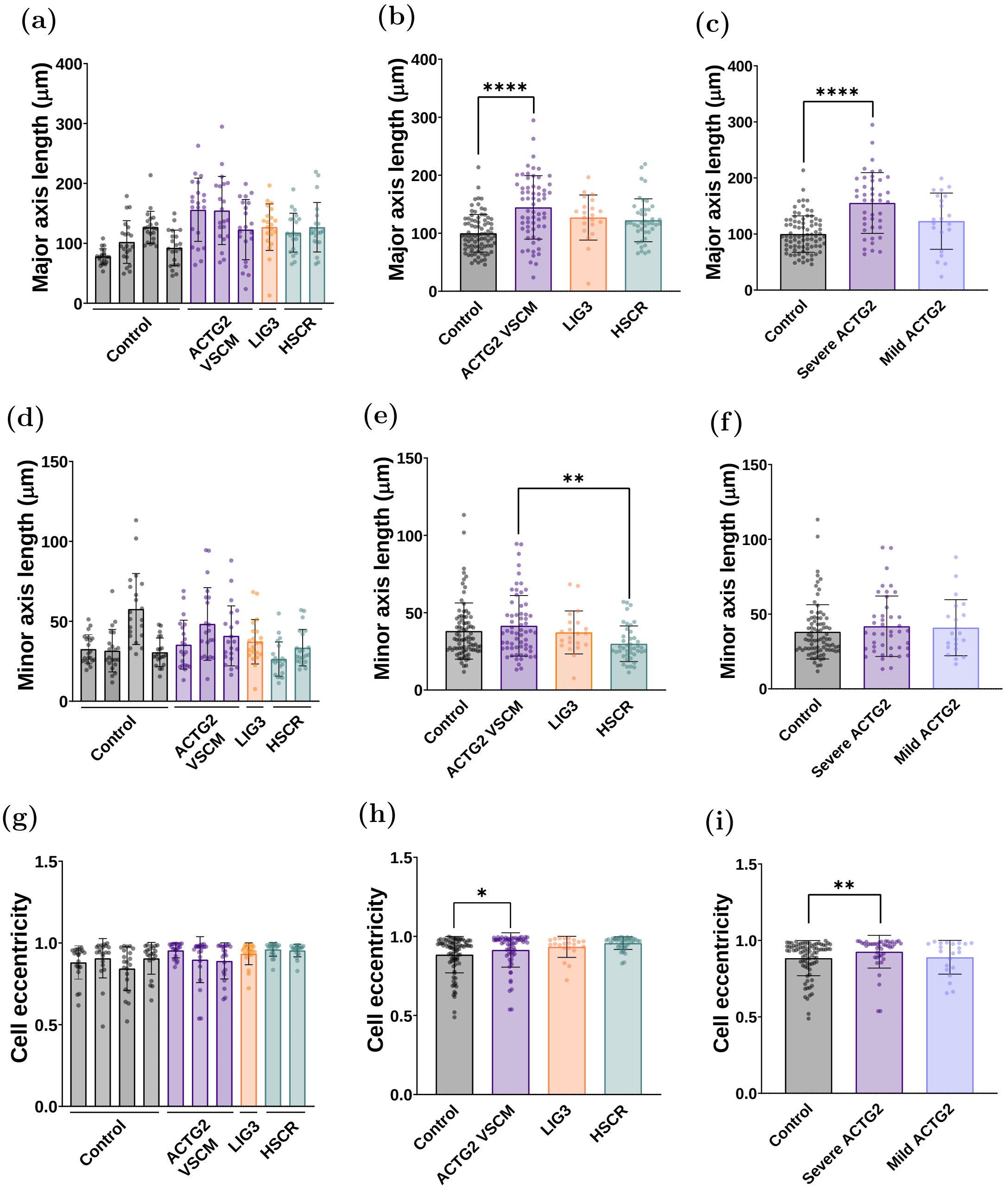

Figure 4.6: Severe *ACTG2*-VSCM associated cells showed more elongation and had a longer major axis length. Quantification of individual cell lines (*n=21 cells*) for (a) major axis length (μm), (d) minor axis length (μm), and (g) cell eccentricity. Quantification of control cell lines (*n=84 cells*), VSCM affected cell lines (VSCM caused by *ACTG2* variants R257C or R38H) (*n=63 cells*), *LIG3* cell line (*n=21 cells*), and HSCR cell lines (*n=42*) for (b) major axis length (μm), (e) minor axis length (μm), and (h) cell eccentricity. Quantification of control (*n=84 cells*), severe *ACTG2*-VSCM affected cell lines (R257C, *n-42*), mild *ACTG2*-VSCM affected cell line (R38H, *n=21*) for (c) major axis length (μm), (f) minor axis length (μm), and (i) cell eccentricity. All graphs show mean ± SD with circles representing individual cell measurements. Statistical significance was determined using Kruskal-Wallis test with Dunn's post hoc multiple comparison test. **P=0.0246 (e); **P= 0.0053 (h); **P=0.0050 (i); ****P<0.0001 (b,c)*

4.3.2 Haralick textural feature analysis on actin cytoskeleton

Haralick textural features of contrast and entropy were measured for the actin cytoskeleton in *ACTG2* associated VSCM, control, *LIG3*, and HSCR cell lines [136]. Haralick contrast measures the variation in the image, whilst Haralick entropy assess the complexity of the image. Values closer to 0 imply that there is less contrast and complexity in the cytoskeleton organisation [136].

Figure 4.7 a, b and d, e showed that *ACTG2* associated VSCM cells had significantly lower average Haralick contrast and Haralick entropy values compared to control and LIG3 cells but similar values to HSCR cells. Furthermore, Figure 4.7 c and f highlighted that when *ACTG2* associated VSCM is divided into severe and mild forms, significantly lower Haralick contrast and entropy values are only observed in cells causing severe VSCM. Additionally, significant differences were seen between severe and mild forms of *ACTG2*-VSCM, where mild *ACTG2* VSCM cells had average Haralick values comparable to control cells.

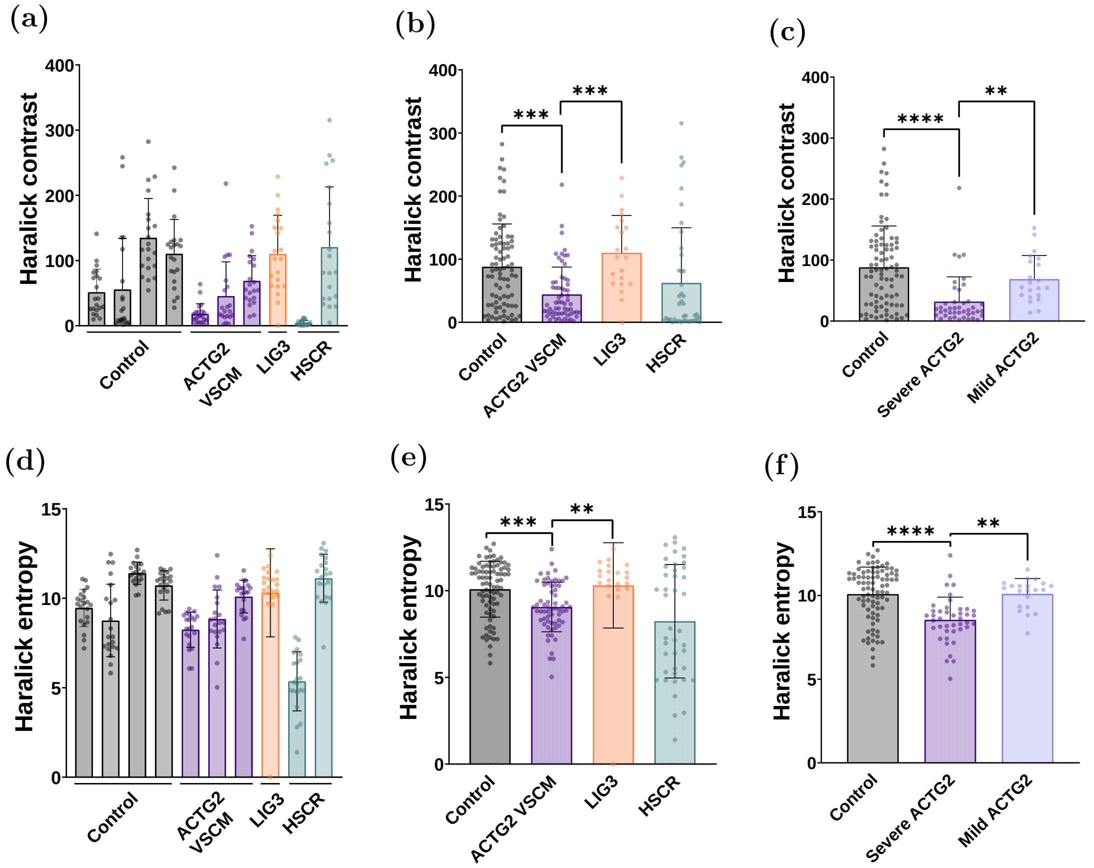

Figure 4.7: Haralick textural feature analysis of actin cytoskeleton in HDFs. Quantification of individual cell lines ($n=21$ *cells*) for (a) Haralick contrast and (d) Haralick entropy. Quantification of control cell lines ($n=84$ *cells*), VSCM affected cell lines (VSCM caused by *ACTG2* variants R257C or R38H) ($n=63$ *cells*), *LIG3* cell line ($n=21$ *cells*), and HSCR cell lines ($n=42$) for (b) Haralick contrast [*** $P=0.0008$ (control-*ACTG2*); $P=0.0004$ (*ACTG2*-*LIG3*)] and (e) Haralick entropy [** $P=0.0018$; *** $P=0.0008$]. Quantification of control ($n=84$ *cells*), severe *ACTG2*-VSCM affected cell lines (R257C, n-42), and mild *ACTG2*-VSCM affected cell line (R38H, $n=21$) for (c) Haralick contrast [** $P=0.0022$; **** $P<0.0001$] and (f) Haralick entropy ** $P=0.0016$; **** $P<0.0001$]. All graphs show mean ± SD with circles representing individual cell measurements. Statistical significance was determined using Kruskal-Wallis test with Dunn's post hoc multiple comparison test.

4.3.3 VSCM influences actin retrograde flow

In order to investigate how the molecular clutch model is impacted in VSCM, the actin retrograde flow was quantified. Cells were incubated with an actin probe (SPY555-FastAct, table 2.3) for two hours prior to live imaging. The average actin retrograde flow speed was calculated at the lamellipodium edge of cells.

Representative images with the associated kymographs are shown for each cell line in Figure 4.8. Figure 4.9 a and b show that *ACTG2* associated VSCM cells had a significantly faster actin retrograde flow speed of 59 nm/sec compared to 28 nm/sec for control cells, 42 nm/sec for LIG3, and 44 nm/sec for HSCR cells. Additionally, in Figure 4.9 c, a significant increase in actin retrograde flow speed was observed when *ACTG2* associated VSCM was split into severe (R257C) and mild (R38H) forms.

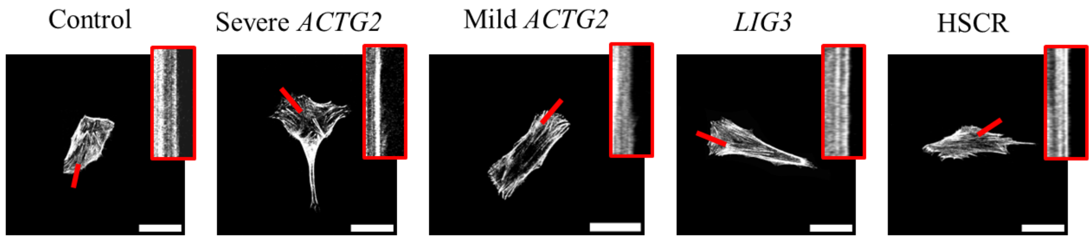

Figure 4.8: Representative single cell image stacks of actin retrograde flow with corresponding kymograph at top left. Cells were incubated with SPY555-FastAct and imaged with Zeiss confocal LSM 980 microscope using 40x oil immersion objective. Scale bar = 50μm.

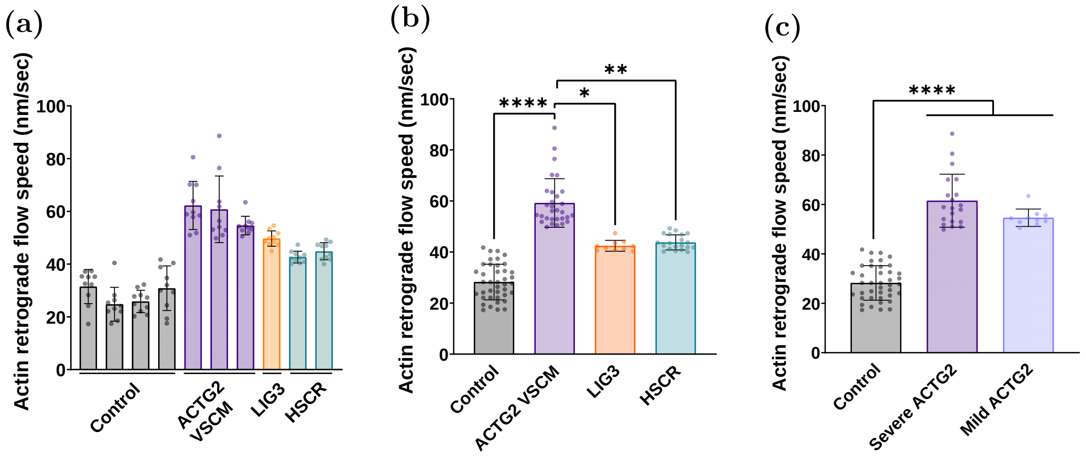

Figure 4.9: Actin retrograde flow speed in HDFs (a) Average actin retrograde flow speed in individual cell lines (b) Average actin retrograde flow speed in control, *ACTG2*-VSCM affected cell lines (VSCM caused by R257C or R38H), *LIG3*, and HSCR cell lines (c) Average actin retrograde flow in control cell lines, severe *ACTG2*-VSCM affected cell lines (R257C) and mild *ACTG2*-VSCM affected cell lines (R38H). 10 cells were analysed for each cell line. Graphs show mean ± SD with circles representing individual cells measurements. Statistical significance was determined using Kruskal-Wallis test with Dunn's post hoc multiple comparison test. _* P=0.0134; ** P=0.0028; **** P<0.0001_

4.3.4 Impact of VSCM on focal adhesion structures

To determine if VSCM influences focal adhesion formation, focal adhesions were visualised through vinculin staining which can be seen in Figure 4.10. The length of individual focal adhesions in a cell as well as the total number of focal adhesions per cell were calculated. Figure 4.11 a and b demonstrate that *ACTG2* associated VSCM cells had significantly shorter focal adhesion length of 3.3 μm compared to 3.8 μm in control cells. Focal adhesion length could also be used to distinguish between *ACTG2*-VSCM cells and *LIG3*-CIPO cells. Moreover, from Figure 4.11 c, it is clear that the difference in focal adhesion length could only be seen in severe VSCM causing *ACTG2* mutations (R257C). Additionally, a significant difference was also observed between the severe and mild *ACTG2*-VSCM forms.

Furthermore, Figure 4.11 d and e indicated that *ACTG2* associated VSCM cells had significantly higher number of focal adhesions compared to control and HSCR cells. Also, Figure 4.11 f highlighted that the increase in number of focal adhesions per cell in VSCM is dependent on disease severity as the difference is only significant in cells with severe forms of *ACTG2* associated VSCM.

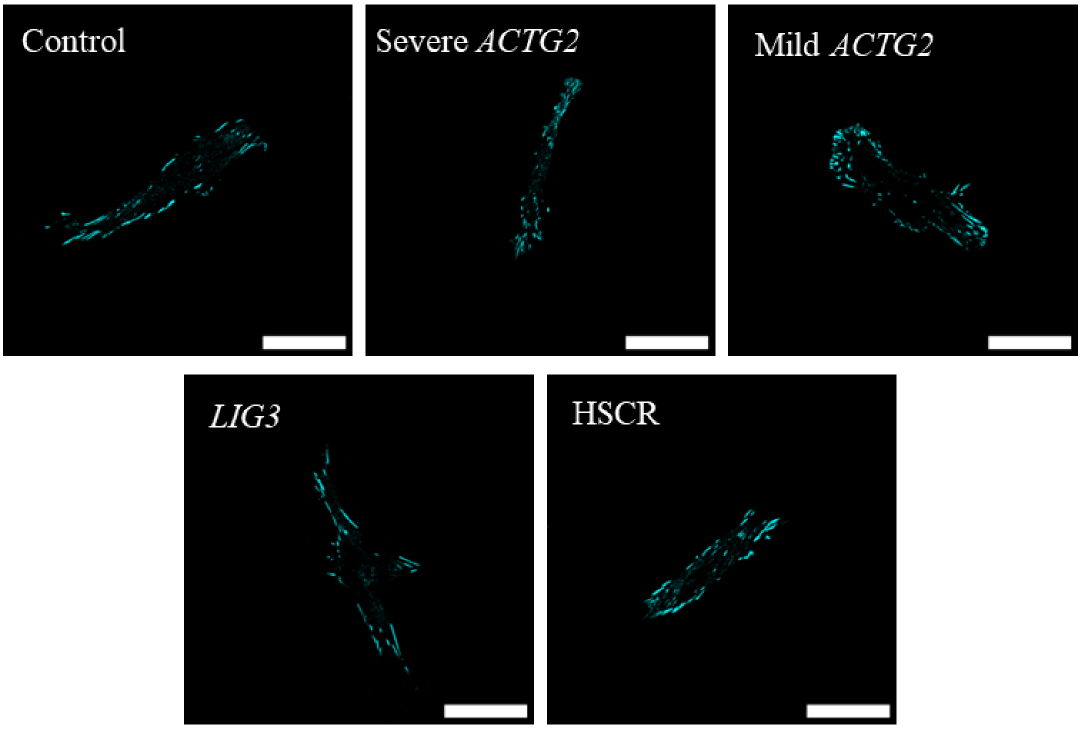

Figure 4.10: (a) Representative HDFs images of focal adhesions, stained with vinculin. Cells were seeded on collagen coated glass coverslips and imaged with Zeiss confocal LSM 980 microscope using 40x oil immersion objective. Scale bar = 50μm.

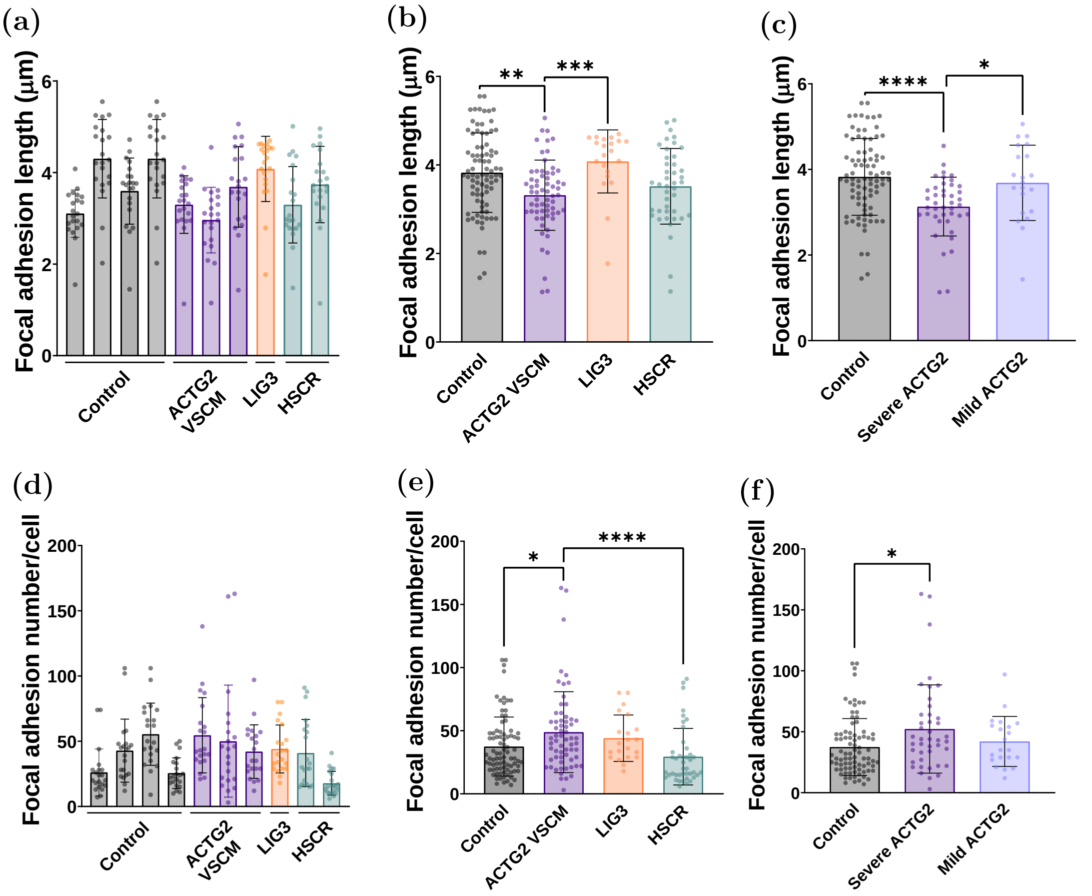

Figure 4.11: Focal adhesions structure in HDF cells. Quantification of individual cell lines (_n=21 cells_) for (a) focal adhesion length and (d) number of focal adhesions per cell. Quantification of control cell lines (_n=84 cells_), VSCM affected cell lines (_ACTG2_-VSCM caused by R257C or R38H) (_n=63 cells_), _LIG3_ cell line (_n=21 cells_), and HSCR cell lines (_n=42_) for (b) focal adhesion length [_** P=0.0030; ***P=0.0005_] and (e) number of focal adhesions per cell [_* P=0.0441; **** P<0.0001_]. Quantification of control (_n=84 cells_), severe _ACTG2_-VSCM affected cell lines (R257C, _n-42_), and _ACTG2_-mild VSCM affected cell line (R38H, _n=21_) for (c) focal adhesion length [_* P=0.0339; **** P<0.0001_] and (f) number of focal adhesions per cell _* P=0.0451_]. All graphs show mean ± SD with circles representing individual cell measurements. Statistical significance was determined using Kruskal-Wallis test with Dunn's post hoc multiple comparison test.

4.3.5 Cell migration is increased in VSCM cells

After observing differences in actin retrograde flow between control and *ACTG2*-VSCM cells, the migration of HDF cell lines was studied over a 24-hour period using the label-free method of digital holographic microscopy. The average distance travelled by cells in selected areas was calculated, followed by linear regression analysis to determine the average speed of a cell in the selected area. Figure 4.12 a shows VSCM cell lines travelled at a faster speed compared to control, *LIG3*, HSCR cells. On average, *ACTG2* associated VSCM cells travelled twice as fast as control cells; VSCM cells had an average speed of 4μm/hour compared to 2μm/hour for control cells (Figure 4.12 b). Moreover, the significantly faster migration time was observed when comparing *ACTG2*-VSCM cells to controls, regardless of disease severity (Figure 4.12 c).

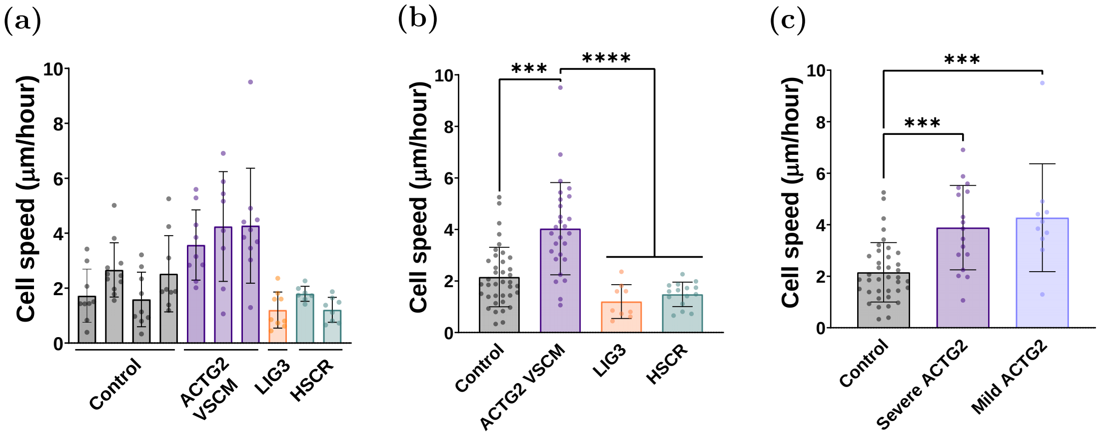

Figure 4.12: Cell migration in HDF cells (a) Average cell speed of individual cell lines (b) Average cell speed of control cell lines, VSCM affected cell lines (VSCM caused by *ACTG2* variants R257C or R38H), *LIG3* and HSCR cell lines. _*** P=0.0002; **** P<0.0001._ (c) Average cell speed of control cell lines, severe *ACTG2*-VSCM affected cell lines (R257C) and mild *ACTG2*-VSCM affected cell lines (R38H). _** P= 0.0020; *** P=0.0006._ 21 cells were analysed for each cell line. Graphs show mean ± SD with circles representing individual cells measurements. Statistical significance was determined using Kruskal-Wallis test with Dunn's post hoc multiple comparison test.

4.4 Discussion

Differences in mechanotransduction between *ACTG2* associated VSCM cells and control cells were investigated in Chapter 3. These observed changes lead to the exploration of using 'force exerted by VSCM cells' as a label-free disease biomarker which in turn showed promising results. However, the differences present in mechanotransduction for *ACTG2*-VSCM cells also prompted further questions about the role of cell migration in *ACTG2* associated VSCM as mechanotransduction has been known to affect actin cytoskeleton dynamics which greatly impacts cell movement [122, 123]. Thus, in this chapter, cell morphology and actin retrograde flow in *ACTG2* associated VSCM were studied in order to establish if VSCM alters characteristics that contribute to cell migration. This was followed by an investigation into whether cell migration could be used as a label-free biomarker for VSCM.

4.4.1 Morphological analysis of VSCM cell lines

The cell morphological features investigated in this chapter included cell area, nuclear area, cell axes, cell eccentricity, Haralick textural features, and focal adhesions. Quantification of the cells structure, as seen in Figures 4.5 to Figure 4.11, indicated that there were no phenotypic differences between *ACTG2*-VSCM and control cells in terms of cell area and nuclear area. This was consistent with morphological analysis carried out by Viti and colleagues, but differs from findings by Hashmi *et al.,* which concluded VSCM cells spread over a larger area [59,82]. The difference observed in results could be attributed to the use of primary HDF cells in this thesis compared with the Hashmi's work where transfected commercial primary human intestinal smooth muscle cells (HISMC) were studied. Furthermore, in this chapter it was established that *ACTG2*-VSCM cells had a longer major axis length and higher values for cell eccentricity implying cells are more elongated compared to healthy controls. At the time of this work, major axis length of cells had not been studied in VSCM. The longer major axis length quantified in VSCM cells could be an indicator of altered cell growth and/or cell division which warrants further investigation. Additionally, the conclusions on cell eccentricity were in line with Hashmi *et al.,* where it was stated that VSCM cells are more elliptical in comparison to wild type cells. [59].

Moreover, Haralick textural features were analysed to determine actin distribution and organisation by quantifying changes in actin cytoskeleton intensity. Haralick contrast is a measure of variation in an image, where images with values closer to 0 have less contrast. Haralick entropy measures the complexity of an image. Higher values of entropy are associated with more complex images [136]. Figure 4.7 showed *ACTG2* associated VSCM cells have smaller Haralick contrast compared with control and *LIG3*-CIPO cells. This implies *ACTG2*-VSCM cells have more homogeneous actin distribution. *ACTG2* associated cells also have lower values for Haralick entropy, suggesting more regular and structured pattern of actin filaments. It should also be noted, when *ACTG2* associated VSCM cells were grouped into severe VSCM (R257C) and mild VSCM (R38H), differences were only observed between severe VSCM and control cells implying it is better to use Haralick features to differentiate between healthy and severe VSCM. It should be noted that Haralick textural analysis results differs from work carried out by Viti *et al.,*, with the main difference between the work being the cell density. In this chapter Haralick textural analysis was carried out on single cells whereas Viti's work was on a denser monolayer [82].

Haralick features have been used for diagnostic purposes on numerous occasions such as by Simonthomas and colleagues who developed a software based on Haralick features in order to diagnose glaucoma from retinal photographs and were able to successfully diagnose 98% of cases [139]. Additionally, lung abnormalities have been identified with 86% success from Haralick textural analysis on X-Ray images and lung CT scans [140]. It is important to note that the use of Haralick textural analysis to successfully diagnose conditions has not been shown at a cellular level and whilst its potential for diagnosis has been highlighted here, it is currently not a diagnostic technique in the clinical setting.

4.4.2 Molecular clutch engagement

Actin retrograde flow speed was quantified in order to investigate if VSCM alters actin polymerisation and as a result impacts molecular clutch engagement. As presented in Figure 4.9, actin retrograde flow speed is faster in *ACTG2* associated VSCM cells compared to control cells implying that the molecular clutch is less engaged in VSCM cells [129]. This suggests actin polymerisation is accelerated in VSCM which opposes the widely accepted hypothesis that actin polymerisation is impaired in VSCM [18,63]. Halim *et al.,* have shown mutations in *ACTG2* reduce actin polymerisation. It should be noted that this work was carried out on different *ACTG2* mutations (R40C, R63Q, R178H, R178C and R178L) compared to the ones used in this thesis (R257C and R38H) [18]. Furthermore, recent findings in May 2024 from Heuckeroth's group, where they used a pyrene-actin polymerisation assay, demonstrated that actin polymerisation can be affected in different ways depending on the *ACTG2* mutation causing VSCM. Heuckeroth's group showed variant R257C (severe *ACTG2*-VSCM) causes significantly faster polymerisation compared to wild type cells whereas variant R40C resulted in slower actin polymerisation. There was no investigation into the effects of R38H (mild *ACTG2*-VSCM) on polymerisation [35]. Additionally, the spectrum of disease severity for VSCM is as follows: R178<R257<R40<R38 [27]. No correlation between actin polymerisation and disease severity was evident when the results presented in this thesis and the conclusions from Heuckeroth's group were considered together [35]. Moreover, the actin polymerisation data from Heuckeroth's group also implied that findings from Halim's group and the results highlighted in Figure 4.9 of this thesis can both be accepted due to the lack of correlation in the spectrum of disease severity.

Due to the differences observed in actin retrograde flow speed, the molecular clutch engagement was further investigated by examining focal adhesion length and number. Figure 4.11 demonstrated that severe *ACTG2* associated VSCM cells had significantly shorter length of focal adhesions as well as an increased number compared to healthy controls. This implied severe VSCM disrupts stable focal adhesion formation and aligns with the increased actin flow speed and reduced traction force results presented in this thesis. Taking everything together, it can be concluded that severe *ACTG2* associated VSCM causes disengagement of the molecular clutch [141]. Also, despite not observing significant differences in focal adhesion number and length for the mild form of *ACTG2*-VSCM, actin flow speed and traction force findings were in line with the disengaged state of the molecular clutch model for VSCM.

4.4.3 Cell migration as a biomarker for VSCM

Quantification of 24-hour cell migration in *ACTG2* associated VSCM cells, shown in Figure 4.12, illustrates VSCM significantly increases cell migration compared to control cells. These findings are consistent with previous work carried out by Viti *et al.*, who investigated migration using a 31 hour wound healing assay and presented a trend where VSCM cells migrated faster than control cells, with a significant acceleration in speed observed from 16 hours onwards [82]. Increased migration in VSCM cells has also been reported by Hashmi *et al.,* where they tracked cell migration for 12 hours using a fluorescent nuclear probe and found cells with R257C *ACTG2* mutation had an 11% higher migration rate compared to wild type cells.

Moreover, cell migration can also be related to the molecular clutch model, as the model is used to describe the interplay between actin retrograde flow and migration. Theoretically, the relationship between the two is thus inverse, as actin retrograde flow increases cell migration speed should decrease [129]. When the clutch is disengaged actin retrograde flow is faster causing an increase in actin polymerisation at the lamellipodia. This results in the formation of less stable focal adhesions, allowing cells to exert less force on the extracellular matrix, and preventing the cell from propelling forward [130, 141]. However, this was not observed from the work carried out in this thesis which illustrates a linear relationship between actin retrograde flow speed and cell migration as seen in Figures 4.9 and 4.12 where both have a 2 fold increase in VSCM compared to non-CIPO control cells. It is widely known that the molecular clutch model is highly complex and contributions from many different factors including integrins, and adaptor proteins can also influence the model. Moreover, it is important to realise that actin retrograde flow is produced both by cytoskeletal assembly and contractility. If either is impaired (as is the case in VSCM) this could result in apparently contradictory findings, as the cytoskeleton cannot withstand the force loading rate and breaks, even if the clutch is engaged [142]. Additionally, the increased migration observed may be due to factors outwith the molecular clutch model such as biochemical changes within a cell, the effects of mechanotransduction, and the extracellular matrix properties [124, 143].

Thus, in theory, *ACTG2*-VSCM cells should be less migratory compared to control cells, but this is not the case. The linear relationship between actin retrograde flow and cell migration may be a result of the dynamic nature of the molecular clutch model where the coupling between the actin cytoskeleton, focal adhesions, and the extracellular matrix is strong enough to counteract the effects of the retrograde flow of actin allowing cells to become more migratory. The following chapter will explore how changes in the metabolic profile in a cell may have influenced cell migration.

The significant differences between *ACTG2* associated VSCM and control cells highlights the potential for migration to be used as a label-free biomarker for VSCM. In the migration work carried out in this thesis, the commercially available HoloMonitor microscope was used. Although the microscope was effective in cell tracking, the field of view is small which limits the number of cells that can be tracked. Moreover, the HoloMonitor is extremely sensitive to environmental factors such as vibrations which can occur, for example, as a result of other nearby equipment or general use of the location where the microscope is stored. This can cause blurry and distorted images, resulting in difficulty obtaining measurements. These problems can be mitigated by carrying out more technical repeats and placing the HoloMonitor in a separate incubator to reduce the impact of vibrations from the environment. Digital holographic microscopy acts as a useful tool for cell migration tracking as it is a non-invasive technique that does not require any of the traditionally used dyes for cell tracking. These dyes can alter cell behaviour affecting the reliability of results as well as being toxic to cells in the long term [134, 135]. Furthermore, digital holography is also a cost-effective method compared to other microscopy systems and so would be a better candidate in a clinical setting. In order for cell migration tracking to be implemented more work needs to be carried out, which will be further explored in Chapter 6, section 6.6.

Overall, the results discussed in this chapter have been summarised in Figure 4.13. The schematic outlines the main differences observed between *ACTG2* associated VSCM and healthy cells.

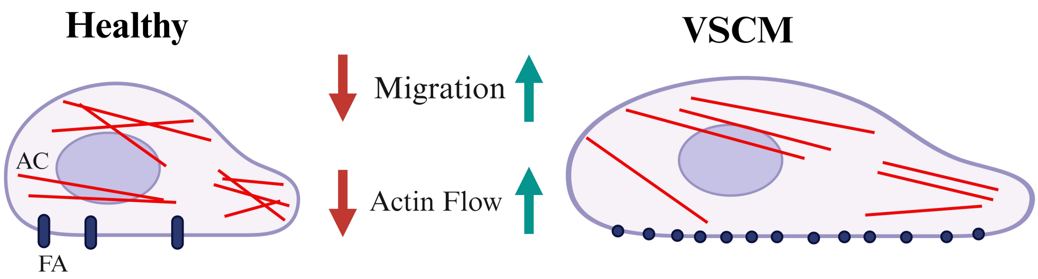

Figure 4.13: Schematic illustrating hypothesis on the effects of *ACTG2* associated VSCM as discussed in Chapter 4. Healthy and VSCM cells are shown with actin fibres as red lines (AC) and focal adhesion as blue rectangles (FA). VSCM cells are longer in major axis length and more elliptical in shape. VSCM cells have less complex and parallel actin cytoskeleton compared to healthy cells that have more complex and variable actin fibres, a shorter major axis length, and are more circular. VSCM cells have more focal adhesions but they are shorter in length. Cell migration, actin retrograde flow, and actin polymerisation increases in VSCM compared to healthy cells. Image created with BioRender.com

4.5 Conclusion

This chapter explored how cell morphology, actin retrograde flow, and cell migration differed in VSCM and control cells. In particular, Haralick textural analysis showed differences in actin organisation between severe VSCM and non-CIPO control as well as VSCM and *LIG3*-CIPO controls. *ACTG2* associated VSCM cells had an organised and more homogeneous distribution of actin fibres compared to the disorganised and random fibres present in control and *LIG3*-CIPO cells.

Moreover, actin retrograde flow speed, and thus actin polymerisation, was significantly faster in *ACTG2* associated VSCM compared to controls regardless of disease severity. Although actin retrograde flow speed had not been directly studied in the context of VSCM, the findings presented in this work align with that currently accepted in the field. Additionally, despite no correlation noted between actin retrograde flow and disease severity, it can not be concluded that actin retrograde flow was accelerated in VSCM regardless of the mutation causing VSCM as only two *ACTG2* mutations were studied.

Additionally, cell migration speed was tracked using digital holographic microscopy and showed *ACTG2*-VSCM cells had a two fold increase in migration speed compared to non-CIPO control cells. *ACTG2* associated VSCM was also significantly faster than non-*ACTG2* control cells, *LIG3*-CIPO and HSCR. Overall, the migration results highlight the potential for cell migration to be used as a biomarker for VSCM drug screening and diagnostic purposes.

5 | Characterising *PIEZO1* Associated VSCM

5.1 Introduction

The Piezo family of proteins, consisting of Piezo1 and Piezo2, are mechanosensitive cation channels found in the lipid bilayer of cells [144]. Mechanosensitive proteins can sense changes in mechanical force in the cell membrane and respond accordingly. Piezo1/2 are highly conserved proteins that consist of 30-40 transmembrane domains making them the largest known protein channels [145]. Piezo1 responds to mechanical stimuli such as shear stress and can be found in various different locations including kidneys, lungs, skin, and intestine. Piezo2 is involved in proprioception and touch; it is mainly found in merkel cells and sensory neurons [146].

Piezo1 is a functional trimer, consisting of a central transmembrane ion pore (a hollow channel with an extracellular cap), three internal beams, and three 'blade-like' structures which are able to sense the external environment [145,147]. Piezo1 is a non-selective cation channel which opens in response to mechanical stimulation. Once open, an influx of cations such as calcium trigger numerous downstream biochemical pathways that can influence the cells physiological behaviour [148].

Mechanosensitive ion channels open in a method known as gating which is usually modulated by voltage or ligand binding but can also be mechanical as in the case of Piezo1 [149]. The specific mechanogating mechanism of Piezo1 is not fully understood yet. There are two major paradigm for mechanogating in membrane channels: 'force from lipids' (FFL) and 'force from filament' (FFF). FFL suggests that mechanosensitive channels are activated only from stimulation by the lipid bilayer itself whereas FFF suggests that the actin cytoskeleton also plays a role in activation due to the membrane being tethered to the actin filaments [146]. However, work carried out by Patapoutian's group and Martinac's group has showed that when the lipid bilayer is not connected to the actin cytoskeleton, tension from the bilayer alone is enough to activate Piezo1 [150, 151]. Therefore, FFL is currently widely accepted as the most probable mechanism for mechanogating. Specifically, in terms of Piezo1, Lewis and Grandl used the patch clamp method to show that Piezo1 activates due to FFL where the membrane curvature act as a mechanism to store the elastic energy [152]. However, recent studies, which are gaining traction, have pointed towards a parallel and/or co-operative approach between FFL and FFF in Piezo1/2 activation [149, 153, 154]

PIEZO1 mutations have resulted in dehydrated hereditary stomatocytosis, generalised lymphatic dysplasia and Prune-belly syndrome [155–160]. Dehydrated hereditary stomatocytosis is a rare form of hemolytic anaemia caused by gain of function mutations in *PIEZO1.* This autosomal dominant disease causes defects in the membrane of red blood cells resulting in increased influx of ions [157–159]. Several cases of autosomal recessive generalised lymphatic dysplasia have been reported due to loss of function mutations in *PIEZO1.* This disorder affects contraction of lymphatic vessels, preventing drainage of lymphatic fluid and causes inflammation as a consequence [155, 156]. Furthermore, Amado *et al.,* in January 2024, found a loss of function *PIEZO1* mutation to cause Prune-belly syndrome, also known as Eagle-Barrett syndrome. The variants were S2195L which impacted transmembrane domain 37, otherwise known as the central pore domain and G253R affecting transmembrane domain 7. Prune-belly syndrome is a rare disorder which primarily affects the abdominal wall, urinary tract as well as impacting the distention of testes [160]. It is important to note that Prune-belly syndrome often results in problems with the contractile phenotype of smooth muscle cells which is a similar phenotype to VSCM [15].

Additionally, mutations in *PIEZO1* have also been linked to several other disorders. These include pancreatitis, hyperglycemia, glioma, oral squamous cell carcinoma, cholangiocarcinoma, hepatocellular carcinoma, and ovarian cancer [31, 53, 161–165]. In these instances, Piezo1 channel is affected by the disease and does not cause the condition.

At the time of this thesis, there was no known published work which links *PIEZO1* mutations to causing VSCM. However, *PIEZO1* has been found to be overexpressed in Crohn's disease which is an inflammatory intestinal disorder [166]. Additionally, as stated above, Prune-belly syndrome is characterised with gastrointestinal abnormalities that overlap with VSCM symptoms and now a *PIEZO1* mutation has been identified to cause the syndrome [15, 160].

This chapter explores the effects on cellular behaviour of the novel *PIEZO1* mutations S1814F (c.5441C>T) and P2230L (c.6689C>T), which were identified in Sant'Orsola - Malpighi Polyclinic, Bologna, Italy. Morphology, mechanotransduction and the molecular clutch model of *PIEZO1* mutant cells were investigated to determine how *PIEZO1* associated VSCM compares to healthy controls and *ACTG2* associated VSCM. The data for control and *ACTG2*-VSCM cells was taken from Chapters 3 and 4. Greater detail and discussion on these conditions can be found throughout Chapters 3 and 4. This chapter will only present a summary of data previously discussed from healthy control and *ACTG2*-VSCM cells in order to determine how *PIEZO1*-VSCM compare to VSCM caused by *ACTG2* mutations. Furthermore, metabolomic analysis was carried out on control, *PIEZO1*-VSCM and *ACTG2*-VSCM cells to establish if metabolic differences exist between the control and VSCM cells as well as between the different mutations associated with VSCM. Metabolomics was utilised to study the cell phenotype at a biochemical level as it provides quantifiable model of changes in the biochemical activity between healthy control and VSCM cells.

5.2 Materials and methods

The materials and methods outlined in this section can be found throughout this work. Specifically cell culture is outlined in Chapter 2, section 2.3.2; immunofluorescence assays in Chapter 2, section 2.3.3; YAP image analysis in Chapter 3, section 3.2.1; Cell morphology and focal adhesion analysis in Chapter 4, section 4.2.1; micropillar arrays in Chapter 3, section 3.2.2; actin retrograde flow in Chapter 4, section 4.2.3; and digital holography in Chapter 4, section 4.2.4. The methods specific to this chapter are outlined below in section 5.2.1.

Information on cell lines used and cell culture conditions can be found in Chapter 2, table 2.1. For, the work carried out in this chapter, the following cell lines were used: control cell lines (C1-C4), *ACTG2*-VSCM cell lines (S1, S2, &M1), and *PIEZO1*-VSCM cell line (P1).

5.2.1 Metabolomics

Whole cell metabolomics was carried out on control (patient ID: C1), VSCM caused by *ACTG2* mutations (patient ID: S1, S2, M1) and VSCM caused by *PIEZO1* mutations (patient ID: P1) cells. Cell pellets containing 100,000 cells for each variants were prepared, except for the *PIEZO1* variants where pellets contained 10,000 cells due to low cell density. Pellets were stored at -80°C until metabolite extraction.

Cells were lysed using extraction buffer containing chloroform: methanol: water mixture (1:3:1 ratio). Samples were shaken at 4°C for an hour, followed by gentrification at 14,000 xg for 15 minutes at 4°C. Supernatants were collected for hydrophilic interaction liquid chromatography-mass spectrometry (HILIC-MS) carried out by Glasgow Polyomics using Dionex UltiMate 3000 RSLC system (ThermoFisher), ZIC-pHILIC column running at 300 μl/min (150mm $\times$ 4.6mm, 5μm column, Merck Sequant) and Orbitrap QExactive (ThermoFisher). An IDEOM worksheet, where data was normalised against the control sample and by cell number, was generated for identifying and filtering metabolites. This was followed by applying base 2 logarithm (log2) for further normalisation and data stabilisation. Analysis was carried out using MetaboAnalyst 6.0 and Qiagen's Ingenuity Pathway Analysis (IPA) software version 01-22-01. P-values were calculated through IPA using the default recommended test which is normally used for analysis carried out with IPA.

5.3 Results

5.3.1 Examining morphological differences caused by *PIEZO1* mutations

Cells were seeded on collagen coated glass coverslips for 24 hours before immunostaining in order to determine if the *PIEZO1* mutations results in morphological changes. Figure 5.1 shows representative images of control, *ACTG2*-VSCM, and *PIEZO1* associated VSCM cells.

From Figures 5.2a and c, it was clear that *PIEZO1*-VSCM cells had a larger surface area and a longer major axis length compared to healthy controls and *ACTG2* associated VSCM cells. Furthermore, the nuclear area was larger in *PIEZO1*-VSCM cells compared to *ACTG2*-VSCM cells but not in comparison to control cells. Additionally, Figures 5.2c and d showed that the major and minor axis lengths were significantly longer in *PIEZO1*-VSCM cells versus control cells. The major axis length in *PIEZO1* associated cells had no significant difference from *ACTG2*-VSCM cells but the minor axis length is significantly larger in *PIEZO1*-VSCM cells. Moreover, no statistically significant differences were observed in cell eccentricity between *PIEZO1*-VSCM cells compared to control and *ACTG2*-VSCM cells.

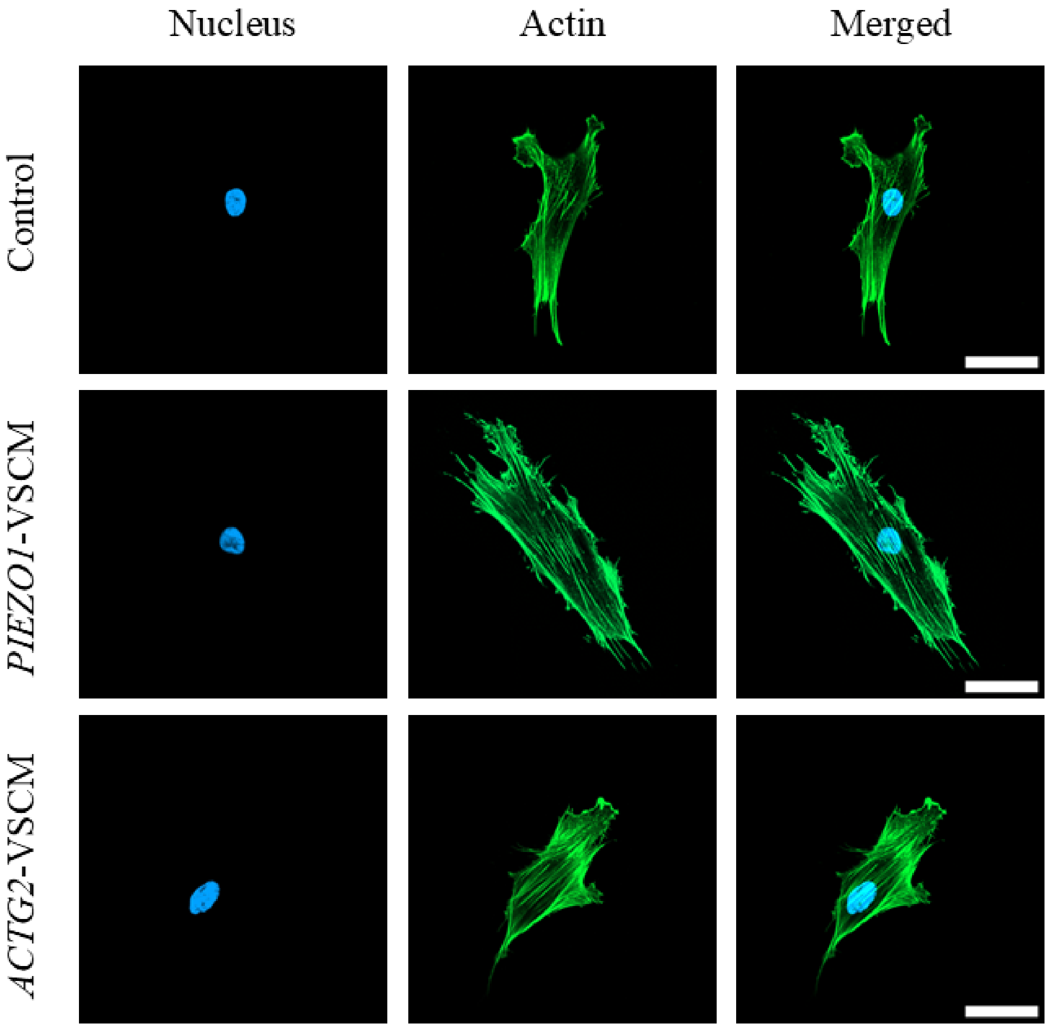

Figure 5.1: Representative images for cell morphology in control, *PIEZO1*-VSCM, *ACTG2*-VSCM HDF cells. Cells were seeded on collagen coated glass coverslips and imaged with Zeiss confocal LSM 980 microscope using 40x oil immersion objective. Images show nucleus (stained with DAPI, blue) and actin cytoskeleton (stained with phalloidin, green). Scale bar = 50μm.

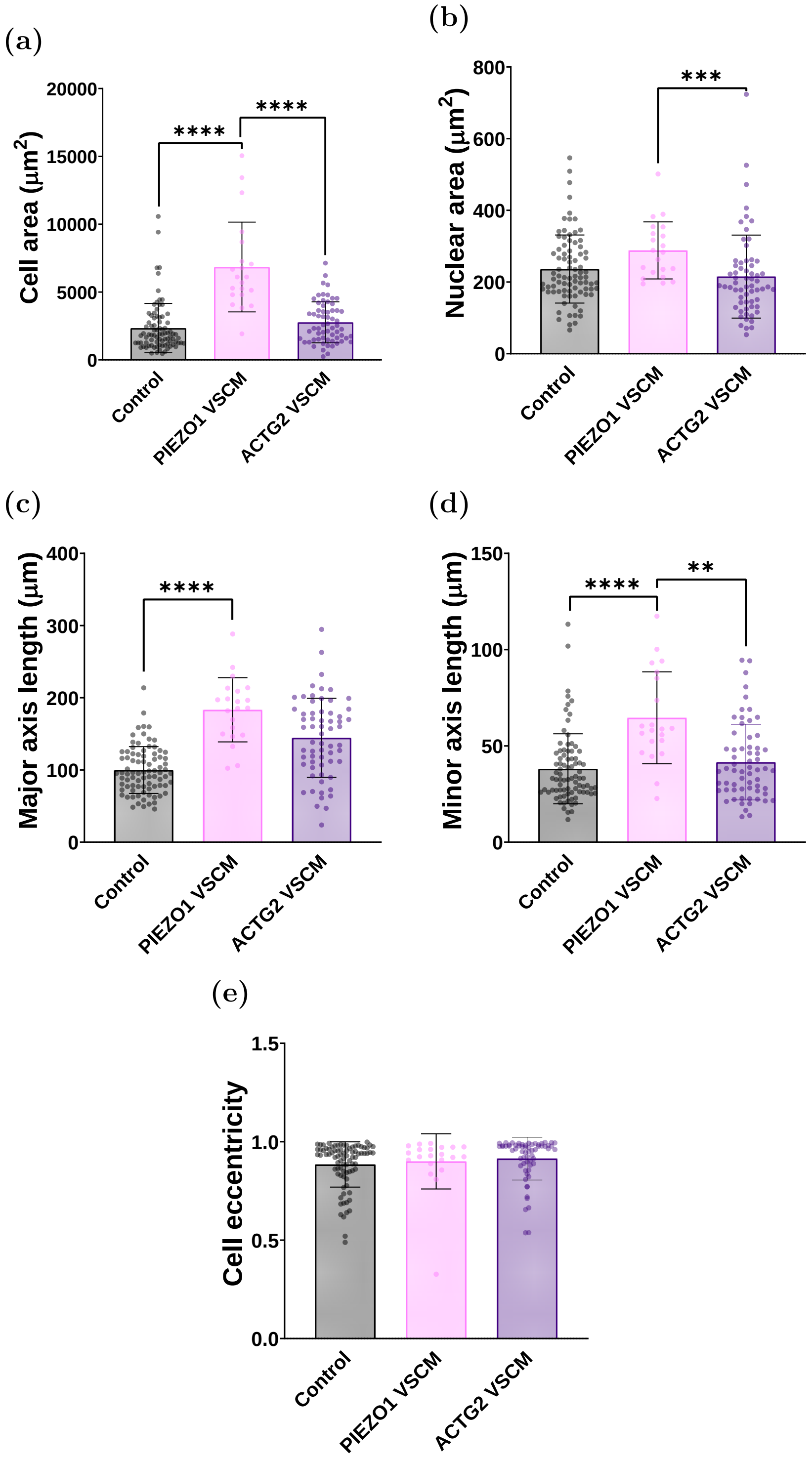

Figure 5.2: *PIEZO1* associated VSCM cells impact area and axis length. Quantification carried out of healthy control ($n=84$), *PIEZO1*-VSCM ($n=21$) and *ACTG2*-VSCM affected cell lines ($n=63$). Data for control and *ACTG2*-VSCM cells are duplicated from Chapters 3 and 4. All graphs show mean ± SD with circles representing individual cell measurements. (a) Cell area, **** $P<0.0001$ (b) Nuclear area, *** $P=0.0007$ (c) Major axis length **** $P<0.0001$ (d) Minor axis length, ** $P=0.0013$; **** $P<0.0001$ (e) Cell eccentricity. Statistical significance was determined using Kruskal-Wallis test with Dunn's post hoc multiple comparison test.

Furthermore, Haralick textural feature analysis was carried out to evaluate the organisation of the actin cytoskeleton. Figure 5.3 illustrated that there were no significant differences between *PIEZO1* associated VSCM and control cells in Haralick contrast and entropy. However, *PIEZO1*-VSCM cells had significantly higher Haralick contrast and entropy values compared to *ACTG2*-VSCM.

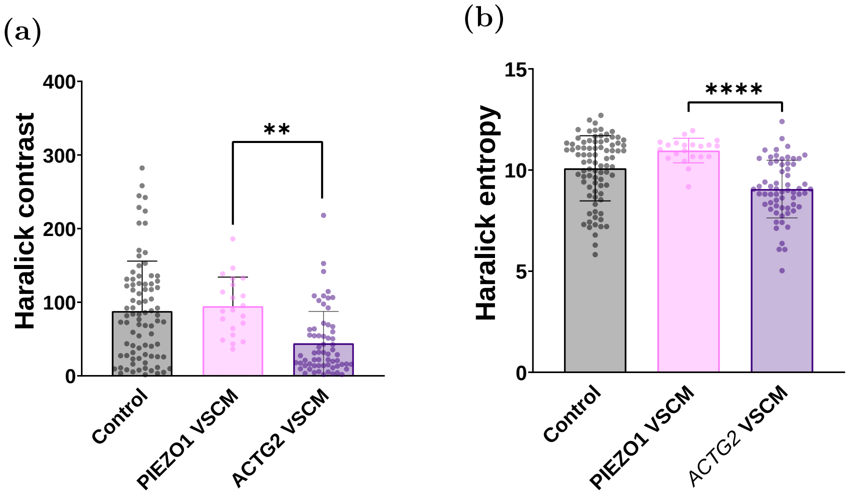

Figure 5.3: Haralick textural feature analysis of actin cytoskeleton in *PIEZO1*-VSCM differs from *ACTG2*-VSCM. Quantification carried out of healthy control (*n=84*), *PIEZO1*-VSCM (*n=21*) and *ACTG2*-VSCM affected cell lines (*n=63*). Data for control and *ACTG2*-VSCM cells are duplicated from Chapters 3 and 4. All graphs show mean ± SD with circles representing individual cell measurements. (a) Haralick contrast, *** P=0.0017* and (b) Haralick entropy, ***** P<0.0001*. Statistical significance was determined using Kruskal-Wallis test with Dunn's post hoc multiple comparison test.

5.3.2 Mechanotransduction in *PIEZO1* associated VSCM cells

HDF cells were seeded on collagen coated glass coverslips, and allowed to adhere for 24 hours prior to YAP immunostaining. Representative images of control, *PIEZO1*-VSCM, and *ACTG2*-VSCM YAP localisation can be seen in Figure 5.4. Figure 5.5a demonstrates that *PIEZO1*-VSCM cells had increased YAP nuclear localisation compared to control and *ACTG2*-VSCM cells. Furthermore, as presented in Figure 5.5b the average forces exerted by cells were also significantly greater in *PIEZO1*-VSCM associated cells, whereas, *ACTG2* associated VSCM cells were found to exert less force compared to healthy control cells.

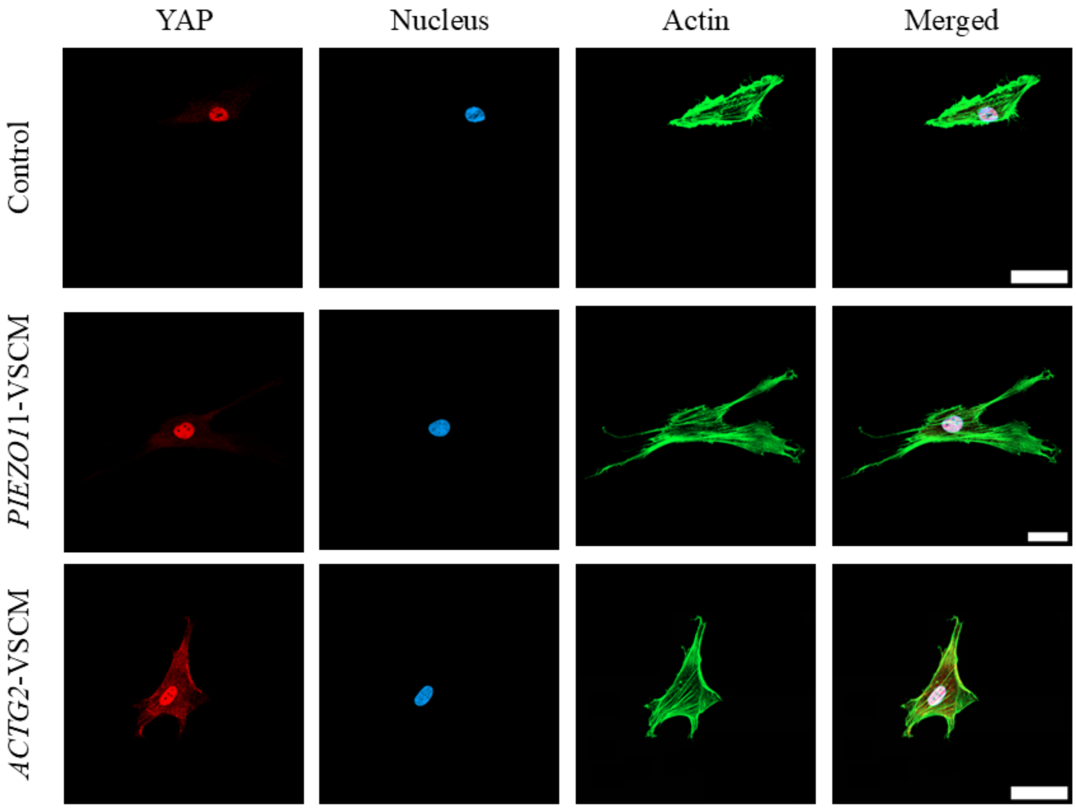

Figure 5.4: Representative image for YAP localisation in control, *PIEZO1*-VSCM, *ACTG2*-VSCM HDFs. Cells were seeded on collagen coated glass coverslips and imaged with Zeiss confocal LSM 980 microscope using 40x oil immersion objective Images show YAP (stained with YAP, red), nucleus (stained with DAPI, blue), and actin cytoskeleton (stained with phalloidin, green). Scale bar = 50μm.

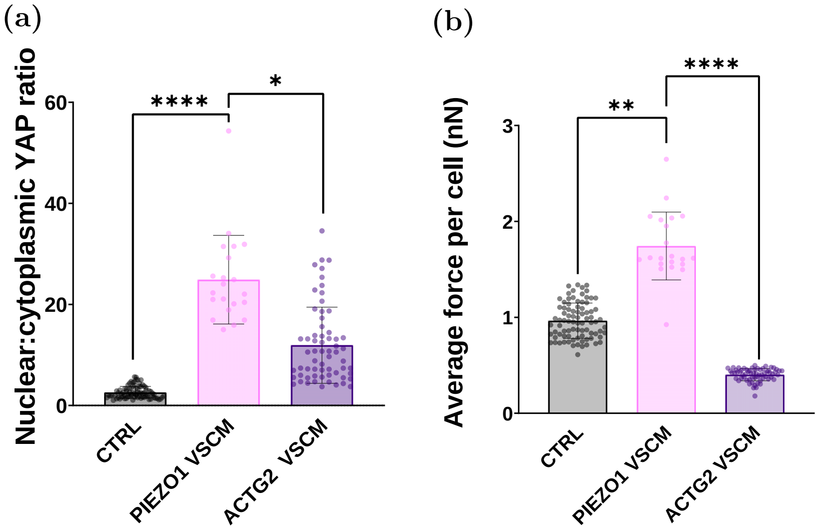

Figure 5.5: *PIEZO1* mutation causes differences in mechanotransduction (a) Nuclear:cytoplasmic YAP ratio of healthy control (*n=84*), *PIEZO1*-VSCM (*n=21*) and *ACTG2*-VSCM affected cell lines (*n=63*). ** P=0.0251; **** P<0.0001* (b) Average force exerted per cell (nN) on micropillar substrate in control, *PIEZO1*-VSCM, and *ACTG2*-VSCM. (*** P=0.0023; **** P<0.0001.* Graphs show mean ± SD with circles representing individual cells measurements. Statistical significance was determined using Kruskal-Wallis test with Dunn's post hoc multiple comparison test. Data for control and *ACTG2*-VSCM cells are duplicated from Chapters 3 and 4.

5.3.3 Molecular clutch mechanism is altered by ***PIEZO1*** mutation causing VSCM

The molecular clutch model in *PIEZO1* cells was investigated as differences in the molecular clutch between control and *ACTG2*-VSCM cells were observed in Chapter 4. Firstly, cells were incubated with SPY555-FastAct (table 2.3) for 2 hours prior to live imaging. This was followed by quantification of actin retrograde flow speed as illustrated in Figure 5.8. The actin flow speed in *PIEZO1* associated VSCM cells was significantly slower than control and *ACTG2*-VSCM cells.

Furthermore, vinculin immunostaining was carried out on HDF cells seeded on collagen coated glass coverslips. Figure 5.8 showed that *PIEZO1*-VSCM cells had longer focal adhesions than healthy controls and *ACTG2*-VSCM cells. However, in Chapter 4, it was observed that *ACTG2* associated VSCM cells had shorter focal adhesions than healthy controls. Additionally, similar to *ACTG2*-VSCM cells, *PIEZO1*-VSCM cells have more focal adhesions per cell compared to control cells.

Lastly, migration of *PIEZO1* cells over 24 hours was investigated using digital holographic microscopy. Figure 5.8 illustrated that *PIEZO1*-VSCM cells migrated slower than control and *ACTG2*-VSCM cells. However, it should be noted that *ACTG2*-VSCM cells migrated faster than healthy control cells, as previously discussed.

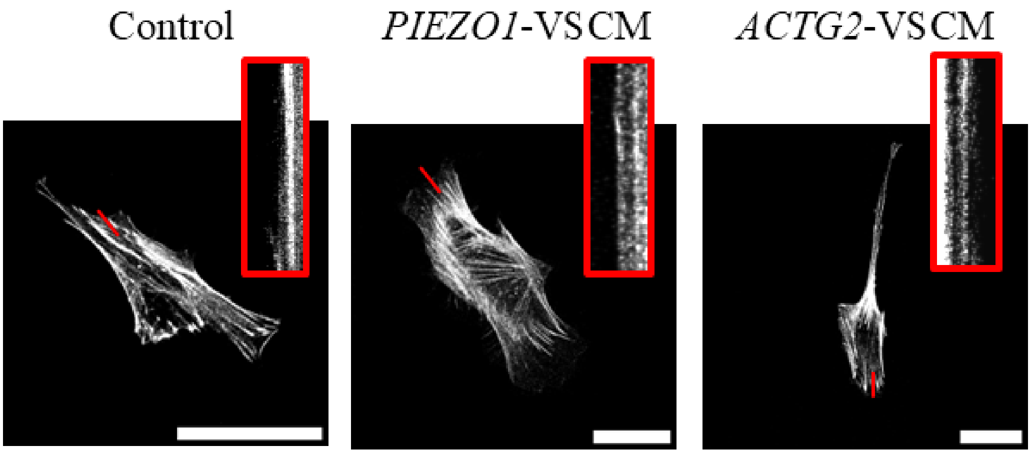

Figure 5.6: Representative image stack of actin retrograde flow with corresponding kymograph at top left for control, *PIEZO1*-VSCM, and *ACTG2*-cells. Cells were incubated with SPY555-FastAct and imaged with Zeiss confocal LSM 980 microscope using 40x oil immersion objective. Scale bars = 50μm.

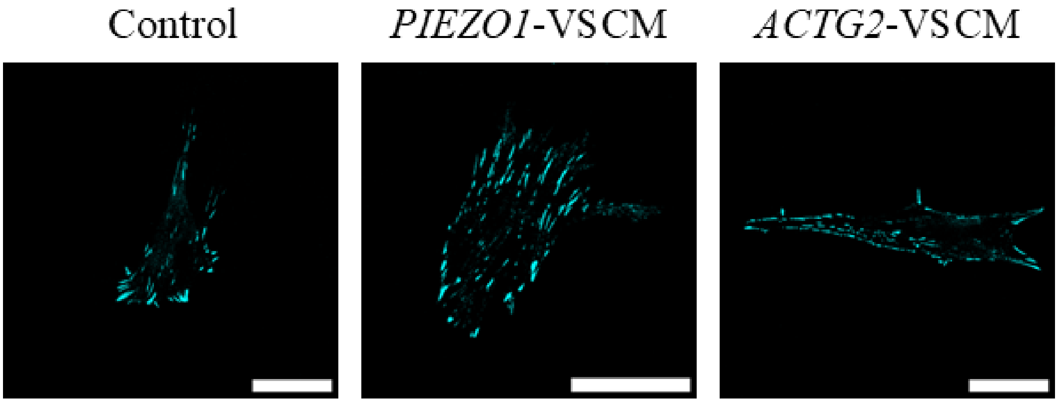

Figure 5.7: Representative image for focal adhesions in control, *PIEZO1*-VSCM, *ACTG2*-VSCM HDFs. Cells were seeded on collagen coated glass coverslips and imaged with Zeiss confocal LSM 980 microscope using 40x oil immersion objective. Images show focal adhesions stained with vinculin, blue. Scale bar = 50μm.

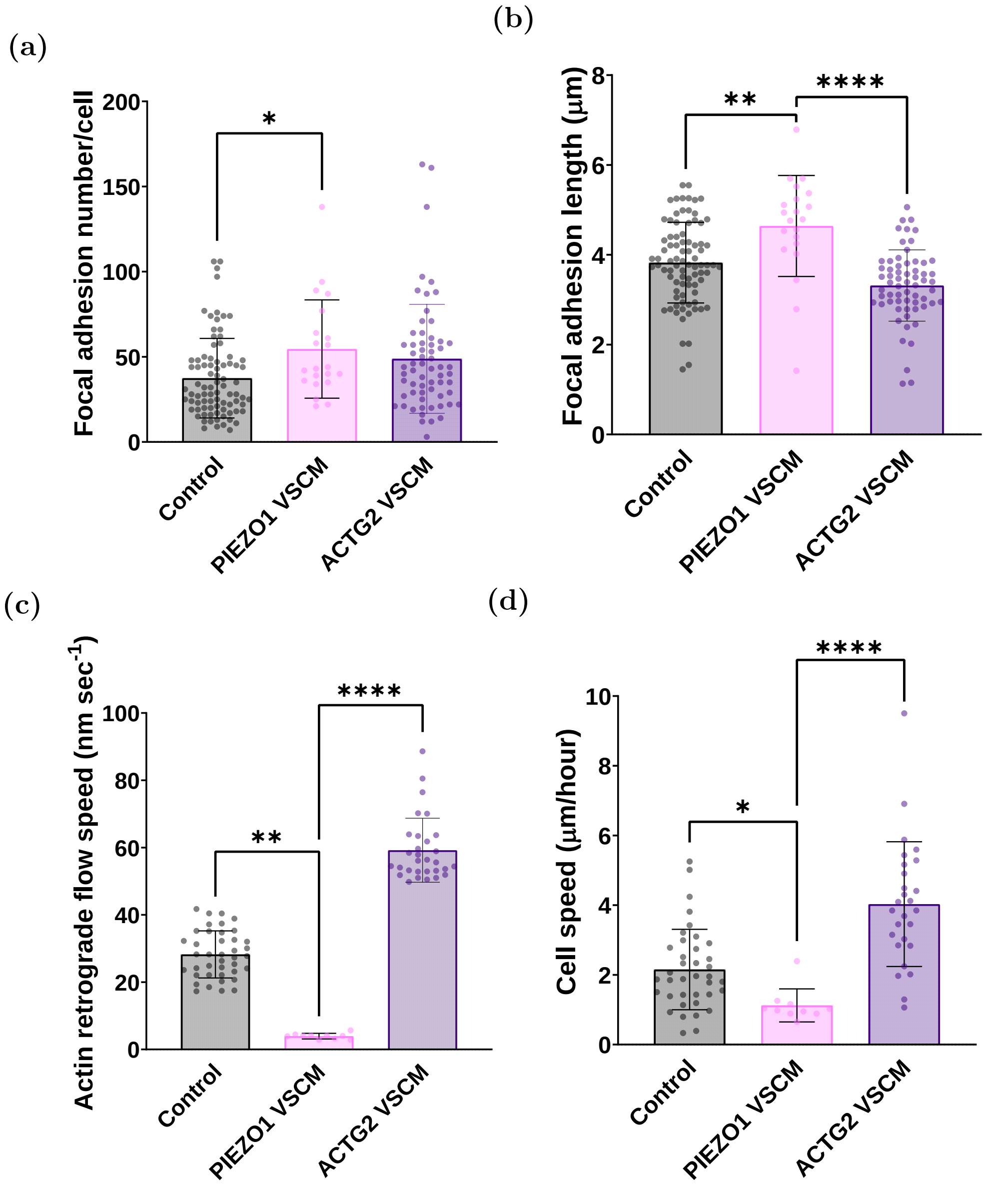

Figure 5.8: _PIEZO1_ mutation impacts the molecular clutch. _PIEZO1_-VSCM ($n=21$) were compared with healthy control ($n=84$) and _ACTG2_-VSCM affected cell lines ($n=63$). Data for control and _ACTG2_-VSCM cells are duplicated from Chapter 3 and 4. (a) number of focal adhesions per cell. _* P=0.0190; **** P<0.0001_ (b) Focal adhesion length _** P=0.0037; **** P<0.0001_ (c) Actin retrograde flow speed _** P=; **** P<0.0001_ (d) Cell speed (μm/hour). _* 0.0476 P=; **** P<0.0001_. Graphs show mean ± SD with circles representing individual cells measurements. Statistical significance was determined using Kruskal-Wallis test with Dunn's post hoc multiple comparison test.

5.3.4 ***PIEZO1*** **associated VSCM cells have a different metabolic profile compared to** ***ACTG2*** **associated VSCM cells**

The metabolic profile of *PIEZO1* associated VSCM cells and *ACTG2* associated VSCM cells in comparison to healthy control cells was investigated. Samples were prepared and sent for HILIC-MS to Glasgow Polyomics.

To gain an understanding of the overall differences in the metabolomes of *PIEZO1*-VSCM and *ACTG2*-VSCM cells, analysis was carried out using the MetaboAnalyst 6.0 software. Figure 5.9 showed heat maps of metabolites. *PIEZO1*-VSCM cells differed completely from healthy control cells in terms of metabolite regulation, as illustrated in Figure 5.9a. From Figure 5.9b, it can be seen that there were clear differences in the metabolic regulation between *ACTG2* associated VSCM cells and control cells. However, the degree of up/down regulation of metabolites in *ACTG2*-VSCM cells compared to control cells was not consistent across different patient samples. Additionally, Figure 5.9c highlighted the contrast in the metabolic profile of *PIEZO1* associated VSCM and *ACTG2* associated VSCM cells as when all samples were analysed together, the marked differences in the profile of *PIEZO1* cells resulted in the data being distorted. Thus, to mitigate this, the *PIEZO1*-VSCM cells and *ACTG2*-VSCM cells were analysed in separate groups.

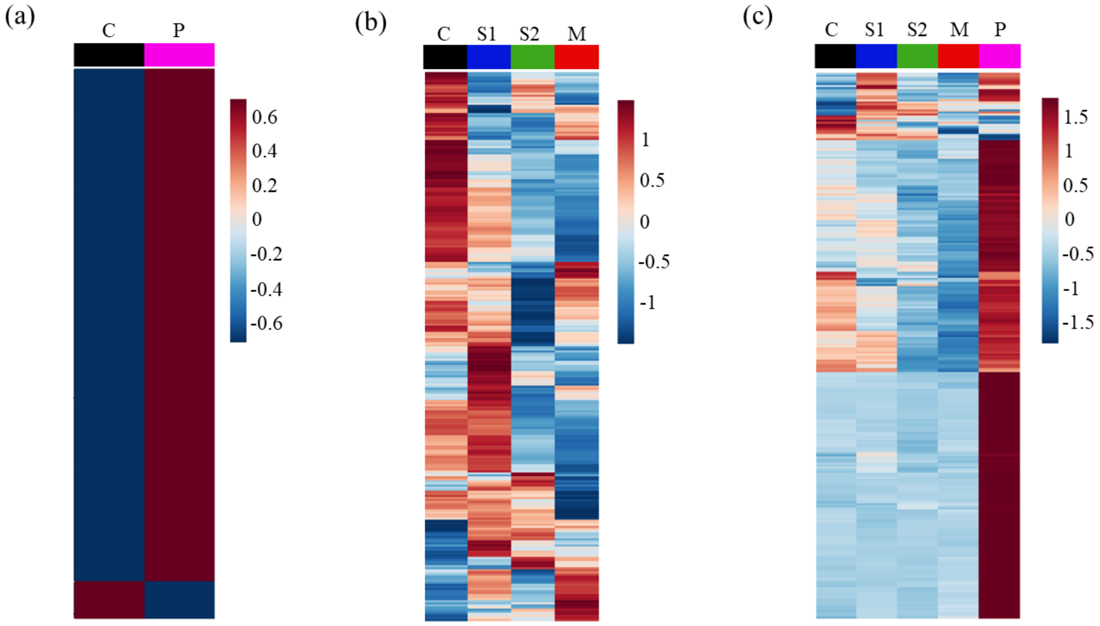

Figure 5.9: Overview of metabolic differences between control, *ACTG2*-VSCM, and *PIEZO1*-VSCM. Heat maps illustrating metabolites regulation differences in (a) control and VSCM caused by *PIEZO1* mutation (b) control, severe and mild forms of VSCM caused by *ACTG2* variants (R257C and R38H) (c) control, severe and mild forms of *ACTG2* associated VSCM, and *PIEZO1* associated VSCM. Each row represents a metabolite, and each column represents a sample. The colour gradient from blue to red indicates the relative abundance of metabolites, with blue representing lower abundance and red representing higher abundance. 'C' (black) = Control; 'S1' (blue) = severe *ACTG2*-VSCM 1 (R257C); 'S2' (green) = severe *ACTG2*-VSCM 2 (R257C); 'M' (red) = mild *ACTG2*-VSCM (R38H); and 'P1' (pink) = *PIEZO1*-VSCM. $n=4$ *technical repeats.*

Principle component analysis (PCA) was carried out to further understand how the metabolic profiles of *PIEZO1*-VSCM and *ACTG2*-VSCM cells differed from healthy controls. Figure 5.10a shows *PIEZO1* associated VSCM cells clustered in separate groups with PC1 representing a variance of 88% and PC2 a variance of 7.3%. Moreover, Figure 5.10b presented *ACTG2* associated VSCM variants and control cells on a plot where PC1 accounted for 54.8% variance and PC2 21.1%. The control cells were distinctly separate from all other samples indicating that the metabolic profile of the healthy control was significantly different from *ACTG2*-VSCM cells. The mild form of *ACTG2*-VSCM, shown in red, was far from the control cells compared to severe forms of the disease. One of the severe cell lines (blue, 'S1') clustered closest to the control along PC1 whereas the other severe cell line (green, 'S2') formed a cluster that was separate yet overlapping the mild form of VSCM. Collectively, these results implied disease severity does not impact the metabolic profile of *ACTG2* associated VSCM as mild (M1) and severe (S2) cluster together. Furthermore, there were differences in metabolic profile observed between the severe samples.

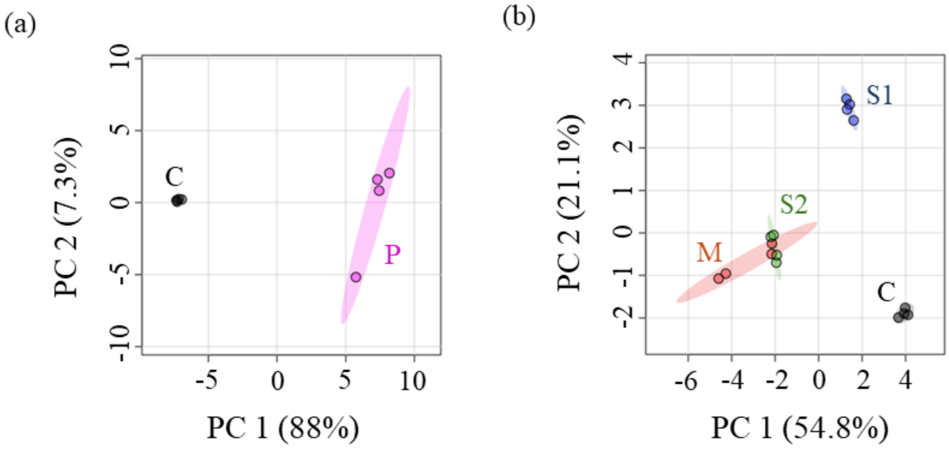

Figure 5.10: Comparison of metabolic profiles of healthy control, *ACTG2*-VSCM, and *PIEZO1*-VSCM cells. Graphs show Principal Component Analysis (PCA) scores plots with each point represents a technical repeat. (a) PCA plot of *PIEZO1*-VSCM and control sample (b) PCA plot analysis of *ACTG2*-VSCM variants and control samples. Black circles denote healthy control (C); red and green circles indicating severe forms of *ACTG2* associated VSCM (S1, S2); red circles representing mild form of *ACTG2* associated VSCM (M); and pink circles showing *PIEZO1* associated VSCM (P). The axes correspond to the first two principal components, which together explains the percentage (%) of the total variance in the dataset. *n=4 technical repeats.*

5.3.5 Investigating metabolic differences at the pathway level

Further analysis at the pathway level was carried out using Qiagen IPA software to gain a deeper understanding of how the metabolomes of *PIEZO1* associated VSCM cells and *ACTG2* associated VSCM cells differed from one another. Firstly, differences in the canonical pathways for each variant compared to the healthy control was analysed. Figures 5.11 to 5.14 showed that similar canonical pathways were impacted across *PIEZO1* and all *ACTG2* mutations causing VSCM. In particular, the metabolic clusters and biosynthesis pathways were the most significantly affected pathways with the largest number of overlapping genes. The biosynthesis pathway was the only one that affected *PIEZO1* and all *ACTG2* mutations. For *PIEZO1*-VSCM and severe *ACTG2*-VSCM (S1) the pathway had a negative z-score. Whereas, the pathways have a positive z-score in severe *ACTG2*-VSCM (S2) and mild *ACTG2*-VSCM.

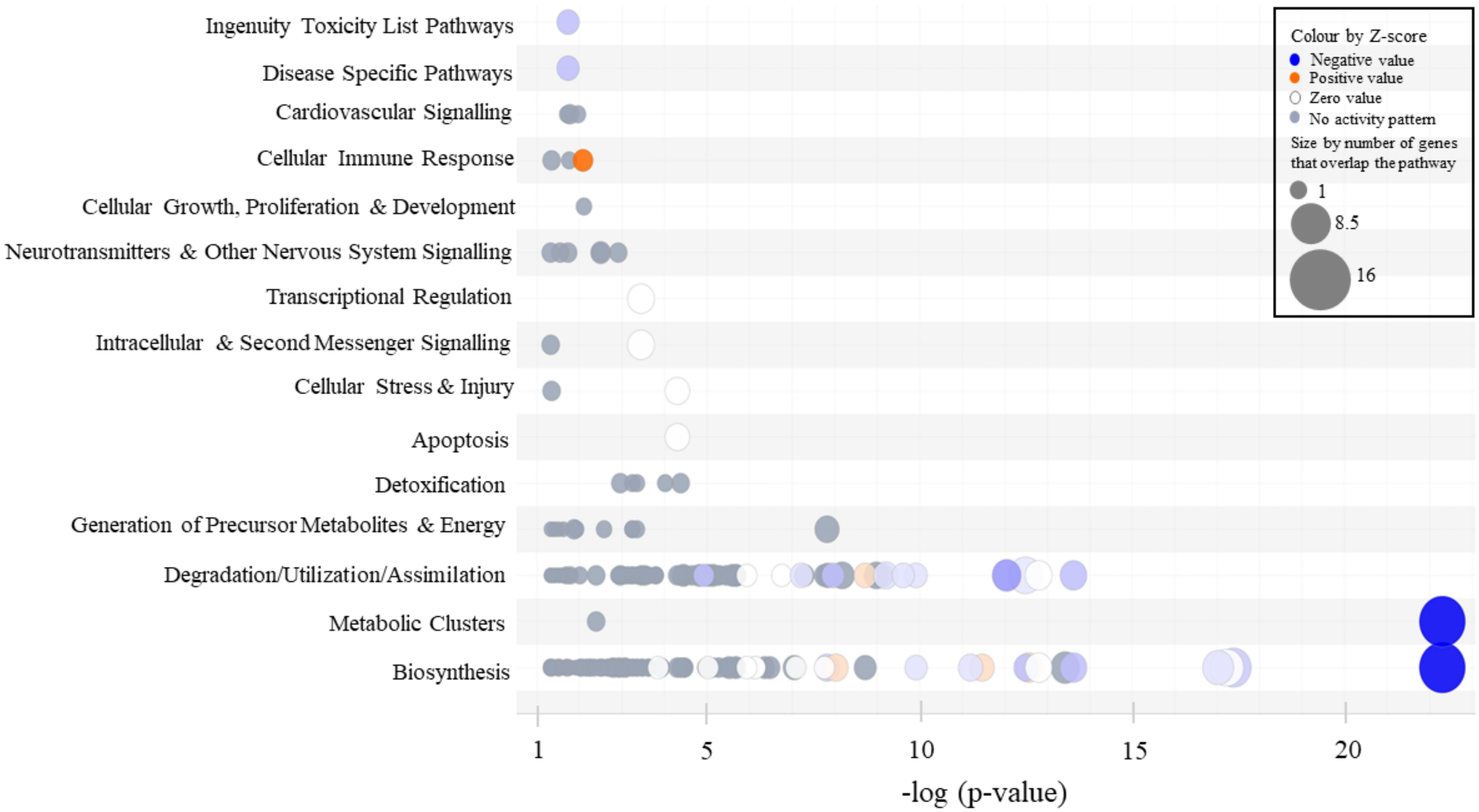

Figure 5.11: Canonical pathways affected in VSCM caused by *PIEZO1* mutation. Bubble size becomes larger with increasing number of overlapping genes in pathway. Z scores displayed by colour as shown in legend. P-value calculated by IPA through Fisher-exact test with Benjamini-Hochberg multiple-testing correction.

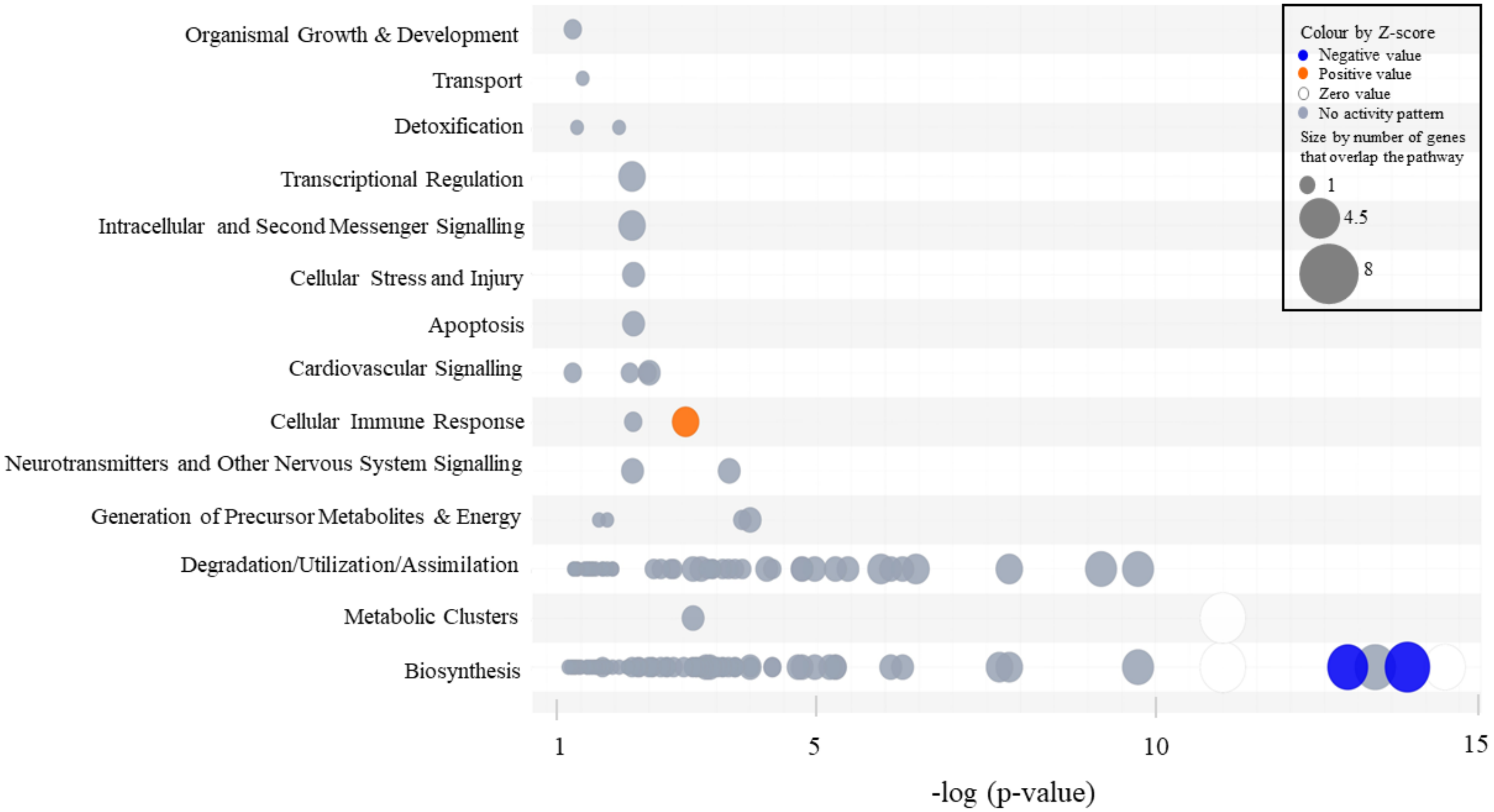

Figure 5.12: Canonical pathways affected in severe VSCM caused by R257C from sample S1. Bubble size becomes larger with increasing number of overlapping genes in pathway. Z scores displayed by colour as shown in legend. P-value calculated by IPA through Fisher-exact test with Benjamini-Hochberg multiple-testing correction.

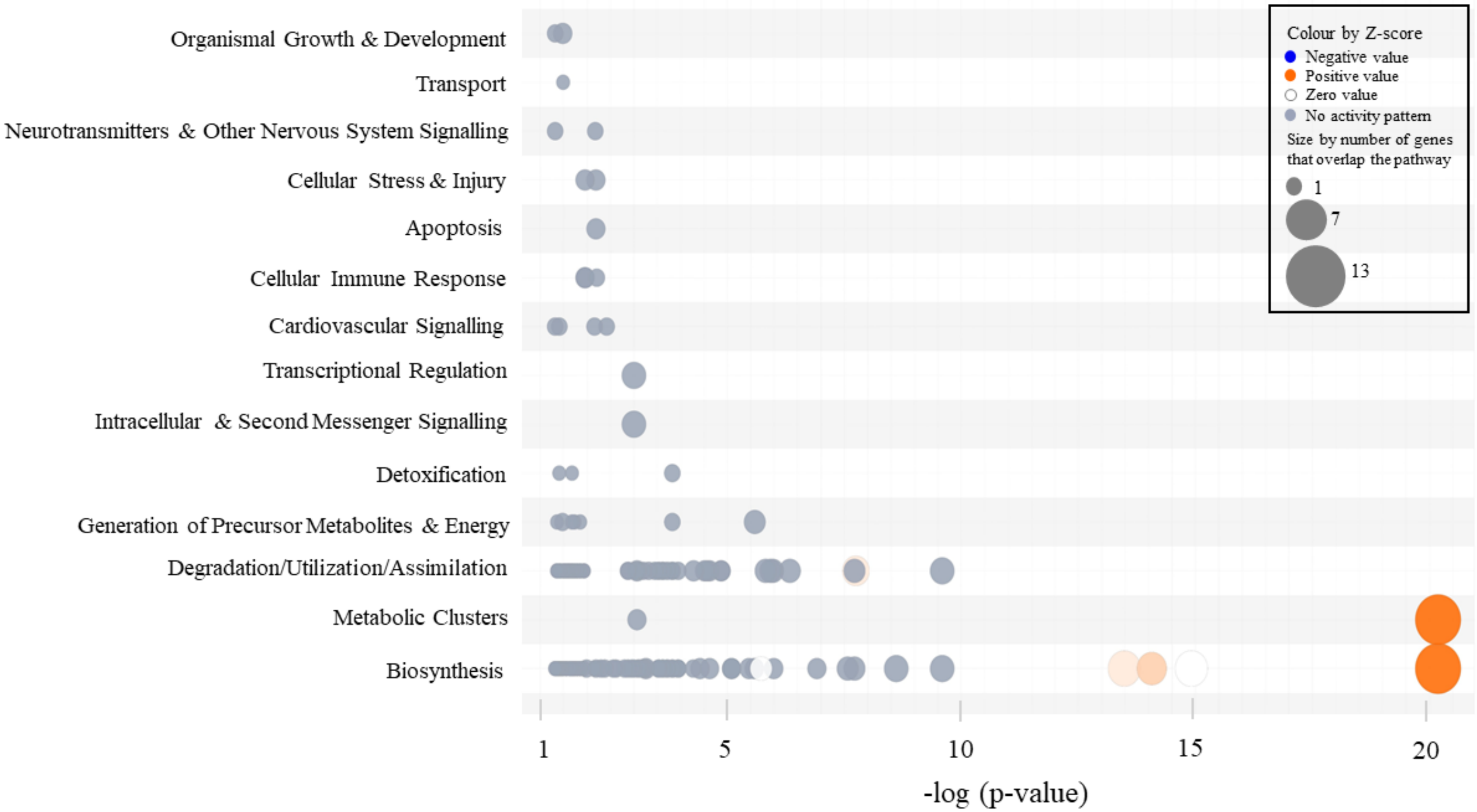

Figure 5.13: Canonical pathways affected in severe VSCM caused by R257C from sample S2. Bubble size becomes larger with increasing number of overlapping genes in pathway. Z scores displayed by colour as shown in legend. P-value calculated by IPA through Fisher-exact test with Benjamini-Hochberg multiple-testing correction.

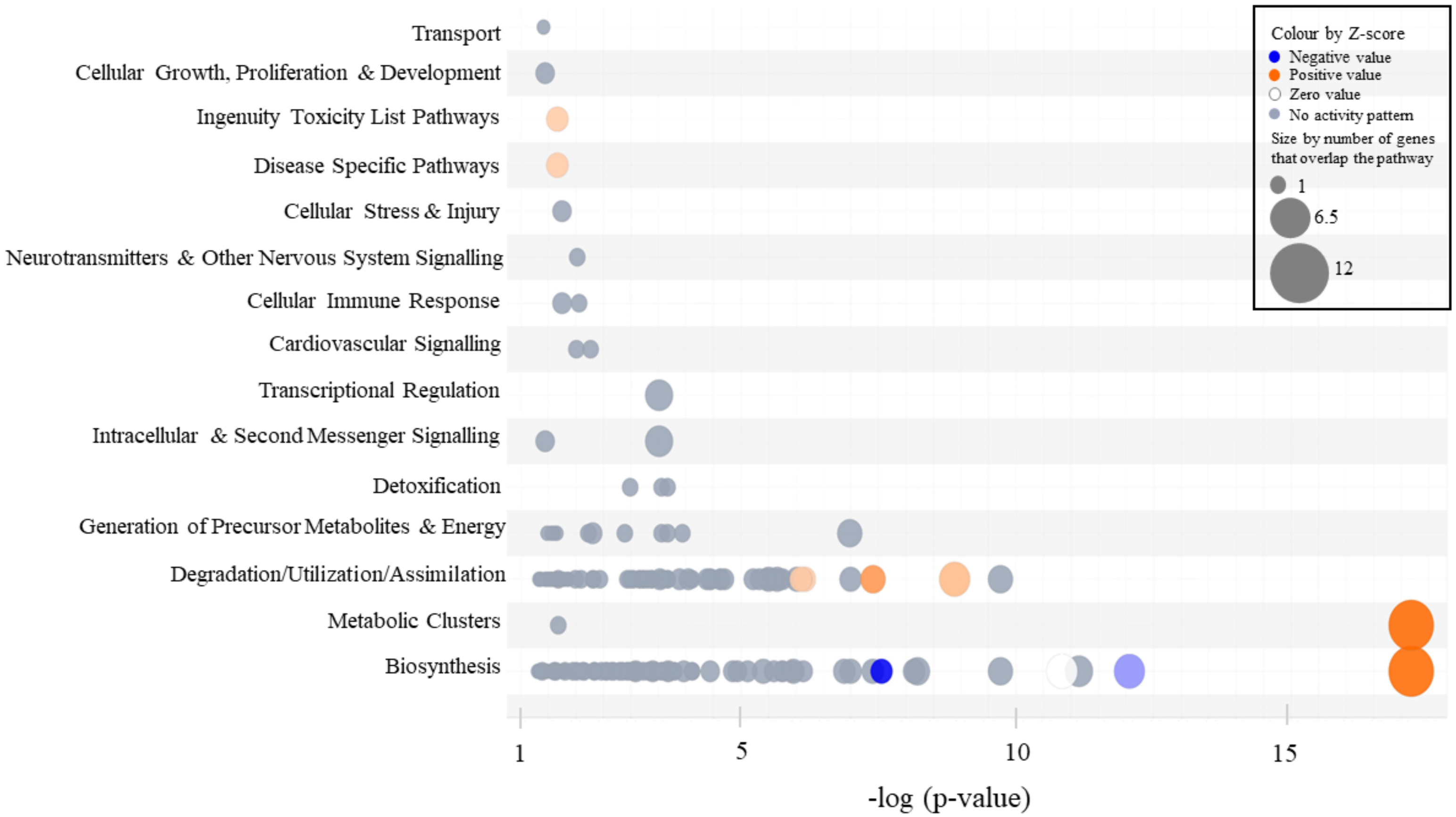

Figure 5.14: Canonical pathways affected in mild VSCM caused by R38H. Bubble size becomes larger with increasing number of overlapping genes in pathway. Z scores displayed by colour as shown in legend. P-value calculated by IPA through Fisher-exact test with Benjamini-Hochberg multiple-testing correction.

Furthermore, no other canonical pathways significantly impacted all *ACTG2* associated VSCM mutations. However, for *PIEZO1* associated VSCM, the disease-specific pathways were also significantly affected with further investigations revealing that *PIEZO1*-VSCM causes mitochondrial dysfunction. Figure 5.15a reported a prediction of the genes involved in causing mitochondrial dysregulation, given the obtained metabolic profile of *PIEZO1*-VSCM cells.

Figure 5.15b showed dopamine, glutathione, nicotinamide adenine dinucleotide (NAD+), palmitic acid, and succinic acid are the key molecules affected in the pathway, with the down regulation of all but glutathione which was upregulated. A detailed version of Figure 5.15 can be found in the appendix as Figure 7.1.

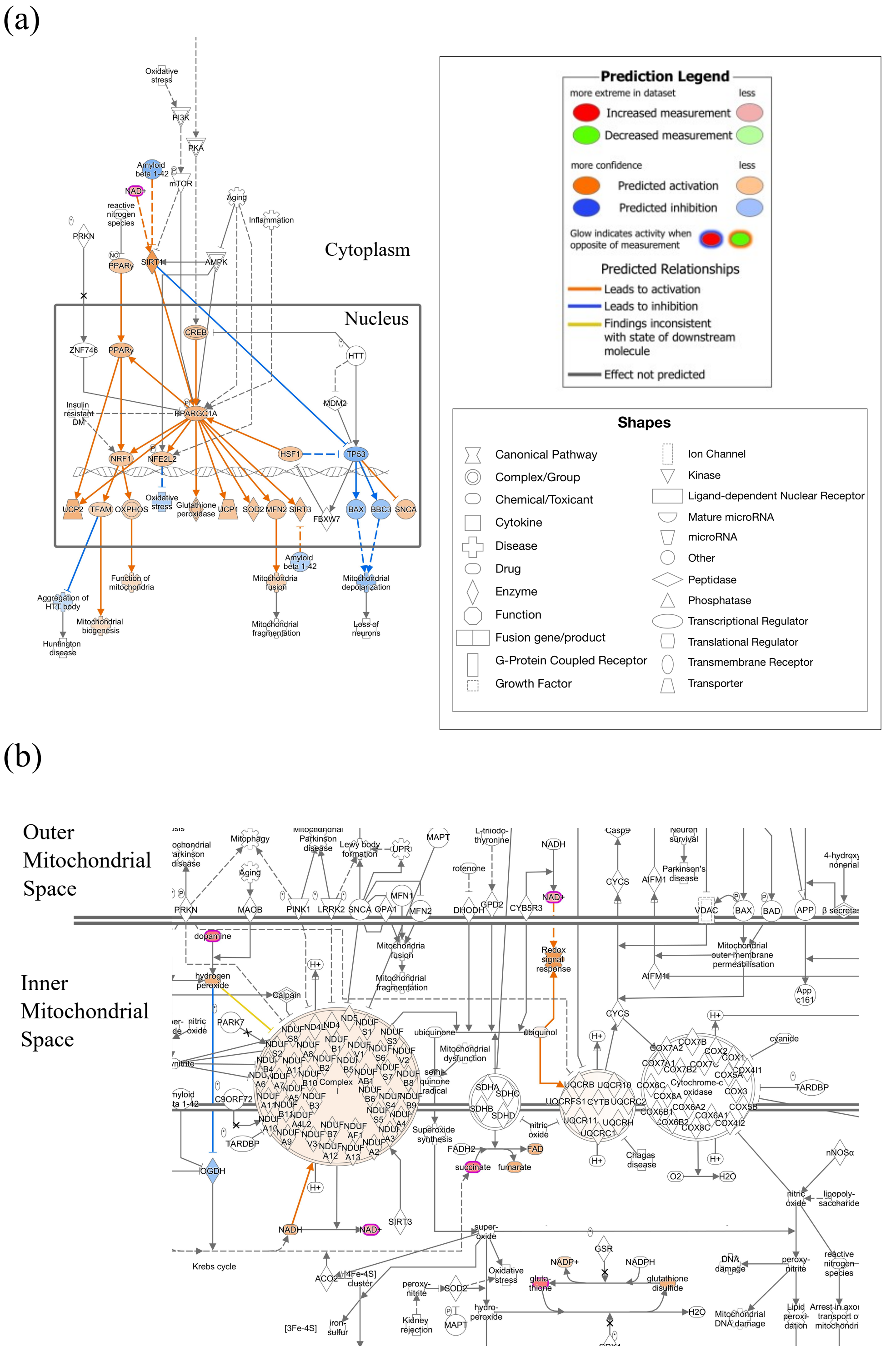

Figure 5.15: Piezo1 mutations cause mitochondrial dysfunction. Map shows prediction of mitochondrial pathways using analysis carried out on Qiagen IPA software with fold-change values. Highlighted in orange the predicted activation and in blue the predicted inhibition. Outline of pathways causing mitochondrial dysregulation in (a) nucleus (b) mitochondria.

5.3.6 EGFR network pathway is dysregulated in VSCM

Following on from canonical pathway analysis, networks involved in *PIEZO1* associated VSCM and all *ACTG2* associated VSCM cells were investigated. The epidermal growth factor receptor (EGFR) network was the top network mapped by Qiagen IPA software for *PIEZO1*-VSCM cells. This network was also significantly affected in all HDF cells. Figure 5.16a illustrated that EGFR network was predicted to be inhibited in *PIEZO1*-VSCM. However, Figure 5.16b depicted that the EGFR network was predicted to be activated in *ACTG2*-VSCM cells. Here, a representative map of the mild form of *ACTG2*-VSCM is shown and maps of the severe forms of *ACTG2*-VSCM can be found in the appendix as part of Figure 7.2.

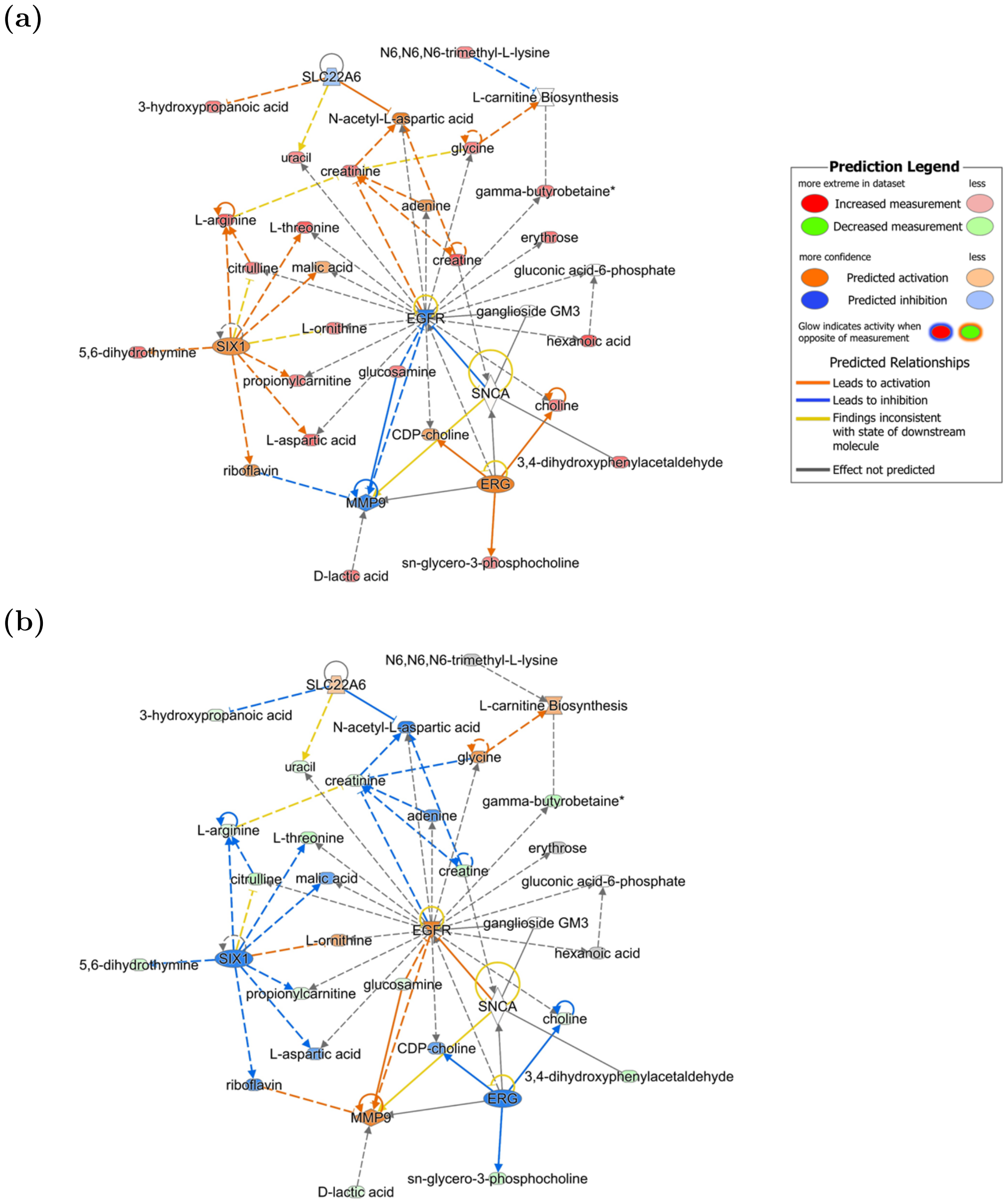

Figure 5.16: EGRF signalling network pathway is affected in VSCM. Maps show prediction of EGFR network pathway using comparison analysis carried out on Qiagen IPA software using fold-change values (a) EGFR network for *PIEZO1* associated VSCM (b) Representative EGFR network for *ACTG2* associated VSCM.

5.3.7 Calcium network is upregulated in *PIEZO1*-VSCM

The calcium network was the second most affected in *PIEZO1* associated VSCM cells. Qiagen IPA software used fold change values in metabolites to predict the activation of pathways in the network. From figure 5.17, it was clear that there was an upregulation of Ca^{2+}.

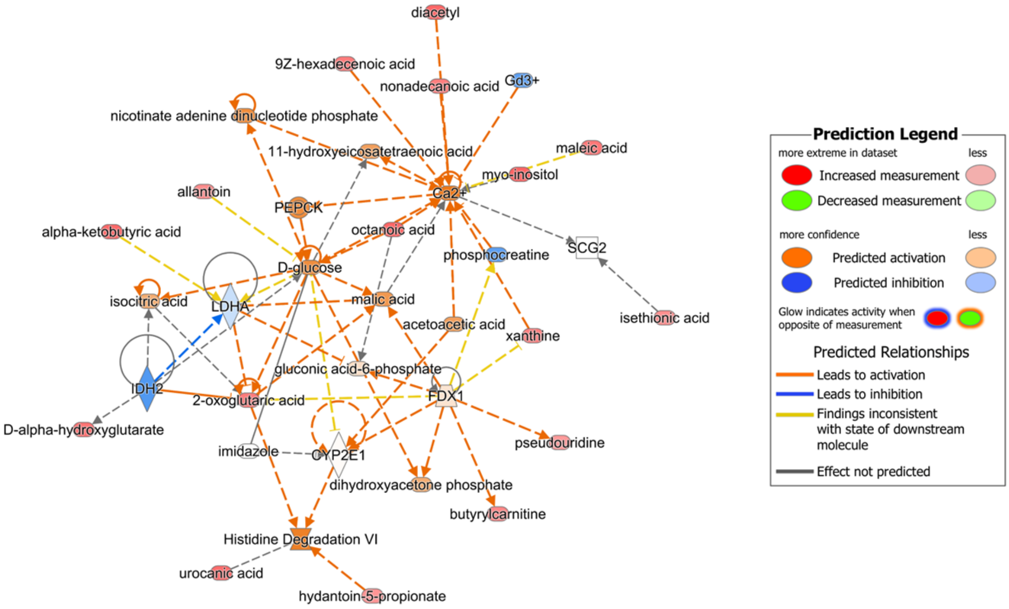

Figure 5.17: Calcium network pathway is affected in *PIEZO1* associated VSCM cells. Map shows prediction of calcium network pathway using analysis carried out on Qiagen IPA software with fold-change values.

In *ACTG2*-VSCM, mild VSCM caused by variant R38H and severe VSCM caused by variant R257C (sample S1) showed down regulation of Ca^{2+}. This was illustrated by a representative network in Figure 5.18a and the second map can be found in the appendix as Figure 7.3. The other severe VSCM sample, S2, showed upregulation of Ca^{2+}, comparable to *PIEZO1*-VSCM. However, not all metabolites in the network were regulated similarly to the calcium network in *PIEZO1*-VSCM.

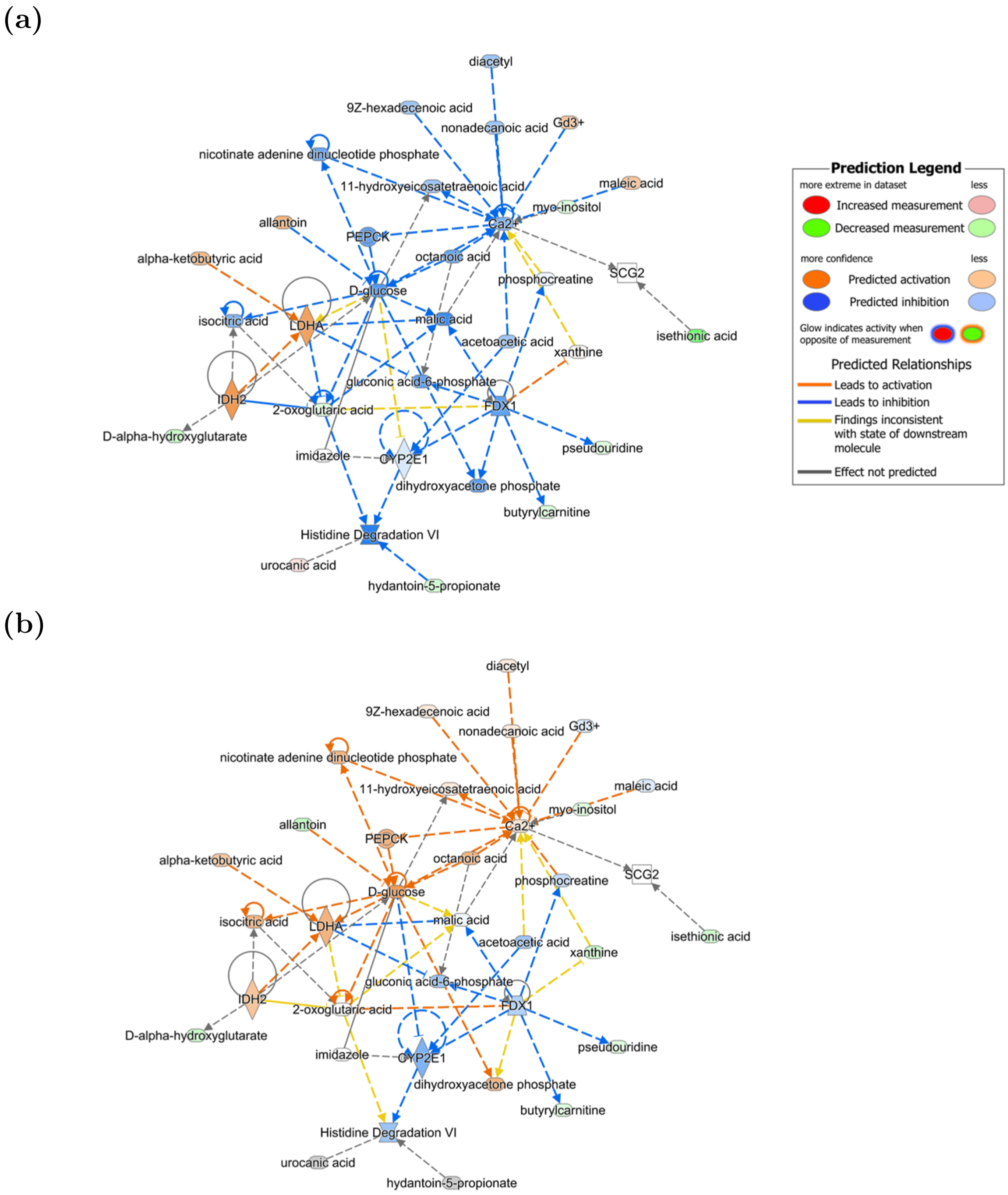

Figure 5.18: Calcium network pathway is affected in *ACTG2*-VSCM. Maps show prediction of calcium network pathway using comparison analysis carried out on Qiagen IPA software using fold-change values (a) Representative calcium network for *ACTG2*-VSCM showing downregulation of calcium. (b) Representative calcium network for *ACTG2*-VSCM showing upregulation of calcium.

5.4 Discussion

The role of the mechanosensitive ion channel, *PIEZO1*, in VSCM has not been previously explored. Recently, mutations in *PIEZO1* which cause VSCM were identified through whole exome sequencing. This chapter investigated the impact of the novel *PIEZO1* mutations by studying characteristics of *PIEZO1* VSCM cells; including morphology, YAP localisation, traction forces exerted, and the molecular clutch model. These characteristics were compared with healthy controls to establish differences between the healthy and disease state. *PIEZO1*-VSCM cells were also compared against *ACTG2*-VSCM cells in order to determine if cells were comparable considering patients present with similar symptoms. Moreover, the metabolic profiles of *PIEZO1*-VSCM, and *ACTG2*-VSCM cells in relation to healthy controls were analysed to determine whether biochemical differences were present between control, *ACTG2* associated VSCM and *PIEZO1* associated VSCM cells.

5.4.1 Morphology of *PIEZO1* associated VSCM

PIEZO1 associated VSCM cells displayed an opposing phenotype to *ACTG2*. From Figure 5.2 it was clear that *PIEZO1*-VSCM cells had a larger surface area compared to control and *ACTG2*-VSCM. Furthermore, *PIEZO1*-VSCM cells has a larger nuclear area compared to *ACTG2*-VSCM cells. These results were not observed in Chapter 4, Figure 4.5, where *ACTG2*-VSCM cells had a similar surface area and nuclear area to control cells. Furthermore, the significant differences observed in the major axis length of *PIEZO1* mutant cells versus control was similar to those seen between *ACTG2*-VSCM and control cells. The minor axis length of *PIEZO1*-VSCM cells was also longer compared to control and *ACTG2* cells. Additionally, *PIEZO1* cells had similar Haralick entropy and contrast values to control cells implying the actin cytoskeleton in *PIEZO1*-VSCM cells was variable in actin fibre density and had a more random fibre organisation. However, this again was opposite to the uniform and homogenous observed in *ACTG2* associated VSCM cells, as seen in Figures 4.7 and 5.3.

5.4.2 Mechanotransduction in *PIEZO1* associated VSCM

Figure 5.5, showed *PIEZO1*-VSCM cells had significantly increased YAP nuclear localisation and exerted greater forces compared to control cells and *ACTG2*-VSCM cells. Furthermore, the trend for YAP localisation in comparison to control cells was similar in both VSCM cell types. However, *PIEZO1*-VSCM cells had significantly higher levels of YAP nuclear localisation than control cells versus *ACTG2*-VSCM cells which had lower levels of YAP nuclear translocation compared to controls. This implied *PIEZO1* associated VSCM has different mechanical properties than *ACTG2* associated VSCM. At the time of this thesis, no known work had been carried out on VSCM and Piezo1 but studies had shown that *PIEZO1* plays a key role in regulating YAP activity [167, 168]. Additionally, work by Pathak's group on *PIEZO1* using human neural stem/progenitor cells (hNSPC) outlined that YAP nuclear localisation decreased with *PIEZO1* knockdown [169]. Since, the work in this thesis demonstrated YAP nuclear localisation has an almost 10 fold increase compared to healthy controls, it would implied *PIEZO1* channel was activated in *PIEZO1*-VSCM cells. Moreover, the traction forces exerted by *PIEZO1* cells on PDMS micropillar substrate were greater than forces exerted by controls. Further work by Pathak's group showed traction forces caused Ca^{2+} flickers which were locally confined to areas containing force exerting focal adhesions and implied channel activation. This in turn caused further generation of inside force and thus created a feedback loop [170].

5.4.3 Molecular clutch mechanism in *PIEZO1*-VSCM

Differences were observed in the molecular clutch mechanism in *ACTG2* associated VSCM cells, as outlined in Chapter 4. Therefore, in this chapter, the molecular clutch was investigated in *PIEZO1*-VSCM cells to determine whether *PIEZO1* mutant cells behaved similarly to *ACTG2*-VSCM cells. From Figure 5.8, it was seen that actin retrograde flow speed decreased in *PIEZO1*-VSCM cells in comparison to control cells whilst *ACTG2*-VSCM increased in actin flow compared to control. This indicated *PIEZO1* associated VSCM results in reduced actin polymerisation compared to healthy control and *ACTG2* associated VSCM. In VSCM, different disease-causing mutations have been shown to increase and decrease actin polymerisation [18, 35].

When analysing the focal adhesions, Figure 5.8 highlighted that focal adhesion number and length increased in *PIEZO1* associated VSCM cells compared to control cells. Whereas, focal adhesion length was shorter in *ACTG2*-VSCM than in control cells, again illustrating the cellular differences present between VSCM caused by *PIEZO1* mutations and that from *ACTG2* mutations. Numerous studies have demonstrated that *PIEZO1* activation is involved in the maturation and turnover of focal adhesions [171–173].

The final molecular clutch component examined was cell migration speed. Figure 5.8 showed migration speed was decreased in *PIEZO1*-VSCM but increased in *ACTG2*-VSCM. The decreased migration speed observed in *PIEZO1* cells differed from findings from *ACTG2*-VSCM carried out in Chapter 4 and in the field [59, 82]. Additionally, studies on cancer have shown that *PIEZO1* channel activation promotes YAP nuclear translocation which correlates with increased migration [174–176]. However, in this chapter, decreased migration was observed alongside increased YAP translocation. This can be due to other biochemical factors that are impacting migration speed outwith the mechanical cues. This is discussed in more detail below with the metabolomics results.

5.4.4 Metabolomic characterisation

After mechanical characterisation of *PIEZO1*, the metabolic profiles of *PIEZO1* associated VSCM and *ACTG2* associated VSCM was studied in comparison to healthy control cells. At the time of this thesis, metabolomics had not been employed to investigate VSCM had not been analysed therefore comments can not be put in context of the wider field. This is likely due to the limitations in acquiring patient samples coupled with the resource constraints associated with studying a rare disease.

The work carried out in this thesis indicated that *PIEZO1*-VSCM cells have completely different up/down regulation of metabolites compared to control cells. *ACTG2* associated VSCM cells also differed from control cells in their up/down regulation of metabolites but did so to a lesser degree. Moreover, there was variation between the different *ACTG2* samples, including between the two samples from patients with severe forms of VSCM, implying there was heterogeneity within *ACTG2*-VSCM metabolism. *PIEZO1*-VSCM and *ACTG2*-VSCM cells were analysed separately against the controls to minimise the dominance of the *PIEZO1*-VSCM cells from skewing the results.

Figure 5.10 illustrated that all VSCM associated cells form isolated cluster distinct from healthy control cells. There were significant differences in the metabolic profiles between *PIEZO1* associated VSCM and control groups as highlighted by the two groups clustering at opposite ends along PC1, which represented a high percentage of variance. Furthermore, there are differences between *ACTG2* associated VSCM and controls, though these appear less stark compared to that of *PIEZO1*-VSCM. When analysing the pathways affected in VSCM, as shown in Figures 5.11 to 5.14, there were numerous highly significant pathways involved which highlights the multifaceted nature of the disease. In depth pathway analysis, using IPA, revealed that mitochondrial dysfunction occurs in *PIEZO1*-VSCM which is not observed in all *ACTG2*-VSCM samples. IPA identifies the most significantly affected pathways using P-values and is then able to predict the expected activity pattern of the pathways.

Currently, not much is known about mitochondrial dysfunction in VSCM but problems with mitochondrial function are consistent with the activation of *PIEZO1*. When *PIEZO1* is activated, there is an influx of Ca^{2+} which enhances mitochondrial activity by increasing cyclic adenosine monophosphate that in turn has a role in increasing oxidative phosphorylation. This results in the increase of reactive oxygen species and can ultimately lead to mitochondrial dysfunction [177]. Work carried out by Liu *et al.,* found *PIEZO1* was over expressed in Crohn's disease, another gastrointestinal disorder. Here, *PIEZO1* activation resulted in Ca^{2+}

influx, increasing reactive oxygen species and ultimately causing mitochondrial dysfunction [166]. Furthermore, Piezo1 upregulation has been reported to cause mitochondrial dysfunction in vascular smooth muscle cells and intervertebral disc degeneration [178, 179]. These studies highlight the importance of *PIEZO1* in mitochondrial homeostasis. Therefore, it is interesting to see that the metabolomic analysis carried out in this chapter has also highlighted mitochondrial dysfunction in *PIEZO1*-VSCM cells.

During network analysis the EGFR network pathway was predicted to be inhibited in *PIEZO1*-VSCM cells and activated in *ACTG2*-VSCM cells as depicted in Figure 5.16. EGFR is a transmembrane protein which plays a pivotal role in signalling and as a result greatly impacts numerous cellular activities such as growth and migration [180–182]. At the time of this thesis, there was no known published work investigating migration and VSCM in the context of EGFR. However, there was evidence that EGFR promoting cell migration in cancer studies [183, 184]. The dysregulation of EGFR was in line with the cell migration speeds observed in Chapters 4 and 5 which reported a reduction in speed for *PIEZO1*-VSCM and an increase for *ACTG2*-VSCM cells. Moreover, these results provided a hypothesis for the migration results discussed above that needs to be investigated more extensively using molecular biology techniques.

Additionally, the calcium network was predicted to be upregulated in *PIEZO1* associated VSCM which supported the YAP and focal adhesion findings presented in this chapter. However, the *PIEZO1* mutation causing Prune-belly syndrome was identified as loss of function. Amado and colleagues used electrophysiology and a calcium flux assay to evaluate *PIEZO1* channel function [160]. Since Prune-belly syndrome also affects the contractile phenotype of smooth muscle cells, similar to VSCM, it is worth considering that the Piezo1-VSCM mutation studied in this chapter may also be loss of function [15]. In that case, the YAP findings presented in this chapter should be further investigated by looking into the Wingless integrated (Wnt) and Hippo pathways. These pathways act as a bridge between mechanical stimulus and YAP activation [185, 186]. Thus, further work exploring the Wnt and Hippo pathways may provide further insights into understanding *PIEZO1*-VSCM. Additionally, quantification of the calcium levels in Piezo1 cells compared to control cells need to be carried out as it would be beneficial in contextualising the results presented in this chapter. The next steps leading on from this thesis will be further discussed in the Chapter 6, section 6.6.

Overall, this chapter aimed to understand the cellular phenotype of VSCM caused by the novel Piezo1 mutation identified by the Sant'Orsola - Malpighi Polyclinic, Bologna, Italy. The findings from this chapter have been summarised with the schematic illustrated in Figure 5.19.

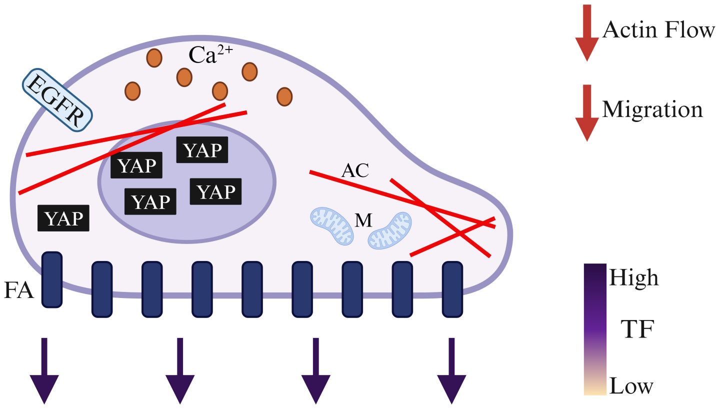

Figure 5.19: Characteristics of *PIEZO1* associated VSCM. Schematic depicts a Piezo1 associated VSCM cell with increased YAP nuclear translocation, mitochondrial dysfunction (M), increased intracellular calcium (Ca^{2+}), and dynamic and varied actin fibres (AC). Actin retrograde flow and migration speed are reduced, as highlighted by red arrows. The high traction forces (TF) exerted by the cell are illustrated with down arrows at the bottom of the cell. Image created with BioRender.com

5.5 Conclusion

A novel biallelic missense *PIEZO1* mutations (S1814F and P2230L) was identified in two sisters diagnosed with VSCM. Cell morphology, mechanotransduction, and the molecular clutch mechanism was analysed in mutant cells in order to determine whether they differed from control and *ACTG2*-VSCM. *PIEZO1*-VSCM cells had significant differences in mechanical characteristics from control cells including an increase in: YAP translocation, traction force exerted, as well as the length and number of focal adhesions. Additionally, there was a decrease in actin retrograde flow speed and thus actin polymerisation. These results indicated that the *PIEZO1* mutation severely impacts the function of the channel. This is supported by the metabolic profile of *PIEZO1* cells which highlighted regulation of Ca^{2+} but still further work needs to be carried out to quantify Piezo1 channel activation in VSCM associated *PIEZO1* mutant cells. Moreover, as a whole, *PIEZO1*-VSCM cells displayed opposite characteristics to *ACTG2* cells. This is a crucial statement when attempting to understand the *PIEZO1* mutation as although VSCM presents similarly in individuals with the *PIEZO1* mutation and *ACTG2* mutations, there are key differences at a cellular level which need to be taken into account as different methods will need to be explored for diagnostic/treatment purposes.

Moreover, the metabolic profiles were also investigated in control and all VSCM associated cells. Specific and pronounced differences were seen in the metabolomes of *PIEZO1*-VSCM and *ACTG2*-VSCM versus control cells which provided insights into possible metabolic pathways that are altered in VSCM. This further highlighted the fundamental differences between the two cell types associated with VSCM.

Furthermore, when exploring disease specific canonical pathways, mitochondrial dysfunction in *PIEZO1*-VSCM cells was found to be impacted which should be explored biochemically in order to determine the impact this has on VSCM. The EGFR network was also significantly affected in *PIEZO1* and *ACTG2* VSCM. This pathway should also be further investigated since it provides a biochemical explanation as to why migration is altered in the direction that it is, in VSCM, despite the mechanical data from traction force and actin retrograde flow indicating that migration should be altered in the opposite direction. Therefore, a biochemical investigation into the EGFR pathway is vital for understanding the disease mechanism, determining if migration can be a biomarker for VSCM, and also aiding in the identification of a potential therapeutic target.

6 | Conclusion & Outlook

The primary aim of this project was to gain a deeper understanding on VSCM from a morpho-mechanical and molecular perspective. In this project, *ACTG2* variants causing severe (R257C) and mild (R38H) forms of VSCM, as well as novel *PIEZO1* mutations associated with VSCM were investigated.

6.1 YAP nuclear localisation

YAP nuclear localisation was assessed to determine if YAP translocation was affected due to the decreased intestinal contractility phenotype associated with VSCM. Prior to this thesis, it had been hypothesised by Heuckeroth's lab that YAP/TAZ localisation would be increased in VSCM due to changes in the cells mechanical properties caused by intestinal stiffening [63]. Chapter 3 shows YAP nuclear localisation was greater in *ACTG2* associated VSCM cells compared to healthy controls, which was consistent with Heuckeroth's hypothesis. At the time of this thesis, the work shown here was the only analysis of YAP localisation in VSCM. This opens up a biochemical avenue that can be further explored in VSCM pathogenesis. Specifically, YAP can act as biomarker for VSCM but the development of an assay based on YAP will need much work. This will be further discussed below in section 6.6.

6.2 Traction forces as a biomarker

Currently, VSCM diagnosis is often delayed/misdiagnosed which has resulted in poor outcomes and no available treatment options as a result there is a need for disease biomarkers. In Chapter 3 the use of forces exerted by cells as a potential biomarker for VSCM was explored with PDMS micropillar arrays serving as a platform to measure traction forces. Quantification showed *ACTG2* associated VSCM cells exerted significantly lower traction forces compared with healthy controls and highlighted the potential of a force based assay for VSCM. There have been previous attempts to utilise a force based assay for VSCM diagnosis/drug screening. However, although successful in studying cellular forces, the assay had limited use in a clinical and research setting due to the expertise required to use such an assay [82]. A more extensive discussion on this can be found in Chapter 3, section 3.4. Overall, the work presented in this thesis demonstrated that PDMS micropillar arrays present as a useful platform to not only measure traction forces in *ACTG2*-VSCM but also can extended beyond *ACTG2*-mutations to include other VSCM causing mutations. This is possible as due to the ease of using micropillar arrays and the robust nature of the platform. Although micropillar fabrication requires state of the art facilities, Professor Gadegaard's team is moving towards commercialisation of the platform, and thus eliminating the difficult manufacturing component of the assay, making the platform particularly useful for drug screening purposes.

6.3 Morpho-mechanical characteristics

Chapter 4 focused on understanding the morpho-mechanical features of VSCM caused by *ACTG2* variants. Initially, cell morphology was investigated to determine phenotypic variations in VSCM. Analysis highlighted that VSCM did not impact cell and nuclear area. However, severe forms of *ACTG2* associated VSCM (R257C) resulted in cells which had a significantly longer major axis length and higher values of eccentricity suggesting VSCM cells are more elongated than control cells. Moreover, *ACTG2*-VSCM cells had lower values for Haralick textural features of contrast and entropy implying that actin fibres in VSCM caused by *ACTG2* have a more homogeneous distribution, with a regular and structured pattern. In particular, this highlighted that *ACTG2*-VSCM cells had less variability in actin fibre density and organisation compared to healthy controls. Disruptions in actin polymerisation would cause the observed homogeneous actin cytoskeleton organisation. Additionally, a more homogeneous actin network would be less capable of rapid reorganisation, which is necessary for effective force generation. This hypothesis is strengthened by the lower traction forces exerted by *ACTG2* associated VSCM cells, as outlined by the work carried out on PDMS micropillar arrays in Chapter 3.

Next, the molecular clutch mechanism was investigated in VSCM. Actin retrograde flow speed was increased indicating actin polymerisation is accelerated in *ACTG2* associated VSCM. Moreover, focal adhesions were shorter in length and greater in number, highlighting that *ACTG2*-VSCM disrupts stable focal adhesion formation. Taken together, this illustrates that the molecular clutch is less engaged in VSCM which is corroborated by the reduced traction force results. Importantly, the characterisation of the morpho-mechanical features of *ACTG2* associated VSCM highlights that VSCM presents as a mechanical disorder.

6.4 Migration as a biomarker

Migration was found to have increased in *ACTG2*-VSCM. This highlighted the role of cell migration as a physical disease biomarker. The data was obtained using the HoloMonitor which was label-free and thus mitigated problems associated with traditional cell migration tracking using probes and dyes. However, the migration findings opposed the prediction of the molecular clutch model that migration would be slower in *ACTG2*-VSCM, as presented and discussed in Chapter 4. Nonetheless, the data shown in this thesis, is in line with current viewpoint that cells from VSCM caused by *ACTG2* variants are more migratory than healthy cells. Overall, it is important to highlight that retrograde flow (the basis of the molecular clutch model) is produced both by cytoskeletal assembly and contractility. If either is impaired, it could result in apparently contradictory results.

Furthermore, the metabolomics analysis carried out in Chapter 5 strengthened the migratory data reported in this thesis, by reporting the predicted activation of the EGFR network pathway in *ACTG2*-VSCM. Thus, overall, the migration analysis undertaken in this thesis not only demonstrated that migration is a physical biomarker for *ACTG2*-VSCM which can be tracked in a label-free manner but also illustrated that there is a mechanical and, previously unexplored, biochemical component to the altered cell migration observed.

6.5 ***PIEZO1***-VSCM versus ***ACTG2***-VSCM

Novel mutations in *PIEZO1* causing VSCM were discovered in Sant'Orsola-Malpighi Polyclinic, Bologna, Italy. In this thesis the morpho-mechanical characteristics were explored to establish whether this VSCM causing mutation, where individuals presented with similar symptoms to *ACTG2*-VSCM, resulted in a similar cellular phenotype. Chapter 5 focused on exploring *PIEZO1* associated VSCM in comparison to *ACTG2* associated VSCM and healthy controls, and showed that *PIEZO1*-VSCM differed from *ACTG2*-VSCM.

Morphological analysis on *PIEZO1*-VSCM revealed that cells were larger in area and had a longer major axis length compared to *ACTG2*-VSCM and healthy control cells. Furthermore, in Chapter 4, *ACTG2* associated VSCM cells were found to have greater values for cell eccentricity implying *ACTG2*-VSCM cells are more elongated than control cells, which is not seen in *PIEZO1*-VSCM cells. Additionally, Haralick textural feature analysis showed that the actin cytoskeleton homogeneity and order in *PIEZO1* associated VSCM was similar to healthy controls but differed from *ACTG2*-VSCM. Together, this highlighted that, morphologically, VSCM caused by *PIEZO1* mutations displayed similar characteristics to the healthy phenotype than to *ACTG2*-VSCM.

Additionally, *PIEZO1*-VSCM cells had higher YAP nuclear localisation and exerted greater traction forces compared to healthy control cells and *ACTG2*-VSCM. This data further reinforces the notion that *PIEZO1*-VSCM cells have different characteristics to *ACTG2*-VSCM. However, in terms of YAP, *PIEZO1*-VSCM does not result in an opposing phenotype but rather a more extreme form of the phenotype displayed by *ACTG2*-VSCM.

Finally, the molecular clutch model was investigated. *PIEZO1* associated VSCM cells displayed slower actin retrograde flow speed and had longer focal adhesion length than healthy control cells and *ACTG2*-VSCM cells. Migration speed was also slower in *PIEZO1*-mutant cells compared to control and *ACTG2* associated VSCM cells. This again confirms that VSCM caused by *PIEZO1* displays different cellular features than VSCM caused by *ACTG2* variants. In this instance *PIEZO1*-VSCM also differed from the healthy control.

Chapter 5 also investigated the metabolomic profiles of VSCM caused by *ACTG2* mutations and by *PIEZO1* mutations. This was to determine whether the morpho-mechanical differences seen between *PIEZO1* associated VSCM and *ACTG2* associated VSCM were present at a biochemical level. *PIEZO1*-VSCM had an opposite metabolic profile compared to *ACTG2*-VSCM. This was particularly evident in the up/down regulation of metabolites and the activation of pathways.

Overall, the morpho-mechanical and metabolomic data showed that *PIEZO1*-VSCM either displays an amplified characteristic of, or differs completely from *ACTG2*-VSCM. Importantly, this revealed that the cellular characteristics between VSCM caused by *PIEZO1* mutation and VSCM caused by *ACTG2* mutations appear to differ significantly despite individuals exhibiting similar symptoms.

6.6 Perspective and future work

In this thesis, primary human dermal fibroblasts were used, however, a more biologically relevant model would be enteric smooth muscle cells. Nonetheless, dermal fibroblasts were chosen as they are less invasive to the patient when collecting a sample compared to extracting enteric smooth muscle cells which would require unnecessary major surgery and could cause further intestinal complications. Furthermore, previous work carried out with Viti and colleagues, as a precursor to this project, demonstrated through both the Human Protein Atlas (HPA) database and quantitative Polymerase Chain Reaction (qPCR) analysis that the *ACTG2* gene was found to be expressed in dermal fibroblasts [82]. Future work on the project could consider the establishment of a protocol for the differentiation of fibroblasts to smooth muscle cells as outlined by Hirai and colleagues [187], from which further investigation into VSCM can be carried out.

Moreover, there was a limited number of samples analysed in this work for *ACTG2*-VSCM, *PIEZO1*-VSCM, *LIG3*-CIPO, and HSCR. As a result, replicates were not available which represents an overall limit for the work. Additional primary samples would have been ideal but as with all work on rare diseases, samples are difficult to acquire due to the small pool of patients and for VSCM there is an added layer of complexity due to late/misdiagnosis as discussed in Chapter 1, section 1.1. Further work should be carried out on additional samples, particularly, from individuals with severe (R257C) and mild (R38H) VSCM causing variants, as well as other *ACTG2* variants (as illustrated in Chapter 1, Figure 1.1) causing VSCM which have not been explored. This would be essential in confirming and validating the findings of this thesis but can only be carried out when more samples become available.

Additionally, a common difficulty when working with primary cells is the limited time that cells can be cultured. To overcome this, primary cells can be immortalised. This has been successfully achieved through the use of 'MyoLine', a platform from the Institute of Myology in Paris, France, where myoblasts and dermal fibroblasts have been successfully immortalised and studied [188–191]. With the services provided by the Institute of Myology, work would not be restricted by the limited growth potential associated with primary cell culture.

Furthermore, this thesis highlighted that mechanical characteristics such as traction forces, migration, and actin retrograde flow are impacted by VSCM. Thus, the next steps would be to investigate the extent to which mechanics impacts VSCM. This can be done through the use of molecules that are able to mechanically affect cells, for example Jasplakinolide, which can stabilise actin filaments. In theory by stabilising actin filaments, polymerisation which was found to be impacted by VSCM would also be stabilised and the cellular phenotype should revert to that similar to control cells. This can be implemented on the platforms and biomarkers already established in this thesis such as PDMS micropillars to test traction forces.

The data in this thesis was able to identify YAP nuclear localisation,traction forces and migration as potential biomarkers for VSCM. Further work needs to be carried out in order to develop assays which can be utilised for diagnostic and therapeutic purposes. For cell migration tracking, digital holography was used. This was carried out on the commercially available HoloMonitor microscope. However, increasing the number of cells able to be tracked would be valuable. This can be done by imaging with microscope that has a wider field of view which would require designing and engineering a holographic devise with analysis software which was not possible for this project due to the time constraints but lays the foundation for a subsequent project. Additionally, the PDMS micropillar platform can currently serve as an assay to measure traction forces between VSCM and healthy cells. The assay is suitable for clinical research rather than diagnostic purposes due to the specialised training and equipment required. Moreover, although the micropillars act as a robust platform to measure traction forces, to carry out data analysis requires specialised training which would not be readily available.

Therefore, future work would be to develop a software which can standardise and automate the analysis process. Furthermore, YAP emerged as a biomarker for VSCM. Much work is needed to further understand the extent to which nuclear YAP translocation is impacted in *ACTG2*-VSCM. This can include general YAP quantification through western blots as well as investigating a potential assay design - for example, an ELISA to quantify YAP would be a specific and robust method of measuring YAP. It would also be useful to explore a combined system where YAP staining could be carried out on cells seeded on micropillar arrays.

The EGFR pathway also provides a new avenue to investigate the altered migration pattern in VSCM. Therefore, future work should involve the investigation of EGFR through a biochemical and genetic approach. This could be done through confirming the activation state of EGFR via western blots, immunoprecipitation to determine protein interactors of EGFR impacted in VSCM, and knocking out or modifying specific genes in the EGFR signalling pathway by using CRISPR/Cas9 technology.

Additionally, further work needs to be carried out in order to fully understand the role of *PIEZO1* in VSCM. In this thesis, the differences between *PIEZO1*-VSCM and *ACTG2* was investigated and it was established that the VSCM caused by *PIEZO1* presents differently at a cellular level from the *ACTG2*. However, since *PIEZO1* is an ion channel, further work studying the activation of the channel needs to be carried out. This can be carried out using the fluid force microscopy (FluidFM) technique as reported by [192].

A final avenue to explore in understanding VSCM is analysing the role of mitochondrial dysfunction in VSCM. Metabolomic analysis in Chapter 5 has already highlighted mitochondrial dysfunction occurs in *PIEZO1*-VSCM. This should be further investigated by, for example, studying mitochondrial morphology and oxygen consumption rate in live cells.

Overall, in this project the morpho-mechanical and biochemical characteristics of *ACTG2* associated VSCM and *PIEZO1* associated VSCM were investigated. From this work cellular features such as traction forces exerted by cells and cell migration have emerged as key disease markers. Whilst, more work is needed, the findings presented in this thesis have added substantially to the understanding of VSCM. In particular, this project has been in able to characterise a novel *PIEZO1* mutation which results in VSCM and explore how VSCM caused by this mutation differs from the VSCM associated with the traditional *ACTG2* variant.

7 | Appendix

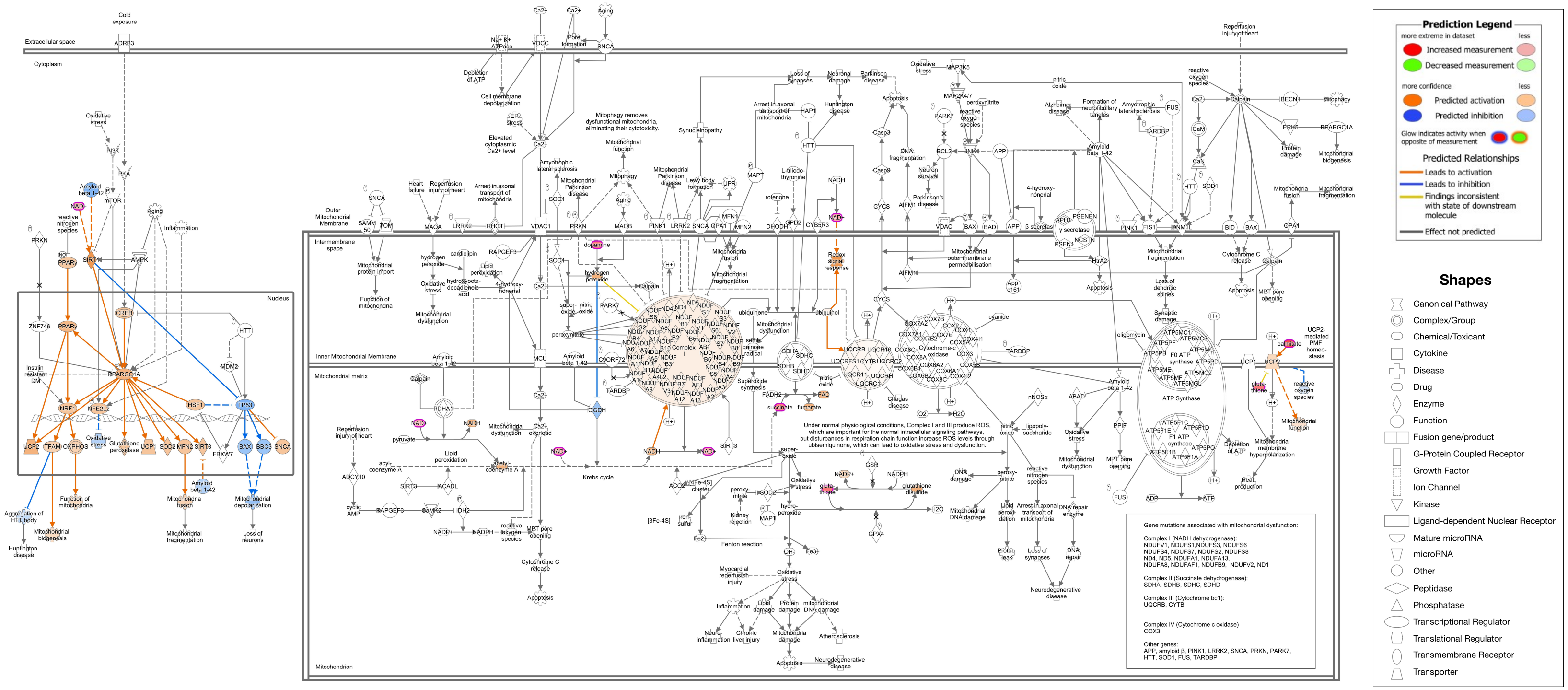

Figure 7.1: Mitochondrial dysfunction occurs in *PIEZO1* associated VSCM cells. Map shows prediction of EGFR network pathway using analysis carried out on Qiagen IPA software with fold-change values.

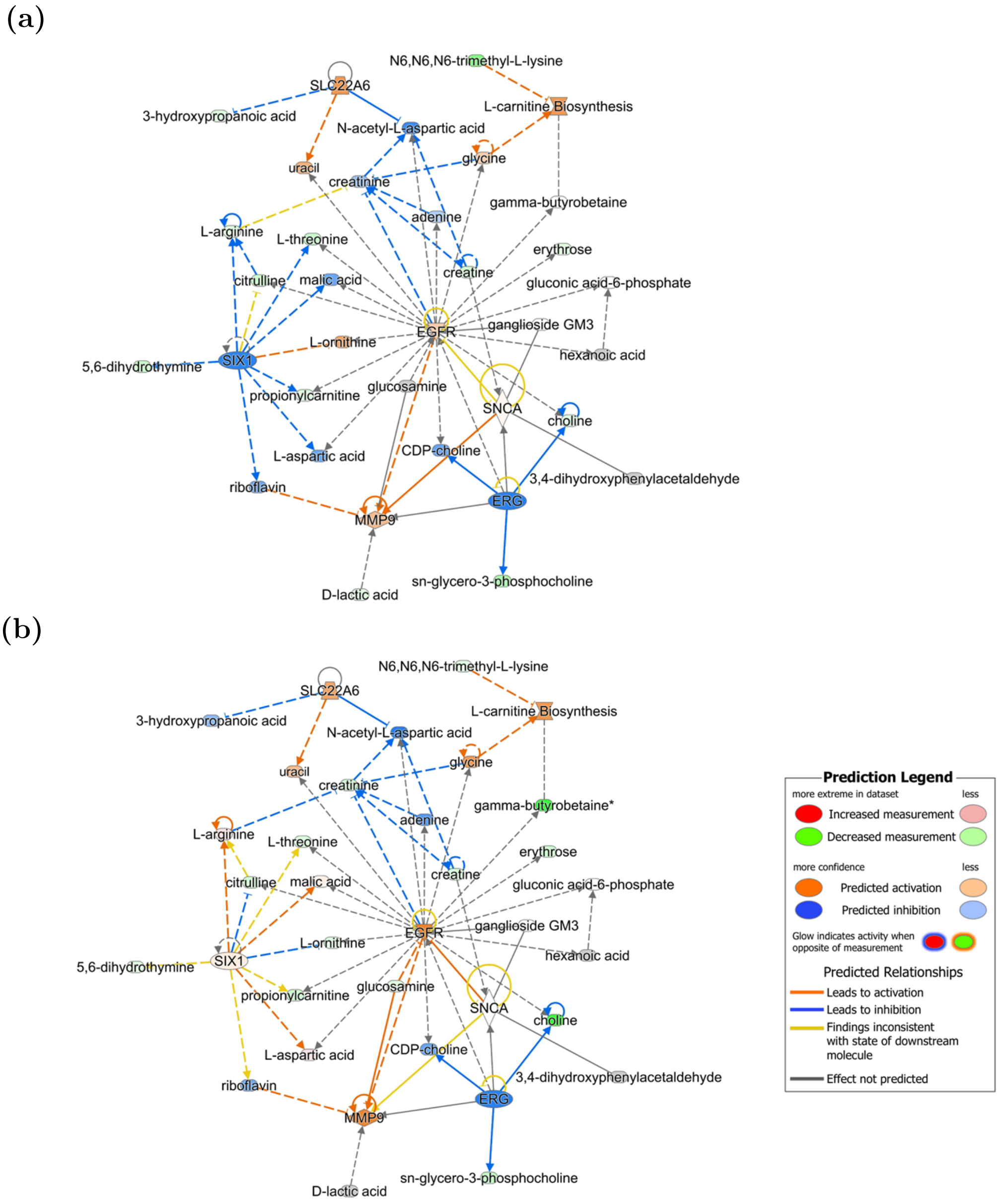

Figure 7.2: EGRF signalling pathway affected in ACTG2 associated VSCM. Maps show prediction of EGFR network pathway using comparison analysis carried out on Qiagen IPA software using fold-change values. (a) severe VSCM caused by severe ACTG2 associated VSCM (S1). (c) severe VSCM caused by severe ACTG2 associated VSCM (S2).

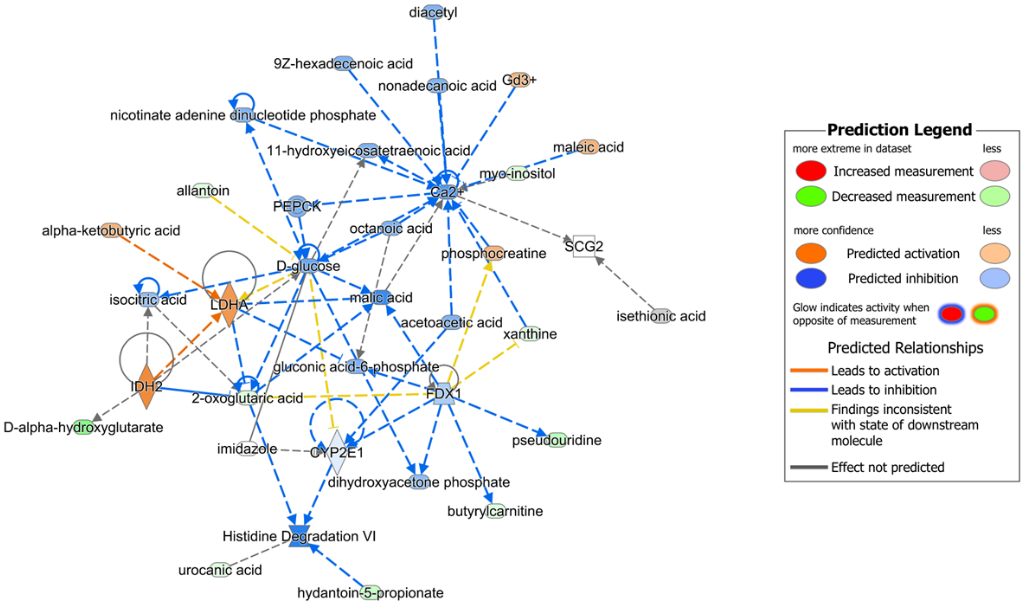

Figure 7.3: Calcium network pathway is affected in severe VSCM caused by *ACTG2* variant R38H (M). Maps show prediction of calcium network pathway using comparison analysis carried out on Qiagen IPA software using fold-change values.

Bibliography

[1] N. Thapar, E. Saliakellis, M. A. Benninga, O. Borrelli, J. Curry, C. Faure, R. De Giorgio, G. Gupte, C. H. Knowles, A. Staiano, et al. (2018). Paediatric intestinal pseudo-obstruction: evidence and consensus-based recommendations from an espghan-led expert group. *Journal of pediatric gastroenterology and nutrition*, 66(6):991–1019.

[2] J.-H. Gosemann and P. Puri (2011). Megacystis microcolon intestinal hypoperistalsis syndrome: systematic review of outcome. *Pediatric surgery international*, 27:1041–1046.

[3] T. J. Downes, M. S. Cheruvu, T. B. Karunaratne, R. De Giorgio, and A. D. Farmer (2018). Pathophysiology, diagnosis, and management of chronic intestinal pseudo-obstruction. *Journal of clinical gastroenterology*, 52(6):477–489.

[4] R. De Giorgio, R. F. Cogliandro, G. Barbara, R. Corinaldesi, and V. Stanghellini (2011). Chronic intestinal pseudo-obstruction: clinical features, diagnosis, and therapy. *Gastroenterology Clinics*, 40(4):787–807.

[5] A. M. Holland, A. C. Bon-Frauches, D. Keszthelyi, V. Melotte, and W. Boesmans (2021). The enteric nervous system in gastrointestinal disease etiology. *Cellular and Molecular Life Sciences*, 78(10):4713–4733.

[6] R. De Giorgio, G. Sarnelli, R. Corinaldesi, and V. Stanghellini (2004). Advances in our understanding of the pathology of chronic intestinal pseudo-obstruction. *Gut*, 53(11):1549–1552.

[7] A. Antonucci, L. Fronzoni, L. Cogliandro, R. F. Cogliandro, C. Caputo, R. De Giorgio, F. Pallotti, G. Barbara, R. Corinaldesi, and V. Stanghellini (2008). Chronic intestinal pseudo-obstruction. *World journal of gastroenterology: WJG*, 14(19):2953.

[8] H. J. Lehtonen, T. Sipponen, S. Tojkander, R. Karikoski, H. Järvinen, N. G. Laing, P. Lappalainen, L. A. Aaltonen, and S. Tuupanen (2012). Segregation of a missense variant in enteric smooth muscle actin γ-2 with autosomal dominant familial visceral myopathy. *Gastroenterology*, 143(6):1482–1491.

[9] C. Di Lorenzo and N. N. Youssef. Diagnosis and management of intestinal motility disorders. In *Seminars in pediatric surgery*, Volume 19, pages 50–58. Elsevier, (2010).

[10] A. L. M. dos Santos, R. W. A. Braga, H. B. K. Seidler, R. P. de Abreu Miranda, I. I. T. Salvador, and E. de Carvalho (2020). Pediatric intestinal pseudo-obstruction: Role of histopathology. *Journal of Pediatric Surgery Case Reports*, 57:101449.

[11] Ö. B. Türer, T. Soyer, H. Özen, U. E. Arslan, İ. Karnak, and F. C. Tanyel (2020). Challenges in management and prognosis of pediatric intestinal pseudo-obstruction. *The Turkish Journal of Gastroenterology*, 31(8):596.

[12] A. Diamanti, F. Fusaro, T. Caldaro, T. Capriati, M. Candusso, V. Nobili, and O. Borrelli (2019). Pediatric intestinal pseudo-obstruction: impact of neonatal and later onset on clinical and nutritional outcomes. *Journal of Pediatric Gastroenterology and Nutrition*, 69(2):212–217.

[13] C. Granata and P. Puri (1997). Megacystis-microcolon-intestinal hypoperistalsis syndrome. *Journal of pediatric gastroenterology and nutrition*, 25(1):12–19.

[14] P. Puri and M. Shinkai. Megacystis microcolon intestinal hypoperistalsis syndrome. In *Seminars in pediatric surgery*, Volume 14, pages 58–63. Elsevier, (2005).

[15] M. F. Wangler, C. Gonzaga-Jauregui, T. Gambin, S. Penney, T. Moss, A. Chopra, F. J. Probst, F. Xia, Y. Yang, S. Werlin, et al. (2014). Heterozygous de novo and inherited mutations in the smooth muscle actin (actg2) gene underlie megacystis-microcolon-intestinal hypoperistalsis syndrome. *PLoS genetics*, 10(3):e1004258.

[16] Z. Gonzalez and R. McCallum (2020). Small bowel dysmotility, pseudoobstruction, and functional correlation with histopathology: lessons learned. *Current Gastroenterology Reports*, 22:1–16.

[17] C. A. Moreno, K. Metze, E. A. Lomazi, D. R. Bertola, R. H. A. Barbosa, V. Cosentino, N. Sobreira, and D. P. Cavalcanti (2016). Visceral myopathy: Clinical and molecular survey of a cohort of seven new patients and state of

the art of overlapping phenotypes. *American Journal of Medical Genetics Part A*, 170(11):2965–2974.

[18] D. Halim, R. M. Hofstra, L. Signorile, R. M. Verdijk, C. S. van der Werf, Y. Sribudiani, R. W. Brouwer, W. F. van IJcken, N. Dahl, J. B. Verheij, et al. (2016). Actg2 variants impair actin polymerization in sporadic megacystis microcolon intestinal hypoperistalsis syndrome. *Human Molecular Genetics*, 25(3):571–583.

[19] F. Viti, R. De Giorgio, I. Ceccherini, A. Ahluwalia, M. M. Alves, C. Baldo, G. Baldussi, E. Bonora, O. Borrelli, L. Dall'Oglio, et al. (2023). Multidisciplinary insights from the first european forum on visceral myopathy 2022 meeting. *Digestive Diseases and Sciences*, 68(10):3857–3871.

[20] T. R. Huycke, B. M. Miller, H. K. Gill, N. L. Nerurkar, D. Sprinzak, L. Mahadevan, and C. J. Tabin (2019). Genetic and mechanical regulation of intestinal smooth muscle development. *Cell*, 179(1):90–105.

[21] Y. Tokita, H. Akiho, K. Nakamura, E. Ihara, and M. Yamamoto (2015). Contraction of gut smooth muscle cells assessed by fluorescence imaging. *Journal of pharmacological sciences*, 127(3):344–351.

[22] J. D. Huizinga, J.-H. Chen, Y. Fang Zhu, A. Pawelka, R. J. McGinn, B. L. Bardakjian, S. P. Parsons, W. A. Kunze, R. Y. Wu, P. Bercik, et al. (2014). The origin of segmentation motor activity in the intestine. *Nature communications*, 5(1):3326.

[23] S. L. Gabbard and B. E. Lacy (2013). Chronic intestinal pseudo-obstruction. *Nutrition in Clinical Practice*, 28(3):307–316.

[24] G. Di Nardo, C. Di Lorenzo, A. Lauro, V. Stanghellini, N. Thapar, T. Karunaratne, U. Volta, and R. De Giorgio (2017). Chronic intestinal pseudo-obstruction in children and adults: diagnosis and therapeutic options. *Neurogastroenterology & Motility*, 29(1):e12945.

[25] C. H. Knowles, R. De Giorgio, R. P. Kapur, E. Bruder, G. Farrugia, K. Geboes, M. D. Gershon, J. Hutson, G. Lindberg, J. E. Martin, et al. (2009). Gastrointestinal neuromuscular pathology: guidelines for histological techniques and reporting on behalf of the gastro 2009 international working group. *Acta neuropathologica*, 118:271–301.

[26] C.-Z. Zhu, H.-W. Zhao, H.-W. Lin, F. Wang, and Y.-X. Li (2020). Latest developments in chronic intestinal pseudo-obstruction. *World Journal of Clinical Cases*, 8(23):5852.

[27] N. Assia Batzir, P. Kishor Bhagwat, A. Larson, Z. Coban Akdemir, M. Bagłaj, L. Bofferding, K. B. Bosanko, S. Bouassida, B. Callewaert, A. Cannon, et al. (2020). Recurrent arginine substitutions in the actg2 gene are the primary driver of disease burden and severity in visceral myopathy. *Human mutation*, 41(3):641–654.

[28] A. Milunsky, C. Baldwin, X. Zhang, D. Primack, A. Curnow, and J. Milunsky (2017). Diagnosis of chronic intestinal pseudo-obstruction and megacystis by sequencing the actg2 gene. *Journal of pediatric gastroenterology and nutrition*, 65(4):384–387.

[29] Ø. L. Holla, G. Bock, Ø. L. Busk, and B. L. Isfoss (2014). Familial visceral myopathy diagnosed by exome sequencing of a patient with chronic intestinal pseudo-obstruction. *Endoscopy*, 46(06):533–537.

[30] W. Dong, C. Baldwin, J. Choi, J. M. Milunsky, J. Zhang, K. Bilguvar, R. P. Lifton, and A. Milunsky (2019). Identification of a dominant myh11 causal variant in chronic intestinal pseudo-obstruction: Results of whole-exome sequencing. *Clinical Genetics*, 96(5):473–477.

[31] W. Zhou, X. Liu, J. W. M. van Wijnbergen, L. Yuan, Y. Liu, C. Zhang, and W. Jia (2020). Identification of piezo1 as a potential prognostic marker in gliomas. *Scientific reports*, 10(1):16121.

[32] L. Sigurdsson, J. Reyes, S. Kocoshis, G. Mazariegos, K. Abu-Elmagd, J. Bueno, and C. Di Lorenzo (1999). Intestinal transplantation in children with chronic intestinal pseudo-obstruction. *Gut*, 45(4):570–574.

[33] A. Lauro, C. Zanfi, S. Pellegrini, F. Catena, M. Cescon, N. Cautero, V. Stanghellini, L. Pironi, and A. D. Pinna. Isolated intestinal transplant for chronic intestinal pseudo-obstruction in adults: long-term outcome. In *Transplantation Proceedings*, Volume 45, pages 3351–3355. Elsevier, (2013).

[34] L. Gu, C. Ding, H. Tian, B. Yang, X. Zhang, Y. Hua, Y. Zhu, J. Gong, W. Zhu, J. Li, et al. (2017). Serial frozen fecal microbiota transplantation in the treatment of chronic intestinal pseudo-obstruction: a preliminary study. *Journal of neurogastroenterology and motility*, 23(2):289.

[35] R. H. Ceron, F. A. Báez-Cruz, N. J. Palmer, P. J. Carman, M. Boczkowska, R. O. Heuckeroth, E. M. Ostap, and R. Dominguez (2024). Molecular mechanisms linking missense actg2 mutations to visceral myopathy. *Science Advances*, 10(22):eadn6615.

[36] I. Matera, M. Rusmini, Y. Guo, M. Lerone, J. Li, J. Zhang, M. Di Duca, P. Nozza, M. Mosconi, A. P. Prato, et al. (2016). Variants of the actg2 gene correlate with degree of severity and presence of megacystis in chronic intestinal pseudo-obstruction. *European Journal of Human Genetics*, 24(8):1211–1215.

[37] I. Matera, D. Bordo, M. Di Duca, M. Lerone, G. Santamaria, M. Pongiglione, A. Lezo, A. Diamanti, M. I. Spagnuolo, A. Pini Prato, et al. (2021). Novel actg2 variants disclose allelic heterogeneity and bi-allelic inheritance in pediatric chronic intestinal pseudo-obstruction. *Clinical Genetics*, 99(3):430–436.

[38] K. V. Schulze, N. A. Hanchard, and M. F. Wangler (2020). Biases in arginine codon usage correlate with genetic disease risk. *Genetics in Medicine*, 22(8):1407–1412.

[39] K. N. James, M. Lau, K. Shayan, J. Lenberg, R. Mardach, R. Ignacio, J. Halbach, L. Choi, S. Kumar, and K. A. Ellsworth (2021). Expanding the genotypic spectrum of actg2-related visceral myopathy. *Molecular Case Studies*, 7(3):a006085.

[40] M. Mori, A. R. Clause, K. Truxal, R. T. Hagelstrom, K. Manickam, S. G. Kaler, V. Prasad, J. Windster, M. M. Alves, and C. Di Lorenzo (2022). Autosomal recessive actg2-related visceral myopathy in brothers. *JPGN reports*, 3(4):e258.

[41] D. Monies, S. Maddirevula, W. Kurdi, M. H. Alanazy, H. Alkhalidi, M. Al-Owain, R. A. Sulaiman, E. Faqeih, E. Goljan, N. Ibrahim, et al. (2017). Autozygosity reveals recessive mutations and novel mechanisms in dominant genes: implications in variant interpretation. *Genetics in Medicine*, 19(10):1144–1150.

[42] H. Lee, S. Park, J.-T. Oh, H. M. Kim, S. Kim, and J.-S. Lee (2019). Oral pyridostigmine-responsive visceral myopathy with actg2 mutations: a case series. *Journal of Pediatric Gastroenterology and Nutrition*, 68(1):e16–e17.

[43] G. Ravenscroft, S. Pannell, G. O'Grady, R. Ong, H. Ee, F. Faiz, L. Marns, H. Goel, P. Kumarasinghe, E. Sollis, et al. (2018). Variants in actg 2 underlie a substantial number of australasian patients with primary chronic intestinal pseudo-obstruction. *Neurogastroenterology & Motility*, 30(9):e13371.

[44] J. W. Hahn, S. Y. Moon, M. S. Kim, M. H. Woo, M. J. Sohn, H.-Y. Kim, M.-W. Seong, S. S. Park, S.-H. Park, J. S. Moon, et al. (2022). Actg2 variants in pediatric chronic intestinal pseudo-obstruction with megacystis. *Journal of Neurogastroenterology and Motility*, 28(1):104.

[45] Z. Wei, L. Lu, Y. Zheng, W. Yan, Y. Tao, Y. Xiao, W. Cai, and Y. Wang (2021). Variants in the enteric smooth muscle actin γ-2 cause pediatric intestinal pseudo-obstruction in chinese patients. *Journal of Pediatric Gastroenterology and Nutrition*, 72(1):36–42.

[46] T. Maluleke, H. Mangray, M. Arnold, H. Moore, and S. Moore (2019). Recurrent actg2 gene variation in african degenerative visceral leiomyopathy. *Pediatric Surgery International*, 35:439–442.

[47] R. R. Collins, B. Barth, S. Megison, C. M. Pfeifer, L. M. Rice, S. Harris, C. F. Timmons, and D. Rakheja (2019). Actg2-associated visceral myopathy with chronic intestinal pseudoobstruction, intestinal malrotation, hypertrophic pyloric stenosis, choledochal cyst, and a novel missense mutation. *International journal of surgical pathology*, 27(1):77–83.

[48] K. M. Sanders, S. D. Koh, S. Ro, and S. M. Ward (2012). Regulation of gastrointestinal motility—insights from smooth muscle biology. *Nature reviews Gastroenterology & hepatology*, 9(11):633–645.

[49] W. Thorson, O. Diaz-Horta, J. Foster, M. Spiliopoulos, R. Quintero, A. Farooq, S. Blanton, and M. Tekin (2014). De novo actg2 mutations cause congenital distended bladder, microcolon, and intestinal hypoperistalsis. *Human genetics*, 133:737–742.

[50] D. Halim, M. P. Wilson, D. Oliver, E. Brosens, J. B. Verheij, Y. Han, V. Nanda, Q. Lyu, M. Doukas, H. Stoop, et al. (2017). Loss of lmod1 impairs smooth muscle cytocontractility and causes megacystis microcolon intestinal hypoperistalsis syndrome in humans and mice. *Proceedings of the National Academy of Sciences*, 114(13):E2739–E2747.

[51] D. Halim, E. Brosens, F. Muller, M. F. Wangler, A. L. Beaudet, J. R. Lupski, Z. H. C. Akdemir, M. Doukas, H. J. Stoop, B. M. De Graaf, et al. (2017). Loss-of-function variants in mylk cause recessive megacystis microcolon intestinal hypoperistalsis syndrome. *The American Journal of Human Genetics*, 101(1):123–129.

[52] E. Ü. Korğalı, A. Yavuz, C. E. Ç. Şimşek, C. Güney, H. K. Kurtulgan, B. Başer, M. H. Atalar, H. Özer, and H. R. Eğilmez (2018). Megacystis microcolon intestinal hypoperistalsis syndrome in which a different de novo actg2 gene mutation was detected: a case report. *Fetal and Pediatric Pathology*, 37(2):109–116.

[53] Y. Xiong, L. Dong, Y. Bai, H. Tang, S. Li, D. Luo, F. Liu, J. Bai, S. Yang, and X. Song (2022). Piezo1 activation facilitates ovarian cancer metastasis via hippo/yap signaling axis. *Channels*, 16(1):159–166.

[54] Z. Stark, T. Y. Tan, B. Chong, G. R. Brett, P. Yap, M. Walsh, A. Yeung, H. Peters, D. Mordaunt, S. Cowie, et al. (2016). A prospective evaluation of whole-exome sequencing as a first-tier molecular test in infants with suspected monogenic disorders. *Genetics in medicine*, 18(11):1090–1096.

[55] N. S. Sandy, K. Huysentruyt, D. J. Mulder, N. Warner, K. Chong, C. Morel, S. AlQahtani, P. W. Wales, M. G. Martin, A. M. Muise, et al. (2022). The diverse phenotype of intestinal dysmotility secondary to actg2-related disorders. *Journal of pediatric gastroenterology and nutrition*, 74(5):575–581.

[56] J. Klar, D. Raykova, E. Gustafson, I. Tóthová, A. Ameur, A. Wanders, and N. Dahl (2015). Phenotypic expansion of visceral myopathy associated with actg2 tandem base substitution. *European Journal of Human Genetics*, 23(12):1679–1683.

[57] R. Arnoldi, A. Hiltbrunner, V. Dugina, J.-C. Tille, and C. Chaponnier (2013). Smooth muscle actin isoforms: a tug of war between contraction and compliance. *European journal of cell biology*, 92(6-7):187–200.

[58] S. J. Gunst and W. Zhang (2008). Actin cytoskeletal dynamics in smooth muscle: a new paradigm for the regulation of smooth muscle contraction. *American Journal of Physiology-Cell Physiology*, 295(3):C576–C587.

[59] S. K. Hashmi, V. Barka, C. Yang, S. Schneider, T. M. Svitkina, and R. O. Heuckeroth (2020). Pseudo-obstruction–inducing actg2r257c alters actin organization and function. *JCI insight*, 5(16).

[60] M. J. Cipolla, N. I. Gokina, and G. Osol (2002). Pressure-induced actin polymerization in vascular smooth muscle as a mechanism underlying myogenic behavior. *The FASEB journal*, 16(1):72–76.

[61] T. D. Pollard and G. G. Borisy (2003). Cellular motility driven by assembly and disassembly of actin filaments. *Cell*, 112(4):453–465.

[62] P. A. Rubenstein and E. A. Mayer (2012). Familial visceral myopathies: from symptom-based syndromes to actin-related diseases. *Gastroenterology*, 143(6):1420–1423.

[63] S. K. Hashmi, R. H. Ceron, and R. O. Heuckeroth (2021). Visceral myopathy: clinical syndromes, genetics, pathophysiology, and fall of the cytoskeleton. *American Journal of Physiology-Gastrointestinal and Liver Physiology*, 320(6):G919–G935.

[64] J. L. Kandler, E. Sklirou, A. Woerner, L. Walsh, E. Cox, and Y. Xue (2020). Compound heterozygous loss of function variants in myl9 in a child with

megacystis–microcolon–intestinal hypoperistalsis syndrome. *Molecular Genetics & Genomic Medicine*, 8(11):e1516.

[65] J. Gauthier, B. Ouled Amar Bencheikh, F. F. Hamdan, S. M. Harrison, L. A. Baker, F. Couture, I. Thiffault, R. Ouazzani, M. E. Samuels, G. A. Mitchell, et al. (2015). A homozygous loss-of-function variant in myh11 in a case with megacystis-microcolon-intestinal hypoperistalsis syndrome. *European Journal of Human Genetics*, 23(9):1266–1268.

[66] A. Gargiulo, R. Auricchio, M. V. Barone, G. Cotugno, W. Reardon, P. J. Milla, A. Ballabio, A. Ciccodicola, and A. Auricchio (2007). Filamin a is mutated in x-linked chronic idiopathic intestinal pseudo-obstruction with central nervous system involvement. *The American Journal of Human Genetics*, 80(4):751–758.

[67] M. A. Gilbert, L. Schultz-Rogers, R. Rajagopalan, C. M. Grochowski, B. J. Wilkins, S. Biswas, L. K. Conlin, K. N. Fiorino, R. Dhamija, M. A. Pack, et al. (2020). Protein-elongating mutations in myh11 are implicated in a dominantly inherited smooth muscle dysmotility syndrome with severe esophageal, gastric, and intestinal disease. *Human mutation*, 41(5):973–982.

[68] C. A. Moreno, N. Sobreira, E. Pugh, P. Zhang, G. Steel, F. R. Torres, and D. P. Cavalcanti (2018). Homozygous deletion in myl9 expands the molecular basis of megacystis–microcolon–intestinal hypoperistalsis syndrome. *European Journal of Human Genetics*, 26(5):669–675.

[69] M. Boczkowska, G. Rebowski, E. Kremneva, P. Lappalainen, and R. Dominguez (2015). How leiomodin and tropomodulin use a common fold for different actin assembly functions. *Nature communications*, 6(1):8314.

[70] F. Nakamura, T. P. Stossel, and J. H. Hartwig (2011). The filamins: organizers of cell structure and function. *Cell adhesion & migration*, 5(2):160–169.

[71] M. Mericskay, J. Blanc, E. Tritsch, R. Moriez, P. Aubert, M. Neunlist, R. Feil, and Z. Li (2007). Inducible mouse model of chronic intestinal pseudo-obstruction by smooth muscle-specific inactivation of the srf gene. *Gastroenterology*, 133(6):1960–1970.

[72] A. C. Houweling, G. M. Beaman, A. V. Postma, T. B. Gainous, K. D. Lichtenbelt, F. Brancati, F. M. Lopes, I. Van Der Made, A. M. Polstra, M. L. Robinson, et al. (2019). Loss-of-function variants in myocardin cause congenital megabladder in humans and mice. *The Journal of clinical investigation*, 129(12):5374–5380.

[73] X. He, J. Song, Z. Cai, X. Chi, Z. Wang, D. Yang, S. Xie, J. Zhou, Y. Fu, W. Li, et al. (2020). Kindlin-2 deficiency induces fatal intestinal obstruction in mice. *Theranostics*, 10(14):6182.

[74] E. Bonora, S. Chakrabarty, G. Kellaris, M. Tsutsumi, F. Bianco, C. Bergamini, F. Ullah, F. Isidori, I. Liparulo, C. Diquigiovanni, et al. (2021). Biallelic variants in lig3 cause a novel mitochondrial neurogastrointestinal encephalomyopathy. *Brain*, 144(5):1451–1466.

[75] R. Dasgupta and J. C. Langer (2004). Hirschsprung disease. *Current problems in surgery*, 41(12):949–988.

[76] A. M. Goldstein, N. Thapar, T. B. Karunaratne, and R. De Giorgio (2016). Clinical aspects of neurointestinal disease: Pathophysiology, diagnosis, and treatment. *Developmental biology*, 417(2):217–228.

[77] H. Tanaka, J. Ito, K. Cho, and M. Mikawa (1993). Hirschsprung disease, unusual face, mental retardation, epilepsy, and congenital heart disease: Goldberg-shprintzen syndrome. *Pediatric neurology*, 9(6):479–481.

[78] M. J. Cuneo, S. A. Gabel, J. M. Krahn, M. A. Ricker, and R. E. London (2011). The structural basis for partitioning of the xrcc1/dna ligase iii-α brct-mediated dimer complexes. *Nucleic acids research*, 39(17):7816–7827.

[79] Y. Gao, S. Katyal, Y. Lee, J. Zhao, J. E. Rehg, H. R. Russell, and P. J. McKinnon (2011). Dna ligase iii is critical for mtdna integrity but not xrcc1-mediated nuclear dna repair. *Nature*, 471(7337):240–244.

[80] S. DiMauro, E. A. Schon, V. Carelli, and M. Hirano (2013). The clinical maze of mitochondrial neurology. *Nature Reviews Neurology*, 9(8):429–444.

[81] J. Amiel, E. Sproat-Emison, M. Garcia-Barcelo, F. Lantieri, G. Burzynski, S. Borrego, A. Pelet, S. Arnold, X. Miao, P. Griseri, et al. (2008). Hirschsprung disease, associated syndromes and genetics: a review. *Journal of medical genetics*, 45(1):1–14.

[82] F. Viti, F. M. Pramotton, M. Martufi, R. Magrassi, N. Pedemonte, M. Nizzari, F. C. Zanacchi, B. De Michele, M. Alampi, M. Zambito, et al. (2023). Patient's dermal fibroblasts as disease markers for visceral myopathy. *Biomaterials Advances*, 148:213355.

[83] R. B. D'Agostino (2017). *Goodness-of-fit-techniques*. Routledge.

[84] B. L. Welch (1947). The generalization of 'student's'problem when several different population varlances are involved. *Biometrika*, 34(1-2):28–35.

[85] H. B. Mann and D. R. Whitney (1947). On a test of whether one of two random variables is stochastically larger than the other. *The annals of mathematical statistics*, pages 50–60.

[86] S. A. Glantz, B. K. Slinker, and T. B. Neilands (2001). *Primer of applied regression & analysis of variance, ed.* Volume 654, McGraw-Hill, Inc., New York.

[87] C. W. Dunnett (1980). Pairwise multiple comparisons in the unequal variance case. *Journal of the American Statistical Association*, 75(372):796–800.

[88] W. H. Kruskal and W. A. Wallis (1952). Use of ranks in one-criterion variance analysis. *Journal of the American statistical Association*, 47(260):583–621.

[89] O. J. Dunn (1964). Multiple comparisons using rank sums. *Technometrics*, 6(3):241–252.

[90] R. M. Houtekamer, M. C. van der Net, M. M. Maurice, and M. Gloerich (2022). Mechanical forces directing intestinal form and function. *Current Biology*, 32(14):R791–R805.

[91] H. GREGERSEN and G. KASSAB (1996). Biomechanics of the gastrointestinal tract. *Neurogastroenterology & Motility*, 8(4):277–297.

[92] C. P. Gayer and M. D. Basson (2009). The effects of mechanical forces on intestinal physiology and pathology. *Cellular Signalling*, 21(8):1237–1244.

[93] R. K. Avvari (2023). Role of segmental contraction in the small intestinal digestion: A computational approach to study the physics behind the luminal mixing and transport. *Journal of Theoretical Biology*, 561:111418.

[94] C. T. Lim, A. Bershadsky, and M. P. Sheetz. Mechanobiology, (2010).

[95] T. Luo, K. Mohan, P. A. Iglesias, and D. N. Robinson (2013). Molecular mechanisms of cellular mechanosensing. *Nature materials*, 12(11):1064–1071.

[96] A. W. Orr, B. P. Helmke, B. R. Blackman, and M. A. Schwartz (2006). Mechanisms of mechanotransduction. *Developmental cell*, 10(1):11–20.

[97] H. W. Thomas Iskratsch and M. Sheetz (2014). Appreciating force and shape—the rise of mechanotransduction in cell biology. *Nature reviews. Molecular cell biology*, 15(12):825–33.

[98] S. D. Stefano Piccolo and M. Cordenonsi The biology of yap/taz: hippo signaling and beyond. *Physiological reviews*, 94(4):1287–312.

[99] T. Panciera, L. Azzolin, M. Cordenonsi, and S. Piccolo (2017). Mechanobiology of yap and taz in physiology and disease. *Nature reviews Molecular cell biology*, 18(12):758–770.

[100] S. Ghassemi, G. Meacci, S. Liu, A. A. Gondarenko, A. Mathur, P. Roca-Cusachs, M. P. Sheetz, and J. Hone (2012). Cells test substrate rigidity by local contractions on submicrometer pillars. *Proceedings of the National Academy of Sciences*, 109(14):5328–5333.

[101] C. H. Rasmussen, P. M. Reynolds, D. R. Petersen, M. Hansson, R. M. McMeeking, M. Dufva, and N. Gadegaard (2016). Enhanced differentiation of human embryonic stem cells toward definitive endoderm on ultrahigh aspect ratio nanopillars. *Advanced Functional Materials*, 26(6):815–823.

[102] A. M. Kloxin, C. J. Kloxin, C. N. Bowman, and K. S. Anseth (2010). Mechanical properties of cellularly responsive hydrogels and their experimental determination. *Advanced Materials*, 22(31):3484–3494.

[103] S. Dupont, L. Morsut, M. Aragona, E. Enzo, S. Giulitti, M. Cordenonsi, F. Zanconato, J. Le Digabel, M. Forcato, S. Bicciato, et al. (2011). Role of yap/taz in mechanotransduction. *Nature*, 474(7350):179–183.

[104] M. Aragona, T. Panciera, A. Manfrin, S. Giulitti, F. Michielin, N. Elvassore, S. Dupont, and S. Piccolo (2013). A mechanical checkpoint controls multicellular growth through yap/taz regulation by actin-processing factors. *Cell*, 154(5):1047–1059.

[105] J. Y. Lee, J. K. Chang, A. A. Dominguez, H.-p. Lee, S. Nam, J. Chang, S. Varma, L. S. Qi, R. B. West, and O. Chaudhuri (2019). Yap-independent mechanotransduction drives breast cancer progression. *Nature communications*, 10(1):1848.

[106] A. E. Stanton, X. Tong, S. Lee, and F. Yang (2019). Biochemical ligand density regulates yes-associated protein translocation in stem cells through cytoskeletal tension and integrins. *ACS applied materials & interfaces*, 11(9):8849–8857.

[107] S. R. Caliari, S. L. Vega, M. Kwon, E. M. Soulas, and J. A. Burdick (2016). Dimensionality and spreading influence msc yap/taz signaling in hydrogel environments. *Biomaterials*, 103:314–323.

[108] J. Oliver-De La Cruz, G. Nardone, J. Vrbsky, A. Pompeiano, A. R. Perestrelo, F. Capradossi, K. Melajová, P. Filipensky, and G. Forte (2019). Substrate mechanics controls adipogenesis through yap phosphorylation by dictating cell spreading. *Biomaterials*, 205:64–80.

[109] E. Cambria, M. F. Coughlin, M. A. Floryan, G. S. Offeddu, S. E. Shelton, and R. D. Kamm (2024). Linking cell mechanical memory and cancer metastasis. *Nature Reviews Cancer*, pages 1–13.

[110] O. Y. Dudaryeva, S. Bernhard, M. W. Tibbitt, and C. Labouesse (2023). Implications of cellular mechanical memory in bioengineering. *ACS Biomaterials Science & Engineering*, 9(11):5985–5998.

[111] C. Yang, M. W. Tibbitt, L. Basta, and K. S. Anseth (2014). Mechanical memory and dosing influence stem cell fate. *Nature materials*, 13(6):645–652.

[112] F. Daoud, J. Holmberg, A. Alajbegovic, M. Grossi, C. Rippe, K. Swärd, and S. Albinsson (2021). Inducible deletion of yap and taz in adult mouse smooth muscle causes rapid and lethal colonic pseudo-obstruction. *Cellular and Molecular Gastroenterology and Hepatology*, 11(2):623–637.

[113] S. O. Sarrigiannidis, J. M. Rey, O. Dobre, C. González-García, M. J. Dalby, and M. Salmeron-Sanchez (2021). A tough act to follow: Collagen hydrogel modifications to improve mechanical and growth factor loading capabilities. *Materials Today Bio*, 10:100098.

[114] R. Parenteau-Bareil, R. Gauvin, and F. Berthod (2010). Collagen-based biomaterials for tissue engineering applications. *Materials*, 3(3):1863–1887.

[115] J. W. Nichol, S. T. Koshy, H. Bae, C. M. Hwang, S. Yamanlar, and A. Khademhosseini (2010). Cell-laden microengineered gelatin methacrylate hydrogels. *Biomaterials*, 31(21):5536–5544.

[116] E. Kaemmerer, F. P. Melchels, B. M. Holzapfel, T. Meckel, D. W. Hutmacher, and D. Loessner (2014). Gelatine methacrylamide-based hydrogels: An alternative three-dimensional cancer cell culture system. *Acta biomaterialia*, 10(6):2551–2562.

[117] I. Miranda, A. Souza, P. Sousa, J. Ribeiro, E. M. Castanheira, R. Lima, and G. Minas (2021). Properties and applications of pdms for biomedical engineering: A review. *Journal of functional biomaterials*, 13(1):2.

[118] T. Zhang, J. H. Day, X. Su, A. G. Guadarrama, N. K. Sandbo, S. Esnault, L. C. Denlinger, E. Berthier, and A. B. Theberge (2019). Investigating fibroblast-induced collagen gel contraction using a dynamic microscale platform. *Frontiers in bioengineering and biotechnology*, 7:196.

[119] M. Ahearne (2014). Introduction to cell–hydrogel mechanosensing. *Interface focus*, 4(2):20130038.

[120] F. Tabatabaei, K. Moharamzadeh, and L. Tayebi (2020). Fibroblast encapsulation in gelatin methacryloyl (gelma) versus collagen hydrogel as substrates for oral mucosa tissue engineering. *Journal of Oral Biology and Craniofacial Research*, 10(4):573–577.

[121] Y. Piao, H. You, T. Xu, H.-P. Bei, I. Z. Piwko, Y. Y. Kwan, and X. Zhao (2021). Biomedical applications of gelatin methacryloyl hydrogels. *Engineered Regeneration*, 2:47–56.

[122] D. E. Mason, J. M. Collins, J. H. Dawahare, T. D. Nguyen, Y. Lin, S. L. Voytik-Harbin, P. Zorlutuna, M. C. Yoder, and J. D. Boerckel (2019). Yap and taz limit cytoskeletal and focal adhesion maturation to enable persistent cell motility. *Journal of Cell Biology*, 218(4):1369–1389.

[123] H. J. Lee, M. F. Diaz, K. M. Price, J. A. Ozuna, S. Zhang, E. M. Sevick-Muraca, J. P. Hagan, and P. L. Wenzel (2017). Fluid shear stress activates yap1 to promote cancer cell motility. *Nature communications*, 8(1):14122.

[124] G. Charras and E. Sahai (2014). Physical influences of the extracellular environment on cell migration. *Nature reviews Molecular cell biology*, 15(12):813–824.

[125] P. Devreotes and A. R. Horwitz (2015). Signaling networks that regulate cell migration. *Cold Spring Harbor perspectives in biology*, 7(8):a005959.

[126] M. Schaks, G. Giannone, and K. Rottner (2019). Actin dynamics in cell migration. *Essays in biochemistry*, 63(5):483–495.

[127] T. Svitkina (2018). The actin cytoskeleton and actin-based motility. *Cold Spring Harbor perspectives in biology*, 10(1):a018267.

[128] S. Yamashiro and N. Watanabe (2014). A new link between the retrograde actin flow and focal adhesions. *The journal of biochemistry*, 156(5):239–248.

[129] T. Mitchison and M. Kirschner (1988). Cytoskeletal dynamics and nerve growth. *Neuron*, 1(9):761–772.

[130] L. B. Case and C. M. Waterman (2015). Integration of actin dynamics and cell adhesion by a three-dimensional, mechanosensitive molecular clutch. *Nature cell biology*, 17(8):955–963.

[131] G. Popescu, L. P. Deflores, J. C. Vaughan, K. Badizadegan, H. Iwai, R. R. Dasari, and M. S. Feld (2004). Fourier phase microscopy for investigation of biological structures and dynamics. *Optics letters*, 29(21):2503–2505.

[132] P. Langehanenberg, L. Ivanova, I. Bernhardt, S. Ketelhut, A. Vollmer, D. Dirksen, G. Georgiev, G. von Bally, and B. Kemper (2009). Automated three-dimensional tracking of living cells by digital holographic microscopy. *Journal of biomedical optics*, 14(1):014018–014018.

[133] B. Rappaz, P. Marquet, E. Cuche, Y. Emery, C. Depeursinge, and P. J. Magistretti (2005). Measurement of the integral refractive index and dynamic cell morphometry of living cells with digital holographic microscopy. *Optics express*, 13(23):9361–9373.

[134] R. Kasprowicz, R. Suman, and P. O'Toole (2017). Characterising live cell behaviour: Traditional label-free and quantitative phase imaging approaches. *The international journal of biochemistry & cell biology*, 84:89–95.

[135] K. Alm, H. Cirenajwis, L. Gisselsson, A. Gjörloff Wingren, B. Janicke, A. Mölder, S. Oredsson, and J. Persson (2011). *Digital holography and cell studies*. DKV-Deutscher Kälte-und Klimatechnischer Verein.

[136] R. M. Haralick, K. Shanmugam, and I. H. Dinstein (1973). Textural features for image classification. *IEEE Transactions on systems, man, and cybernetics*, (6):610–621.

[137] M. Sebesta, P. J. Egelberg, A. Langberg, J.-H. Lindskov, K. Alm, and B. Janicke. Holomonitor m4: holographic imaging cytometer for real-time kinetic label-free live-cell analysis of adherent cells. In *Quantitative phase imaging II*, Volume 9718, pages 146–155. SPIE, (2016).

[138] M. Gustafsson and M. Sebesta (2004). Refractometry of microscopic objects with digital holography. *Applied optics*, 43(25):4796–4801.

[139] S. Simonthomas, N. Thulasi, and P. Asharaf. Automated diagnosis of glaucoma using haralick texture features. In *International conference on information communication and embedded systems (ICICES2014)*, pages 1–6. IEEE, (2014).

[140] N. Zayed and H. A. Elnemr (2015). Statistical analysis of haralick texture features to discriminate lung abnormalities. *Journal of Biomedical Imaging*, 2015:12–12.

[141] Z. Sun, S. S. Guo, and R. Fässler (2016). Integrin-mediated mechanotransduction. *Journal of Cell Biology*, 215(4):445–456.

[142] I. Andreu, B. Falcones, S. Hurst, N. Chahare, X. Quiroga, A.-L. Le Roux, Z. Kechagia, A. E. Beedle, A. Elosegui-Artola, X. Trepat, et al. (2021). The force loading rate drives cell mechanosensing through both reinforcement and cytoskeletal softening. *Nature communications*, 12(1):4229.

[143] F. Merino-Casallo, M. J. Gomez-Benito, S. Hervas-Raluy, and J. M. Garcia-Aznar (2022). Unravelling cell migration: defining movement from the cell surface. *Cell adhesion & migration*, 16(1):25–64.

[144] B. Coste, J. Mathur, M. Schmidt, T. J. Earley, S. Ranade, M. J. Petrus, A. E. Dubin, and A. Patapoutian (2010). Piezo1 and piezo2 are essential components of distinct mechanically activated cation channels. *Science*, 330(6000):55–60.

[145] B. Coste, B. Xiao, J. S. Santos, R. Syeda, J. Grandl, K. S. Spencer, S. E. Kim, M. Schmidt, J. Mathur, A. E. Dubin, et al. (2012). Piezo proteins are pore-forming subunits of mechanically activated channels. *Nature*, 483(7388):176–181.

[146] P. Ridone, M. Vassalli, and B. Martinac (2019). Piezo1 mechanosensitive channels: what are they and why are they important. *Biophysical reviews*, 11(5):795–805.

[147] J. Ge, W. Li, Q. Zhao, N. Li, M. Chen, P. Zhi, R. Li, N. Gao, B. Xiao, and M. Yang (2015). Architecture of the mammalian mechanosensitive piezo1 channel. *Nature*, 527(7576):64–69.

[148] J. L. Nourse and M. M. Pathak. How cells channel their stress: Interplay between piezo1 and the cytoskeleton. In *Seminars in cell & developmental biology*, Volume 71, pages 3–12. Elsevier, (2017).

[149] C. Verkest and S. G. Lechner (2023). Advances and recent insights into the gating mechanisms of the mechanically activated ion channels piezo1 and piezo2. *Current Opinion in Physiology*, 31:100625.

[150] C. D. Cox, C. Bae, L. Ziegler, S. Hartley, V. Nikolova-Krstevski, P. R. Rohde, C.-A. Ng, F. Sachs, P. A. Gottlieb, and B. Martinac (2016). Removal of the mechanoprotective influence of the cytoskeleton reveals piezo1 is gated by bilayer tension. *Nature communications*, 7(1):10366.

[151] R. Syeda, M. N. Florendo, C. D. Cox, J. M. Kefauver, J. S. Santos, B. Martinac, and A. Patapoutian (2016). Piezo1 channels are inherently mechanosensitive. *Cell reports*, 17(7):1739–1746.

[152] A. H. Lewis and J. Grandl (2015). Mechanical sensitivity of piezo1 ion channels can be tuned by cellular membrane tension. *Elife*, 4:e12088.

[153] J. Hu, L.-Y. Chiang, M. Koch, and G. R. Lewin (2010). Evidence for a protein tether involved in somatic touch. *The EMBO journal*, 29(4):855–867.

[154] J. Wang, J. Jiang, X. Yang, G. Zhou, L. Wang, and B. Xiao (2022). Tethering piezo channels to the actin cytoskeleton for mechanogating via the cadherin-β-catenin mechanotransduction complex. *Cell Reports*, 38(6).

[155] E. Fotiou, S. Martin-Almedina, M. A. Simpson, S. Lin, K. Gordon, G. Brice, G. Atton, I. Jeffery, D. C. Rees, C. Mignot, et al. (2015). Novel mutations in piezo1 cause an autosomal recessive generalized lymphatic dysplasia with non-immune hydrops fetalis. *Nature communications*, 6(1):8085.

[156] V. Lukacs, J. Mathur, R. Mao, P. Bayrak-Toydemir, M. Procter, S. M. Cahalan, H. J. Kim, M. Bandell, N. Longo, R. W. Day, et al. (2015). Impaired piezo1 function in patients with a novel autosomal recessive congenital lymphatic dysplasia. *Nature communications*, 6(1):8329.

[157] J. Albuisson, S. E. Murthy, M. Bandell, B. Coste, H. Louis-dit Picard, J. Mathur, M. Fénéant-Thibault, G. Tertian, J.-P. de Jaureguiberry, P.-Y. Syfuss, et al. (2013). Dehydrated hereditary stomatocytosis linked to gain-of-function mutations in mechanically activated piezo1 ion channels. *Nature communications*, 4(1):1884.

[158] I. Andolfo, S. L. Alper, L. De Franceschi, C. Auriemma, R. Russo, L. De Falco, F. Vallefuoco, M. R. Esposito, D. H. Vandorpe, B. E. Shmukler, et al. (2013). Multiple clinical forms of dehydrated hereditary stomatocytosis arise from mutations in piezo1. *Blood, The Journal of the American Society of Hematology*, 121(19):3925–3935.

[159] S. Demolombe, F. Duprat, E. Honoré, and A. Patel (2013). Slower piezo1 inactivation in dehydrated hereditary stomatocytosis (xerocytosis). *Biophysical journal*, 105(4):833–834.

[160] N. G. Amado, E. D. Nosyreva, D. Thompson, T. J. Egeland, O. W. Ogujiofor, M. Yang, A. N. Fusco, N. Passoni, J. Mathews, B. Cantarel, et al. (2024). Piezo1 loss-of-function compound heterozygous mutations in the rare congenital human disorder prune belly syndrome. *Nature communications*, 15(1):339.

[161] J. M.-J. Romac, R. A. Shahid, S. M. Swain, S. R. Vigna, and R. A. Liddle (2018). Piezo1 is a mechanically activated ion channel and mediates pressure induced pancreatitis. *Nature communications*, 9(1):1715.

[162] W. Zhu, S. Guo, M. Homilius, C. Nsubuga, S. H. Wright, D. Quan, A. Kc, S. S. Eddy, R. A. Victorio, M. Beerens, et al. (2022). Piezo1 mediates a mechanothrombotic pathway in diabetes. *Science Translational Medicine*, 14(626):eabk1707.

[163] K. Hasegawa, S. Fujii, S. Matsumoto, Y. Tajiri, A. Kikuchi, and T. Kiyoshima (2021). Yap signaling induces piezo1 to promote oral squamous cell carcinoma cell proliferation. *The Journal of pathology*, 253(1):80–93.

[164] B. Zhu, W. Qian, C. Han, T. Bai, and X. Hou (2021). Piezo 1 activation facilitates cholangiocarcinoma metastasis via hippo/yap signaling axis. *Molecular Therapy-Nucleic Acids*, 24:241–252.

[165] M. Li, X. Zhang, M. Wang, Y. Wang, J. Qian, X. Xing, Z. Wang, Y. You, K. Guo, J. Chen, et al. (2022). Activation of piezo1 contributes to matrix stiffness-induced angiogenesis in hepatocellular carcinoma. *Cancer Communications*, 42(11):1162–1184.

[166] Q. Liu, D. Wang, X. Yang, F. Ma, W. Han, J. Hu, and Q. Mei (2023). The mechanosensitive ion channel piezo1 in intestinal epithelial cells mediates inflammation through the nod-like receptor 3 pathway in crohn's disease. *Inflammatory Bowel Diseases*, 29(1):103–115.

[167] K. Hasegawa, S. Fujii, S. Matsumoto, Y. Tajiri, A. Kikuchi, and T. Kiyoshima (2021). Yap signaling induces piezo1 to promote oral squamous cell carcinoma cell proliferation. *The Journal of pathology*, 253(1):80–93.

[168] G. Zhong, S. Su, J. Li, H. Zhao, D. Hu, J. Chen, S. Li, Y. Lin, L. Wen, X. Lin, et al. (2023). Activation of piezo1 promotes osteogenic differentiation of aortic valve interstitial cell through yap-dependent glutaminolysis. *Science Advances*, 9(22):eadg0478.

[169] M. M. Pathak, J. L. Nourse, T. Tran, J. Hwe, J. Arulmoli, D. T. T. Le, E. Bernardis, L. A. Flanagan, and F. Tombola (2014). Stretch-activated ion channel piezo1 directs lineage choice in human neural stem cells. *Proceedings of the National Academy of Sciences*, 111(45):16148–16153.

[170] K. L. Ellefsen, J. R. Holt, A. C. Chang, J. L. Nourse, J. Arulmoli, A. H. Mekhdjian, H. Abuwarda, F. Tombola, L. A. Flanagan, A. R. Dunn, et al. (2019). Myosin-ii mediated traction forces evoke localized piezo1-dependent ca2+ flickers. *Communications biology*, 2(1):298.

[171] X. Chen, S. Wanggou, A. Bodalia, M. Zhu, W. Dong, J. J. Fan, W. C. Yin, H.-K. Min, M. Hu, D. Draghici, et al. (2018). A feedforward mechanism mediated by mechanosensitive ion channel piezo1 and tissue mechanics promotes glioma aggression. *Neuron*, 100(4):799–815.

[172] M. Yao, A. Tijore, D. Cheng, J. V. Li, A. Hariharan, B. Martinac, G. Tran Van Nhieu, C. D. Cox, and M. Sheetz (2022). Force-and cell state–dependent recruitment of piezo1 drives focal adhesion dynamics and calcium entry. *Science advances*, 8(45):eabo1461.

[173] D. Jetta, T. Shireen, and S. Z. Hua (2023). Epithelial cells sense local stiffness via piezo1 mediated cytoskeletal reorganization. *Frontiers in Cell and Developmental Biology*, 11:1198109.

[174] S. Liu, X. Xu, Z. Fang, Y. Ning, B. Deng, X. Pan, Y. He, Z. Yang, K. Huang, and J. Li (2021). Piezo1 impairs hepatocellular tumor growth via deregulation of the mapk-mediated yap signaling pathway. *Cell Calcium*, 95:102367.

[175] B. Zhu, W. Qian, C. Han, T. Bai, and X. Hou (2021). Piezo 1 activation facilitates cholangiocarcinoma metastasis via hippo/yap signaling axis. *Molecular Therapy-Nucleic Acids*, 24:241–252.

[176] Y. Xiong, L. Dong, Y. Bai, H. Tang, S. Li, D. Luo, F. Liu, J. Bai, S. Yang, and X. Song (2022). Piezo1 activation facilitates ovarian cancer metastasis via hippo/yap signaling axis. *Channels*, 16(1):159–166.

[177] X. Li, J. Kordsmeier, I. Nookaew, H.-N. Kim, and J. Xiong (2022). Piezo1 stimulates mitochondrial function via camp signaling. *FASEB journal: official publication of the Federation of American Societies for Experimental Biology*, 36(10):e22519.

[178] Q. Yin, G. Zang, N. Li, C. Sun, and R. Du (2022). Agonist-induced piezo1 activation promote mitochondrial-dependent apoptosis in vascular smooth muscle cells. *BMC cardiovascular disorders*, 22(1):287.

[179] S. Shi, X.-J. Kang, Z. Zhou, Z.-M. He, S. Zheng, and S.-S. He (2022). Excessive mechanical stress-induced intervertebral disc degeneration is related to piezo1 overexpression triggering the imbalance of autophagy/apoptosis in human nucleus pulpous. *Arthritis Research & Therapy*, 24(1):119.

[180] S. Hart, O. M. Fischer, N. Prenzel, E. Zwick-Wallasch, M. Schneider, L. Hennighausen, and A. Ullrich (2005). Gpcr-induced migration of breast carcinoma cells depends on both egfr signal transactivation and egfr-independent pathways. *Biological chemistry*, 386(9):845–855.

[181] B. S. Verbeek, S. S. Adriaansen-Slot, T. M. Vroom, T. Beckers, and G. Rijksen (1998). Overexpression of egfr and c-erbb2 causes enhanced cell migration in human breast cancer cells and nih3t3 fibroblasts. *FEBS letters*, 425(1):145–150.

[182] N. Normanno, A. De Luca, C. Bianco, L. Strizzi, M. Mancino, M. R. Maiello, A. Carotenuto, G. De Feo, F. Caponigro, and D. S. Salomon (2006). Epidermal growth factor receptor (egfr) signaling in cancer. *Gene*, 366(1):2–16.

[183] N. K. Saxena, L. Taliaferro-Smith, B. B. Knight, D. Merlin, F. A. Anania, R. M. O'Regan, and D. Sharma (2008). Bidirectional crosstalk between leptin and insulin-like growth factor-i signaling promotes invasion and migration of breast cancer cells via transactivation of epidermal growth factor receptor. *Cancer research*, 68(23):9712–9722.

[184] J. Shen, G. Liu, H. Qi, X. Xiang, and J. Shao (2023). Jmjd5 inhibits lung cancer progression by facilitating egfr proteasomal degradation. *Cell Death & Disease*, 14(10):657.

[185] H. W. Park, Y. C. Kim, B. Yu, T. Moroishi, J.-S. Mo, S. W. Plouffe, Z. Meng, K. C. Lin, F.-X. Yu, C. M. Alexander, et al. (2015). Alternative wnt signaling activates yap/taz. *Cell*, 162(4):780–794.

[186] L. Jiang, J. Li, C. Zhang, Y. Shang, and J. Lin (2020). Yap-mediated crosstalk between the wnt and hippo signaling pathways. *Molecular medicine reports*, 22(5):4101–4106.

[187] H. Hirai, B. Yang, M. T. Garcia-Barrio, O. Rom, P. X. Ma, J. Zhang, and Y. E. Chen (2018). Direct reprogramming of fibroblasts into smooth muscle-like cells with defined transcription factors—brief report. *Arteriosclerosis, thrombosis, and vascular biology*, 38(9):2191–2197.

[188] J. Núñez-Manchón, J. Capó, A. Martínez-Piñeiro, E. Juanola, J. Pesovic, L. Mosqueira-Martín, K. González-Imaz, P. Maestre-Mora, R. Odria, D. Savic-Pavicevic, et al. (2024). Immortalized human myotonic dystrophy type 1 muscle cell lines to address patient heterogeneity. *Iscience*, 27(6).

[189] L. Arandel, M. Polay Espinoza, M. Matloka, A. Bazinet, D. de Dea Diniz, N. Naouar, F. Rau, A. Jollet, F. Edom-Vovard, K. Mamchaoui, et al. (2017). Immortalized human myotonic dystrophy muscle cell lines to assess therapeutic compounds. *Disease models & mechanisms*, 10(4):487–497.

[190] B. Tedesco, L. Vendredy, E. Adriaenssens, M. Cozzi, B. Asselbergh, V. Crippa, R. Cristofani, P. Rusmini, V. Ferrari, E. Casarotto, et al. (2023). Hspb8 frameshift mutant aggregates weaken chaperone-assisted selective autophagy in neuromyopathies. *Autophagy*, 19(8):2217–2239.

[191] E. Lemerle, J. Lainé, M. Benoist, G. Moulay, A. Bigot, C. Labasse, A. Madelaine, A. Canette, P. Aubin, J.-M. Vallat, et al. (2023). Caveolae and bin1 form ring-shaped platforms for t-tubule initiation. *Elife*, 12:e84139.

[192] I. Lüchtefeld, I. V. Pivkin, L. Gardini, E. Zare-Eelanjegh, C. Gäbelein, S. J. Ihle, A. M. Reichmuth, M. Capitanio, B. Martinac, T. Zambelli, et al.

(2024). Dissecting cell membrane tension dynamics and its effect on piezo1-mediated cellular mechanosensitivity using force-controlled nanopipettes. *Nature Methods*, pages 1–11.